



Particles II

Access the latest eBook →

11

Advanced
Optical Metrology

Particles II



EVIDENT
OLYMPUS

WILEY

Impact on Biological Systems and the Environment

This eBook is dedicated to the research of Professor David Wertheim.

In collaboration with various groups, Professor Wertheim uses confocal microscopy to analyse the impact of different types of particles on human health and the environment, with a focus on human health-hazardous particles detected with solid-state nuclear track detectors (SSNTD). Download for free, today.

EVIDENT
OLYMPUS

WILEY

Printed Thermoelectrics

Matthew Burton,* Geraint Howells, Jonathan Atoyo, and Matthew Carnie

The looming impact of climate change and the diminishing supply of fossil fuels both highlight the need for a transition to more sustainable energy sources. While solar and wind can produce much of the energy needed, to meet all our energy demands there is a need for a diverse sustainable energy generation mix. Thermoelectrics can play a vital role in this, by harvesting otherwise wasted heat energy and converting it into useful electrical energy. While efficient thermoelectric materials have been known since the 1950s, thermoelectrics have not been utilized beyond a few niche applications. This can in part be attributed to the high cost of manufacturing and the geometrical restraints of current commercial manufacturing techniques. Printing offers a potential route to manufacture thermoelectric materials at a lower price point and allows for the fabrication of generators that are custom built to meet the waste heat source requirements. This review details the significant progress that has been made in recent years in printing of thermoelectric materials in all thermoelectric material groups and printing methods, and highlights very recent publications that show printing can now offer comparable performance to commercially manufactured thermoelectric materials.

1. Introduction

In a world that is continually becoming more aware of the impact of climate change and where there is an ever-depleting source of fossil fuels, there is a necessity to transition to more sustainable energy systems. Renewables such as wind, solar and tidal energy have the capability to produce much of our energy needs, yet a greater mix of energy saving and harvesting technologies are required to meet our future energy requirements.^[1] In order to have a sustainable future, there needs to be a diverse mixture of renewable and sustainable technologies in use, thermoelectrics

can have a key part in that mixture. A 2014 estimate found that 48 TWh yr⁻¹ of energy is lost as waste heat from UK industrial sources alone.^[2] Capturing just 1% of that energy would lead to a reduction of 0.25 Tg yr⁻¹ in CO₂ emissions.^[3]

Thermoelectric devices are heat engines, a consequence of this is that the maximum efficiency is limited by the Carnot efficiency, $\eta = (T_H - T_C)/T_H$. This dictates that energy can only be absorbed from the heat differential between the hot side (T_H) and the cold side (T_C); energy cannot be absorbed from the background temperature. In addition to the Carnot efficiency limitation, the efficiency of thermoelectric generators is also limited by the dimensionless material property ZT . The figure of merit (ZT , Equation 1) is composed of the interrelated material properties of the Seebeck coefficient (S , V K⁻¹), electrical conductivity (σ , S m⁻¹), thermal conductivity (κ , W m⁻¹ K⁻¹) and

the absolute temperature (T , K).^[4] Thermal conductivity can be expressed as the sum of the electronic component (κ_e) and the lattice component (κ_L), Equation 2. ZT can, therefore, be written as expressed in Equation 3. Due to the interrelated nature of the properties comprising ZT , optimizing one property leads to the detrimental effects on another.^[4] One example of this is Wiedemann-Franz law, which states that electrical conductivity is proportional to the electronic component of thermal conductivity ($\sigma \propto \kappa_e$). This leads to an increase in electrical conductivity leading to a simultaneous increase in thermal conductivity, which counteracts each other in terms of ZT . This has led to slow progress in improving ZT , with heavily doped semiconductors striking the best balance between the interrelated material parameters. While a ZT of 1 was achieved in the 1950s in Bi₂Te₃ and PbTe,^[5,6] increases have been slow throughout the years since. In the last decade, however, significant improvements in ZT have been reported in materials, such as Cu₂S_{0.52}Te_{0.48} with a ZT of 2.1,^[7] PbTe–SrTe with a ZT of 2.5,^[8] and SnSe with a ZT of 2.7.^[9]

$$ZT = \frac{S^2 \sigma}{\kappa} T \quad (1)$$


$$\kappa = \kappa_e + \kappa_L \quad (2)$$

$$ZT = \frac{S^2 \sigma}{\kappa_e + \kappa_L} T \quad (3)$$

Efficient thermoelectric devices require both p- and n-type semiconductor materials (Figure 1), so when calculating a

M. Burton, M. Carnie
SPECIFIC, Materials Research Centre
Faculty of Science and Engineering
Swansea University
Bay Campus, Swansea SA1 8EN, UK
E-mail: m.r.burton@swansea.ac.uk

G. Howells, J. Atoyo
M2A
Materials Research Centre
Faculty of Science and Engineering
Swansea University
Bay Campus, Swansea SA1 8EN, UK

 The ORCID identification number(s) for the author(s) of this article can be found under <https://doi.org/10.1002/adma.202108183>.

© 2022 The Authors. Advanced Materials published by Wiley-VCH GmbH. This is an open access article under the terms of the Creative Commons Attribution License, which permits use, distribution and reproduction in any medium, provided the original work is properly cited.

DOI: 10.1002/adma.202108183

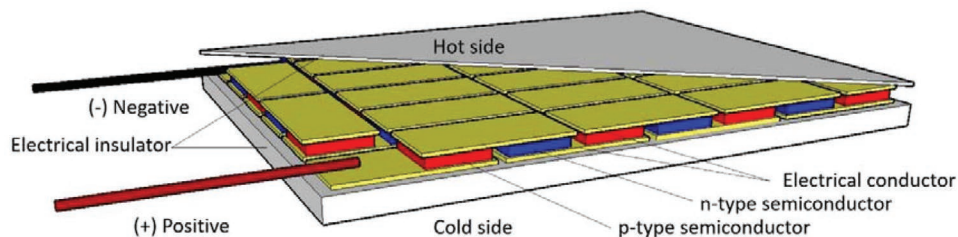


Figure 1. Diagram of a typical design of a thermoelectric generator, with alternating p- and n-type legs connected electrically in series but thermally in parallel. The legs are connected together with an electrical conductor and the top and the bottom of the device are covered in an electrical insulator with high thermal conductivity (e.g., alumina).

device's efficiency, a ZT "average" is required which takes into account the material properties of both the n- and p- type material (Equation 4).^[10,11] This "average" ZT can be seen in Equation 5,^[4] which shows the maximum efficiency of a thermoelectric generator considering Carnot efficiency and material property limitations. **Figure 2** uses Equation 5 to show what efficiencies can be achieved with different ZT s.

$$Z\bar{T} = \frac{(S_p - S_n)^2 \bar{T}}{(\sqrt{\rho_n \kappa_n} + \sqrt{\rho_p \kappa_p})^2} \quad (4)$$

$$\eta_{\max} = \frac{T_H - T_C}{T_H} \frac{\sqrt{1 + Z\bar{T}} - 1}{\sqrt{1 + Z\bar{T}} + \frac{T_C}{T_H}} \quad (5)$$

Figure 2 reveals that with the right temperatures, a ZT of 1 can yield efficiencies comparable to other renewable technologies.^[12] While wind and solar renewable technologies have become ubiquitous in nations striving to become carbon neutral, thermoelectrics can only be found in niche applications, such as space,^[13] watches,^[14] or in Peltier coolers.^[15] This in part can be rationalized when realizing the high cost of manufacturing thermoelectric devices, which contributes toward

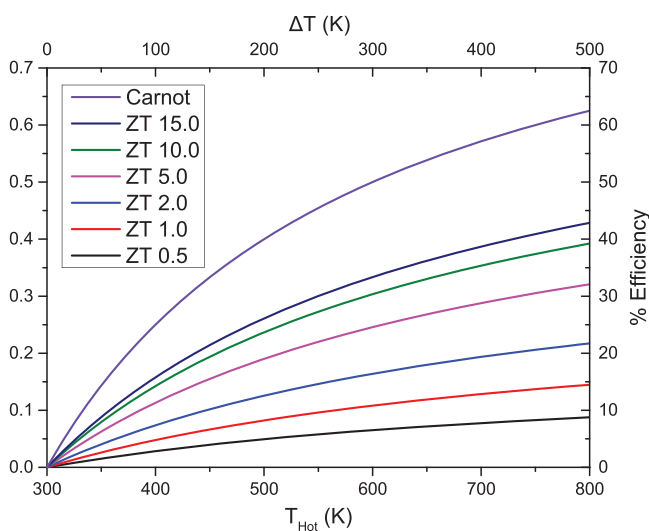


Figure 2. Efficiency of thermoelectric materials with different ZT values at different ΔT values, with a cold side temperature of 300 K. Carnot efficiency is also shown, which is equivocal to a ZT of infinity. Efficiencies are calculated using Equation 5.

the cost of \$0.80 per kWh for thermoelectric generators,^[16] compared to \$0.089 per kWh and \$0.084 per kWh for PV and wind turbines respectively.^[17] If thermoelectrics are ever to see widespread use the cost of manufacturing thermoelectric generators and thus the cost per kWh of energy harvested needs to be reduced.

One way to reduce the cost of heat to electrical harvesting is to reduce the cost of manufacturing thermoelectric materials. Current commercial devices use hot pressing, spark plasma sintering, or a combination of both, to manufacture thermoelectric materials. These techniques require high pressure, high temperature, expensive equipment and considerable manufacturing times. Printing, in contrast, can be done in ambient conditions, achieve rapid manufacturing speeds and use relatively cheap equipment. There has been a significant advancement of printed thermoelectrics in the recent past. Printing techniques (**Figure 3**) that have been studied include screen printing, inkjet printing, dispenser printing and more recently 3D printing/pseudo 3D printing.

Spin coating (Figure 3a, a solution-process technique) while not strictly classed as a printing technique is often used in the laboratory to test the feasibility of ink formulations before scale-up using a different printing technique. The ink formulation is applied to the center of a substrate that is still or spinning at a slow speed. Once the ink is applied to the substrate, the substrate is set to spin at a high speed. There can be multiple spin speeds used with various acceleration rates. The process when done properly, results in uniform films. The limitations with this technique are that it requires a flat substrate and only results in thin films.

Screen printing (Figure 3b) has traditionally been used for commercially printed products such as posters and textile products, but has recently found new usage in being used to produce printed circuit boards (PCBs),^[18] and other electrical products such as printed resistors and dye-sensitized and perovskite solar cells.^[19–23] Screen printing is a technique where ink is transferred onto a substrate through a mesh, apart from in areas of the mesh that are impermeable due to a blocking stencil. A squeegee or blade is moved over the screen to fill the open apertures with ink, then a reverse stroke allows the screen to momentarily touch the substrate along the line of contact. This results in the ink wetting the substrate and being pulled out of the mesh apertures as the screen retreats after the blade has passed. A wide range of thicknesses can be printed, from a few μm to several hundred. Any flat solid substrate can be used, with typical examples being aluminum, glass, or more generally with thermoelectrics, polyimide. A wide range of inks can also be employed. Limitations include restricted feature

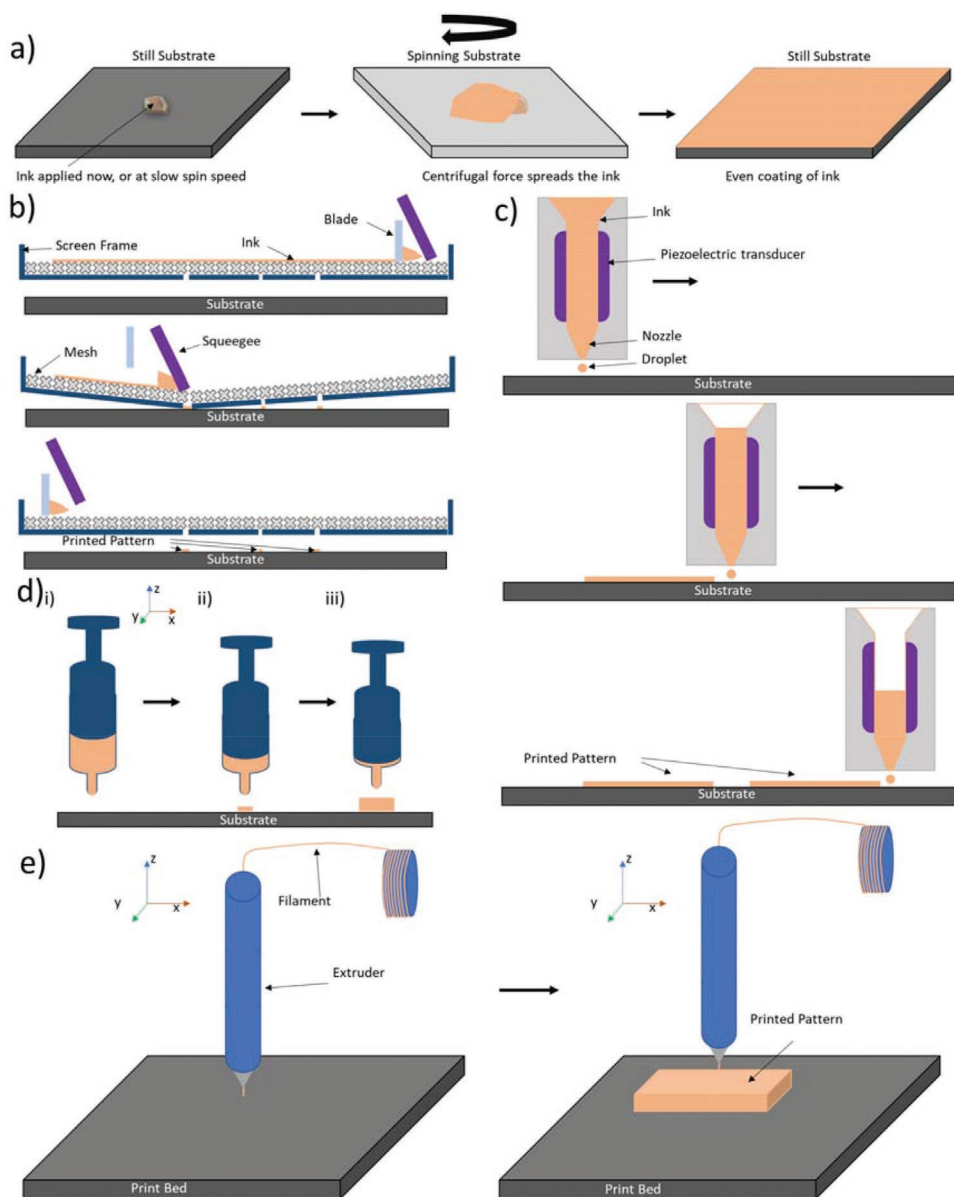


Figure 3. Schematic diagrams of: a) spin coating, and various printing techniques: b) screen printing, c) ink jet printing, and the printing techniques capable of 3D printing: d) dispenser printing (direct ink writing/microextrusion), e) fuse deposition modeling (FDM).

size, which may lead to issues in the final product if intricate parts are needed; and the drying process which may lead to shrinkage and a high surface roughness, possibly leading to faults or defects in the final product. Although the inks used can have a wide range of viscosities, typically, higher viscosity inks are used (typically 1 to 10 Pa s) than those used in other printing techniques.^[24,25] Films that are produced in this fashion typically show lower electrical conductivity due to surface oxidation of the films, and due to the thermoelectric particles not being molten, so electrical pathways are harder to cross.^[18,26]

Inkjet printing (Figure 3c) is a technique that involves building up an image on a substrate in a drop by drop fashion, controlled electronically. Drop on demand (DOD) is the most popular type, with other types being continuous inkjet printing.^[27] DOD is where the ink is pushed into a chamber

by a voltage-activated piezoelectric diaphragm. A change of voltage can cause the diaphragm to contract, this change of volume causes a higher pressure within the diaphragm compared to within the printing chamber. This pressure differential pushes ink into the chamber (change of volume equal to the volume of ink dropped). When the voltage change is reversed, the volume of the piezoelectric diaphragm relaxes to allow in air so that more ink can be printed on the next activation of the piezoelectric diaphragm. Ink droplets are only produced when needed, so there is very little ink wastage. In inkjet printing, however, the printer head is susceptible to clogging and damage if the particle size within the ink is close to the diameter of the nozzle, and if a larger nozzle diameter is used, the resolution of the deposited image may be reduced. Inkjet inks are also prone to the “coffee ring” effect upon being deposited and dried,

where the solute within the deposited ink flows to the outside of the deposited droplet via capillary effects as it dries, causing the inside of the droplet to be thinner, this can cause uneven characteristics within the ink.^[28] Films and devices produced via inkjet printing are also very thin ($\approx 0.4\text{--}1.6\ \mu\text{m}$).^[29]

Dispenser printing (Figure 3d) is a simple process that consists of a syringe that deposits ink onto a substrate through a needle.^[30] This printing method can produce thicker films up to several hundred microns with multiple passes,^[31] allowing 3D samples to be made. The printing equipment itself involves an ink reservoir within a chamber, and at the bottom of this chamber is a needle-like structure, or a nozzle. Force is applied to the ink reservoir in a downward motion and the ink is then deposited out of the nozzle or needle onto the substrate. The force needed to push the ink through the needle or nozzle is typically achieved via one of three methods: Piston, where a mechanical piston forces itself down onto the ink; Screw, where a mechanical screw device within the reservoir turns and forces ink down to the bottom to be deposited; or Pneumatic, where air pressure forces down on the ink.^[32] The geometry of the device that is to be built is achieved by moving the substrate or the printer head, which can be moved in the x , y , and z axes. A wide range of viscosities can be printed ($0.1\text{--}10\ \text{Pa s}$) by varying nozzle size, pressure, and dispensing time.^[33] Colloidal inks have been used to achieve the desired viscoelasticity for 3D dispenser printing.^[34] The main disadvantage of this method is that it is relatively slow per unit area of substrate compared to other methods outlined, as well as low printing resolution.^[35]

The 3D printing technique of fuse deposition modeling (Figure 3e) involves the construction of fully 3D objects. Traditionally materials such as polylactic acid (PLA) or acrylonitrile butadiene styrene (ABS) are used as the filament (feedstock), in fused deposition modeling 3D printers. If used for thermoelectrics then the ink must also contain a binder (such as cellulose) that would give the ink appropriate viscoelastic properties when printing, but not after printing when being used in a thermoelectric application. The 3D printing processes are typically automated by the desired 3D object being constructed on CAD software, which is subsequently broken down into different layers. The 3D printer then deposits the ink via a moveable printer head in these predetermined layers, one on top of the other to eventually make the 3D shape on a stage, without the need for a substrate. If a printing design results in overhanging within the geometry, then temporary support structures can be built under the overhang to support the structure while printing, these can then be removed post-printing. This method, unlike the other printing techniques mentioned, can produce 3D shapes not limited in thickness. Printed objects can be produced that are made to fit on nonflat surfaces (e.g., a cylinder), to make custom-shaped thermoelectric modules to fit bespoke applications (e.g., pipes).^[34] 3D printing of thermoelectrics is currently limited by the production of filaments. Pseudo 3D printing (which can also be considered additive manufacturing) is fundamentally the same as 3D printing, but the addition of the different layers (typically a couple of millimeters at a time) is supported with a sacrificial mold. After curing the mold is removed, leaving behind one solid piece which takes the mold's shape.^[36,37]

In recent years there have been many reviews covering different aspects of thermoelectrics, from materials,^[38]

historical footprints,^[39] advanced designs,^[40] unconventional materials,^[41] wearables,^[42] and high performance.^[43] While these reviews may cover research that uses printing to a certain degree, this was not their focus. This review gives an in depth look at printed thermoelectrics, with particular attention to the significant progress that has been made, especially in the last decade. Initially, the review covers chalcogenide thermoelectrics, starting with tellurides. The review then moves onto all other inorganic thermoelectric groups, before moving onto printed organic thermoelectrics such as PEDOT:PSS and CNTs.

2. Chalcogenides

Perhaps the most promising of the thermoelectric material groups, and the most widely explored are the chalcogenides. This group are compounds that contain at least one chalcogen element (group 16), that element being commonly selenium or tellurium.

2.1. Tellurides

The most researched thermoelectric element is tellurium. Tellurium is the heaviest nonradioactive chalcogen atom. Tellurium's relative mass gives it a reduced lattice thermal conductivity, which is a key characteristic for selecting materials to manufacture thermoelectric generators (TEGs) and thermoelectric materials, as a low lattice thermal conductivity can produce a high ZT value. Telluride compounds are also less ionic than other chalcogen compounds which leads to an increase in carrier mobility, which in turn increases electrical conductivity and therefore an increase ZT .^[44] The most commonly used of the tellurium based compounds is bismuth telluride (Bi_2Te_3) and its respective derivatives. A ZT of 1 at room temperature was demonstrated using Bi_2Te_3 in the 1950s.^[5] During the same period, PbTe was also studied for medium-temperature applications ($500\text{--}850\ \text{K}$), with a ZT of over 1 being demonstrated.^[6]

Different telluride derivatives have different peak ZT and hence operating temperatures. Amongst the best ZT for low-temperature applications, is the work done by Yamashita et al. who used induction melting to produce p-type $(\text{Bi}_{0.25}\text{Sb}_{0.75})_2\text{Te}_3$ doped with 8 wt% excess tellurium and n-type $\text{Bi}_2(\text{Te}_{0.94}\text{Se}_{0.06})_3$ doped with 0.07 wt% Iodine, 0.02 wt% tellurium, and 0.03 wt% CuBr . These materials produced ZT values of 1.41 and 1.13 for p- and n-type, respectively, at 308 K.^[45] For increased temperatures, lead telluride (PbTe) based materials have been widely explored. Fu et al. made $\text{PbTe}_{0.8}\text{Se}_{0.2}$ with 8% MgTe based alloy which achieved a ZT of 2.2 at 820 K,^[46] which is among the highest ZT s ever reported. The materials were prepared, however, by melting the constituent powders in a vacuum-sealed furnace for 10 h at 1273 K, followed by annealing at 873 K for 4 d, which resulted in homogeneous ingots being formed. These ingots were then ground back down into powder form, before being compacted by spark plasma sintering (SPS) at 823 K under 60 MPa in a vacuum.

Telluride-based compounds do show promise, however, the aforementioned ZT values were obtained via nonprinting energy-intensive and time-consuming techniques. The current

literature surrounding printed telluride compounds has produced ZT values that are, for the most part, considerably lower.

2.1.1. Screen Printed Tellurides

The thermoelectric properties of screen-printed tellurides reported in the literature are shown in **Figure 4** (also Table S1, Supporting Information), and examples of screen-printed thermoelectric modules are highlighted in **Figure 5**. All printed Te-based thermoelectric generators that report a power output are summarized in **Table 1**.

Weber et al. published using this technique for thermoelectrics in 2006.^[18] In this paper, $\text{Bi}_{0.85}\text{Sb}_{0.15}$ was used as the n-type material and Sb was used as the p-type material. Both materials were combined with ethylene glycol and were printed on polyimide with a thickness in the range of 1–3 μm . The electrical conductivity was measured to be 10 and 100 S cm^{-1} for n-type and p-type respectively. Other individual characteristics were not measured, but the thermopower for a $\text{Bi}_{0.85}\text{Sb}_{0.15}$ –Sb thermocouple was, with a reported value of 97 $\mu\text{V K}^{-1}$. A maximum theoretical thermopower of 141 $\mu\text{V K}^{-1}$ was stated by the authors. Many improvements were suggested that could be done such as finding the ideal particle size, reducing the native oxide surface as much as possible, looking for the best ratio of metal powder and binder and searching for the best annealing temperature, factors which are well known to be vital. Due to the lack of proper Seebeck coefficient measurements and a lack of thermal conductivity measurements, no ZT values were reported.

Bi_2Te_3 -based compounds have since also been screen printed. In 2010, Navone et al. investigated screen printed Bi_2Te_3 .^[47] $\text{Bi}_2\text{Sb}_{0.3}\text{Te}_{2.7}$ was used as the n-type material and $\text{Bi}_{0.5}\text{Sb}_{1.5}\text{Te}_3$ as the p-type material, both were combined with polystyrene and toluene. These were printed on alumina (Al_2O_3) for a rigid substrate and on polyethylene naphthalate (PEN) for a flexible substrate. The films had thicknesses of at least 100 μm . In this work, the two materials were again combined and used to make a thermocouple. A 15 cm long TEG was made that consisted of five thermocouples connected in series, although a power output for the device was not stated. To improve film connection and particle unity, uniaxial pressure of 15 and 50 bar were employed to the rigid and flexible devices, respectively. This pressure improved thermoelectric performance significantly. Films that were printed onto the Al_2O_3 were annealed at 523 K in an argon atmosphere for 10 h meaning this postprinting process could potentially be energy intensive. The individual electrical conductivities for the materials printed on Al_2O_3 were reported to be 31.5 and 7.8 S cm^{-1} for n-type and p-type, respectively, the thermocouple device made had an electrical resistance of 190 Ω . The thermopower of the thermocouple was reported as 123 $\mu\text{V K}^{-1}$ at a ΔT of 50 K, an improvement from the work conducted by Weber et al.^[18] An electromotive force (EMF) of 30 mV was measured for the same temperature differential (50 K). The thermal treatments used on Al_2O_3 substrates were not possible for the flexible PEN films as this would lead to degradation of the substrate, so films that were printed on the flexible substrate underwent laser annealing using a 473 mJ cm^{-2} Tamarack excimer laser. At 100 pulses, electrical

conductivity was about 8 S cm^{-1} , and films were noted to be crack free and damage free. A Seebeck coefficient of 160 $\mu\text{V K}^{-1}$ was measured, but this decreased with the number of pulses (up to 80 pulses) where it would stabilize at 90 $\mu\text{V K}^{-1}$. The power factor for half a thermocouple (single thermoelectric leg) with the laser-treated samples was measured as 0.06 $\mu\text{W m}^{-1} \text{K}^{-2}$. While these values were an improvement over the previous work,^[18] they were still small compared to values that can be obtained in bulk materials produced by more energy-intensive means.

In 2012 optimization of post-screen-printing annealing was investigated. We et al. did this using n-type Bi_2Te_3 thick films.^[52] They found that ZT and power factor values could be optimized if annealed in a nitrogen environment, at 773 K for 15 min. Beyond 773 K the electrical conductivity rapidly dropped, and this is likely due to the excess evaporation of metal powders. Bi and Te powders, therefore, were placed next to the samples within the annealing chamber. With these powders present, the electrical conductivity and power factor increase further with a longer annealing times. It was stated that the presence of the Te and Bi powders within the annealing chamber would suppress the evaporation of the same materials within the film. With these annealing parameters, a room temperature ZT value of 0.61 was achieved. The power factor, electrical conductivity, and Seebeck coefficient were 480 $\mu\text{W m}^{-1} \text{K}^{-2}$, 260 S cm^{-1} and $\approx 137 \mu\text{V K}^{-1}$ respectively when annealed at 773 K. When further annealed for 10 min with ambient powders of Bi and Te the power factor increased to 2100 $\mu\text{W m}^{-1} \text{K}^{-2}$, while having a thermal conductivity of 1.0 $\text{W m}^{-1} \text{K}^{-1}$. We et al. also stated that thermal conductivity does not seem to be affected significantly by annealing time.

In 2013, Cao et al. made a Bi_2Te_3 – Sb_2Te_3 based TEG (Figure 5a).^[26] Here the n-type material was $\text{Bi}_{1.8}\text{Te}_{3.2}$ and the p-type was Sb_2Te_3 and they were combined with epoxy and printed on polyimide. The dimensions of each leg of the TEG were 39.3 mm \times 3 mm with thicknesses of 67 μm and 62 μm for the n-type and p-type, respectively. A single thermocouple of these dimensions produced a voltage of 6 mV and had a peak output power of 48 nW at $\Delta T = 20$ K. The power produced, however, decreased to 23 nW after 50 days of testing. The Seebeck coefficient of this thermocouple was reported to be 272 (± 10) $\mu\text{V K}^{-1}$. The individual Seebeck coefficients for materials, at room temperatures, were -126.5 (± 7.5) $\mu\text{V K}^{-1}$ and 131 (± 3) $\mu\text{V K}^{-1}$ for the n-type and p-type materials, respectively. The Seebeck coefficient value obtained for the $\text{Bi}_{1.8}\text{Te}_{3.2}$ was considerably lower than the bulk value of $-227 \mu\text{V K}^{-1}$ quoted by Cao et al. The value obtained for Sb_2Te_3 , however, is higher than the quoted bulk value (110 $\mu\text{V K}^{-1}$). Cao et al. stated the reason for the low power output was due to the high resistivity of the $\text{Bi}_{1.8}\text{Te}_{3.2}$ film, from the many pores in between particles of the $\text{Bi}_{1.8}\text{Te}_{3.2}$. This caused a large contact resistance between the particles and thus in the film as a whole. Oxidation of the $\text{Bi}_{1.8}\text{Te}_{3.2}$ film was also mentioned as a possible source of higher resistivity. Oxidation of bismuth tellurides is well known, We et al. in 2012 showed that annealing in a N_2 environment at higher temperatures can correct for this.^[52] As is common for thermoelectric films, the thermal conductivity was not measured, thus no ZT value was obtained.

In 2014, Kim et al. screen printed on glass fabric 500 μm thick Bi_2Te_3 and Sb_2Te_3 as n-type and p-type materials

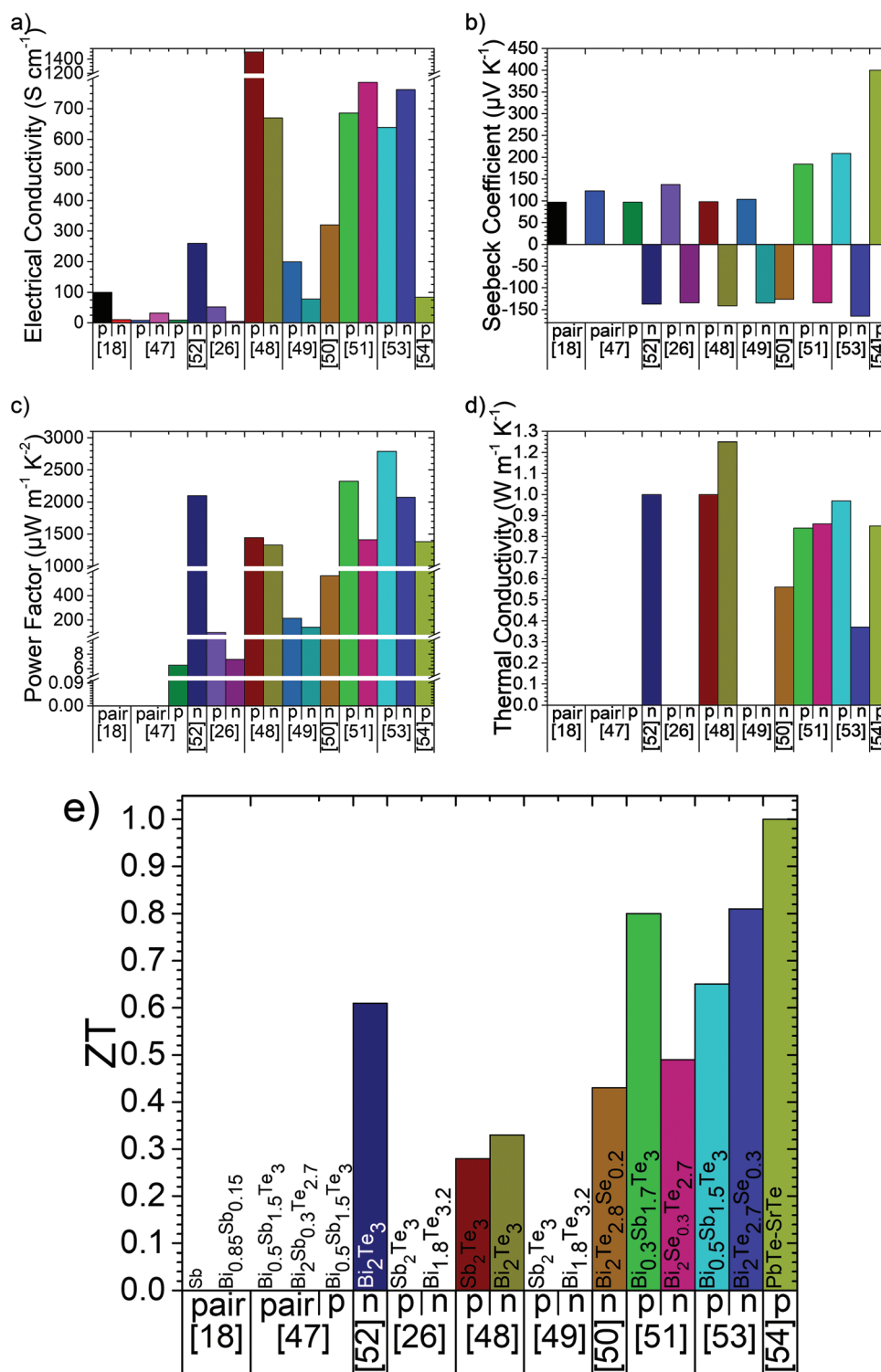


Figure 4. Thermoelectric properties of screen-printed tellurides (materials are labeled in part e). Values presented represent the sample and temperature where the peak ZT value was observed, if ZT was not reported then values represent the peak power factor measured: a) electrical conductivity, b) Seebeck coefficient, c) power factor, d) thermal conductivity and e) ZT. This data is also represented in Table S1 (Supporting Information).

respectively.^[48] These materials were bonded by an unspecified organic binder. The ZT values of both materials were relatively low compared to bulk counterparts and were 0.33 and 0.28 for

the n-type and p-type, respectively. The electrical conductivity, thermal conductivity, Seebeck coefficient, and power factor for the n-type and p-type were 670 and 1500 $S\ cm^{-1}$, 1.25 and

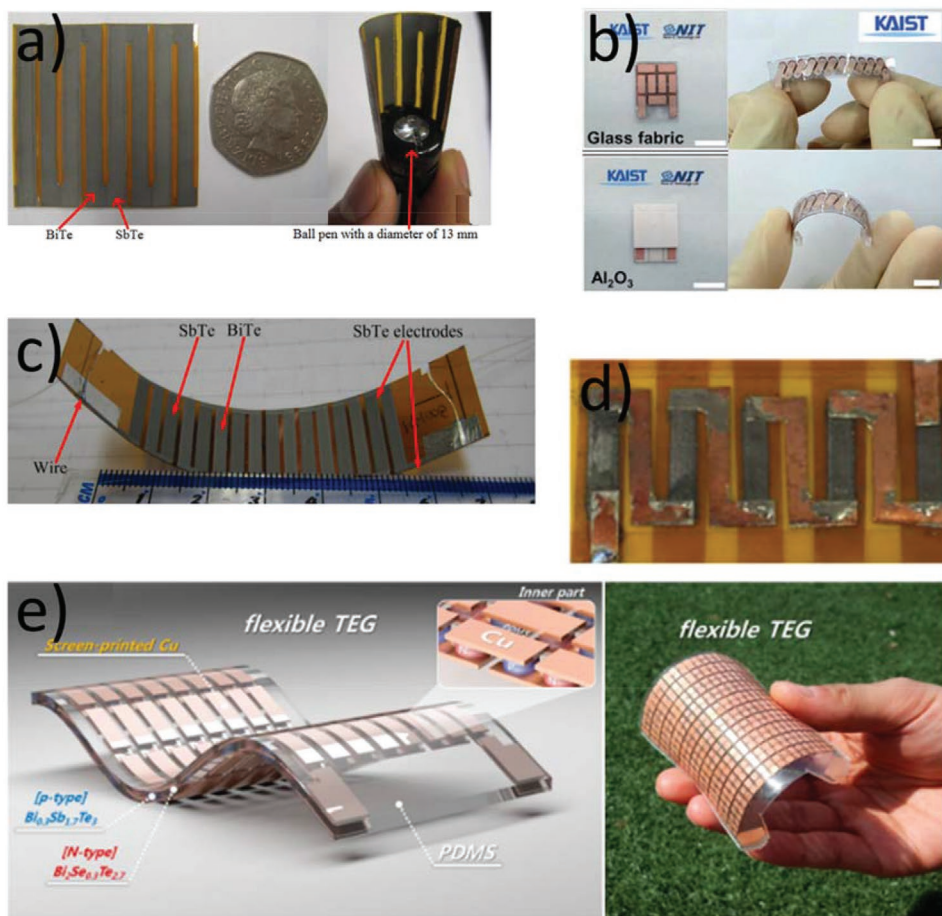


Figure 5. Screen printed thermoelectric modules. a) Printed $\text{Bi}_2\text{Te}_3/\text{Sb}_2\text{Te}_3$ thermocouples next to a 50 pence coin for comparison, also shown is the sample rolled onto a 13 mm ball point pen. Reproduced under the terms of an Attribution 3.0 International (CC BY 3.0) license.^[26] Copyright 2013, The Authors. Published by IOP. b) printed $\text{Bi}_2\text{Te}_3/\text{Sb}_2\text{Te}_3$ thermoelectric generators printed on Al_2O_3 and flexible glass fabric substrates. Reproduced with permission.^[48] Copyright 2014, RSC. c) Printed $\text{Bi}_{1.8}\text{Te}_{3.2}/\text{Sb}_2\text{Te}_3$ thermocouples on a Kapton substrate. Reproduced with permission.^[49] Copyright 2016, Elsevier. d) A TEG device consisting of 5 n-type elements of printed $\text{Bi}_2\text{Te}_{2.8}\text{Se}_{0.2}$ nanocrystals on flexible polyimide. Reproduced under terms of an Attribution 4.0 International (CC BY 4.0) license.^[50] Copyright 2016, The Authors. Published by Springer Nature. e) schematic illustration and photo of a $\text{Bi}_2\text{Se}_{0.3}\text{Te}_{2.7}/\text{Bi}_{0.3}\text{Sb}_{1.7}\text{Te}_3$ TEG produced using screen printing along with a laser multiscanning lift-off process. Reproduced with permission.^[51] Copyright 2016, ACS.

$1 \text{ W m}^{-1} \text{ K}^{-1}$, -141 and $98 \mu\text{V K}^{-1}$ (reported to be similar to hot pressed samples^[48]), and 1332 and $1441 \mu\text{W m}^{-1} \text{ K}^{-2}$ respectively. All the characteristics that were reported were measured as a function of the thickness ratio. This is the ratio between the printed thermoelectric film and the glass fabric substrate. This thickness ratio was controlled by varying the thickness of thermoelectric materials, with the glass fabric thickness fixed at $25 \mu\text{m}$. Seebeck coefficient and ZT values remained largely unchanged with changing ratios, but electrical and thermal conductivity would increase. This is due to the increasing ratio of thermoelectric material to insulating glass fabric presents less of a layer where the flow of phonons and charge carriers are being disrupted by bundles of glass fibers. A prototype TEG (Figure 5b) was made which consisted of eight thermocouples of Bi_2Te_3 and Sb_2Te_3 thick films with dimensions $15 \times 20 \times 0.5 \text{ mm}$ and was printed on Al_2O_3 . This TEG produced an open-circuit voltage of 90 mV at a ΔT of 50 K . The Al_2O_3 substrate would act as a heat

sink, which lead to a enhanced power density of 3.8 mW cm^{-2} at a ΔT of 50 K . The research team noted that the devices that were fabricated were very light (approximately 0.13 g cm^{-2}) and had a large specific power output of 28 mW g^{-1} at a $\Delta T = 50 \text{ K}$. A TEG device was made to demonstrate the possibility of energy harvesting from the heat that human bodies produce (Figure 5b). A simple glass fabric TEG with 11 TE couples was made and placed on human skin. This TEG produced an open-circuit voltage of 2.9 mV and a power output of $3 \mu\text{W}$ with an ambient air temperature of 288 K ($15 \text{ }^\circ\text{C}$).

In 2015 Cao et al. continued their work on printed TEGs. The materials were n-type $\text{Bi}_{1.8}\text{Te}_{3.2}$ and p-type Sb_2Te_3 much like their previous work, and the goal was also similar, to create a TEG device with these materials.^[49] These were again printed on polyimide and had dimensions of $20 \text{ mm} \times 2 \text{ mm}$ and had thicknesses ranging from 70.5 to $78 \mu\text{m}$. Each TEG (Figure 5c) produced had eight of these thermocouples connected by an

Table 1. Summation of Te based printed thermoelectric generators that report power outputs.

Material	Printing technique	Substrate	Thickness [mm]	Power [μW]	Power density [mW cm^{-2}]	Cure time [min]	Cure temperature [K]	Refs.
$\text{Sb}_2\text{Te}_3/\text{Bi}_{1.8}\text{Te}_{3.2}$	Screen	Kapton	0.067	0.048	N/A	180	523	[26]
$\text{Sb}_2\text{Te}_3/\text{Bi}_2\text{Te}_3$ with organic binder	Screen	Glass fabric	0.5	N/A	3.8	N/A	803	[48]
$\text{Sb}_2\text{Te}_3/\text{Bi}_{1.8}\text{Te}_{3.2}$ with epoxy	Screen	Polyimide	0.078	0.444	N/A	180	523	[49]
$\text{Bi}_2\text{Te}_{2.8}\text{Se}_{0.2}$ with α -terpineol and Disperbyk-110	Screen	Polyimide	0.1	0.0041	4.1	45	703	[50]
$\text{Bi}_{0.3}\text{Sb}_{1.7}\text{Te}_3/\text{Bi}_2\text{Se}_{0.3}\text{Te}_{2.7}$	Screen	$\text{SiO}_2/\text{a-Si}/\text{quartz}$	0.65	76480	4.78	N/A	N/A	[51]
Bi_2Te_3 with PVA	Shadow Mask	PET	0.265	N/A	0.009	120	353	[55]
$\text{Sb}_2\text{Te}_3/\text{Bi}_2\text{Te}_3$ with epoxy	Dispenser	Polyimide	0.12	0.85	N/A	N/A	473	[57]
$\text{Sb}_2\text{Te}_3/\text{Bi}_2\text{Te}_3$ with epoxy	Dispenser	Polyimide/glass	0.2	10.5	75×10^{-3}	N/A	523	[58]
Se doped Bi_2Te_3 with epoxy	Dispenser	Polyimide	0.2	1.6	N/A	720	523	[60]
Bi_2Te_3 with epoxy	Dispenser	Polyimide	0.1-0.12	25	0.13	720	623	[61]
$\text{Bi}_{0.5}\text{Sb}_{1.5}\text{Te}_3/\text{Bi}$ with epoxy	Dispenser	Glass	N/A	130	1.23	720	523	[62]
$\text{Bi}_{0.5}\text{Sb}_{1.5}\text{Te}_3/\text{Bi}_2\text{Te}_{2.75}\text{Se}_{0.25}$ with epoxy	Dispenser	Free standing	4.4	0.126	N/A	N/A	N/A	[68]
$\text{Sb}_{1.5}\text{Bi}_{0.5}\text{Te}_3/\text{Bi}_2\text{Te}_{2.7}\text{Se}_{0.3}$	Inkjet	Glass/polyimide	150 layers ^{a)}	341	N/A	30	673	[63]
$\text{Bi}_{0.5}\text{Sb}_{1.5}\text{Te}_3/\text{Bi}_2\text{Te}_3$	Inkjet	Polyimide	0.00156	0.127	N/A	120	723	[64]
$\text{Bi}_{0.4}\text{Sb}_{1.6}\text{Te}_3/\text{Bi}_2\text{Te}_{2.7}\text{Se}_{0.3}$ with Sb_2Te_3	3D	N/A	1.5–2.0	1620	1.42	60	723	[34]
$\text{Bi}_{0.55}\text{Sb}_{1.45}\text{Te}_3/\text{Bi}_2\text{Te}_{2.7}\text{Se}_{0.3}$ with $\text{Sb}_2\text{Te}_4^{2-}$	3D	N/A	0.35	2.8	0.479	30	723	[66]
$\text{Pb}_{0.98}\text{Na}_{0.02}\text{Te}/\text{Pb}_{0.98}\text{Sb}_{0.02}\text{Te}$	3D	N/A	2	216300	153.7	3150	373-1023	[67]
$\text{Bi}_{0.4}\text{Sb}_{1.6}\text{Te}_3/\text{Bi}_2\text{Te}_{2.7}\text{Se}_{0.3}$ ^{b)}	Laser	$\text{Bi}_{0.4}\text{Sb}_{1.6}\text{Te}_3$	1.6	1450000 ^{b)}	90.6 ^{b)}	1440	673	[71]

^{a)}No thickness was given so number of layers of print is shown;; ^{b)}The $\text{Bi}_2\text{Te}_{2.7}\text{Se}_{0.3}$ n-type legs were not printed.

electrode. SbTe was used as the electrode material as it had an inherently lower contact resistance than the other material that was tested (silver paste). In this body of work, the effect of cold isostatic pressing (CIP) and two different binder systems were investigated. The binders were 4,4'-isopropylidenediphenol-epichlorohydrin (BPA-ECH) based epoxy (3M) and epichlorohydrin-polyglycol (ECH-PG) based epoxy (Dow Chemical). The highest power factor achieved for the $\text{Bi}_{1.8}\text{Te}_{3.2}$ was $141 \mu\text{W K}^{-2} \text{m}^{-1}$ which contained binder ECH-EG and was not pressed, although pressing did not negatively affect the performance, while the highest power factor the Sb_2Te_3 films were $215 \mu\text{W K}^{-2} \text{m}^{-1}$ which contained binder BPA-ECH and was pressed. The individual Seebeck coefficients with the same parameters were reported to be -134.38 and $103.67 \mu\text{V K}^{-1}$ for the n-type and p-type, respectively. These two power factor values were achieved because of the lower resistivity of the respective combination of materials and processes. Ignoring the effects of pressing, ECH-EG yielded lower resistivity than BPA-ECH. This is because BPA-ECH required butyl carbitol acetate thinner which was added and readily absorbed moisture within the atmosphere, this additional moisture increased oxidation and subsequently increased resistivity. ECH-EG required no additional thinner, so this problem was not present. Within the samples that had undergone cold isostatic pressing after printing, there were less voids present in the samples. This led to a decrease contact resistance between the particles within the thermoelectric material. The Seebeck coefficient of TEGs made with these materials and processes were also investigated using BPA-ECH. The Seebeck coefficient for TEGs made from a single thermocouple with BPA-ECH ranged from 193 to

$227 \mu\text{V K}^{-1}$. At a ΔT of 20 K, while the power output was measured to be 142 nW after cold isostatic pressing. ECH-EG was then added which was able to decrease the resistivity of the $\text{Bi}_{1.8}\text{Te}_{3.2}$ film and increased the power output to 444 nW. The optimum combination of materials and processes for TEG manufacturing is therefore n-type $\text{Bi}_{1.8}\text{Te}_{3.2}$ with ECH-EG, p-type Sb_2Te_3 with BPA-ECH, with SbTe contact electrodes, with the whole assembly undergoing cold isostatic pressing. Cold isostatic pressing (CIP) does not improve or deteriorate the performance of $\text{Bi}_{1.8}\text{Te}_{3.2}$, while yielding a performance improvement in Sb_2Te_3 sections, therefore, justifying the use of CIP.

In 2016, Varghese et al. showed that nanocrystals could be screen printed to make highly flexible thermoelectric materials.^[50] In this work, n-type $\text{Bi}_2\text{Te}_{2.8}\text{Se}_{0.2}$ nanocrystals were printed onto polyimide. A ZT of 0.43 at 448 K was obtained, which is not as high as bulk materials, however, the devices made offer much more flexibility. This was evidenced by a negligible change in electrical conductivity after 150 bending cycles, indicating the electrical integrity of the sample was intact. The power factor of the sample was reported as $560 \mu\text{W m}^{-1} \text{K}^{-2}$. The lattice thermal conductivity was $0.41 \text{ W m}^{-1} \text{K}^{-1}$, which is lower compared to that of the pellet samples ($0.66 \text{ W m}^{-1} \text{K}^{-1}$) which were also made in this work. The lower thermal conductivity stems from the nanoscale grains and porosities from nanocrystals. The printed films were used to manufacture a TEG device (Figure 5d) which consisted of 5 n-type elements. This TEG device generated a power density of 4.1 mW cm^{-2} with a ΔT of 60 K. The electrical conductivity of the samples, however, even though it did not degrade after bending, was still considerably lower than that of pellet samples ($\approx 53\%$ lower).

Also in 2016, Kim et al. used screen printing along with a laser multiscanning (LMS) lift-off process.^[51] The materials used here were n-type $\text{Bi}_2\text{Se}_{0.3}\text{Te}_{2.7}$ and p-type $\text{Bi}_{0.3}\text{Sb}_{1.7}\text{Te}_3$. These materials were printed on a SiO_2 substrate using an unspecified organic binder and had a thickness of 650 μm . The LMS lift-off process essentially peels the flexible thermoelectric material from the substrate after it has been screen printed. The advantage of this extraction method is that one can separate the flexible thermoelectric material from the substrate without degradation, as the laser uses a mixture of chlorine and xenon gas (wavelength 308 nm), which selectively reacts with the substrate (a-Si). This LMS process also allowed Kim et al. to use high-temperature annealing conditions (over 973 K), which helped with thermoelectric properties. The laser shots used had high energy density of 700 mJ cm^{-2} , a frequency of 20 Hz, and a time duration of 30 ns. The Seebeck coefficient, electrical conductivity, and thermal conductivity were -134 and 184 $\mu\text{V K}^{-1}$, 786 and 686 S cm^{-1} , and 0.86 and 0.84 $\text{W m}^{-1} \text{K}^{-1}$ for the n-type and p-type, respectively. The resulting ZT values were reported to be 0.49 for the n-type material, and 0.80 for the p-type material at 300 K. As is common with printed thermoelectrics materials a decreased electrical conductivity compared to bulk counterparts was observed. This is due to the porosity of the screen-printed films, the thermal conductivity is also lower for the same reason. In this body of work a freestanding TEG device was also built using the same materials. The TEG (Figure 5e) consisted of 72 TE couples with dimensions 40 mm \times 40 mm \times 0.8 mm. The TEG achieved a maximum output power density of 4.78 mW cm^{-2} at a ΔT of 25 K and an open-circuit voltage of 500 mV. The device weighed 3.7 g, and so generated a power per unit weight of 20.8 mW g^{-1} .

Shin et al. achieved a higher ZT value in 2017 by screen printing $\text{Bi}_{0.5}\text{Sb}_{1.5}\text{Te}_3$ and $\text{Bi}_2\text{Te}_{2.7}\text{Se}_{0.3}$ for p- and n-type, respectively. The goal was to create a material that in theory could be used to create wearable devices for energy harvesting.^[53] $\text{Bi}_{0.5}\text{Sb}_{1.5}\text{Te}_3$ and $\text{Bi}_2\text{Te}_{2.7}\text{Se}_{0.3}$ were combined with methyl cellulose. These inks were printed on a fiberglass fabric structure and uniaxial hot pressing was conducted after the films were printed because of the poor conductivity of the as printed films. The low conductivity was due to loose thermoelectric particles in the film, and the hot pressing helped alleviate the problem by densifying the films. The printed modules had thicknesses ranging from 10 to 700 μm . The electrical conductivity, thermal conductivity, and Seebeck coefficient of the p- and n-type were reported to be 639 and 763 S cm^{-1} , 0.97 and 0.37 $\text{W m}^{-1} \text{K}^{-1}$ and 209 and -165 $\mu\text{V K}^{-1}$ respectively. The room temperature ZT values were 0.65 and 0.81 for the p-type and n-type, respectively.

One of the highest ZT s achieved in a printed tellurides was reported in 2018. In this paper, Han et al. report a ZT of >1 in the medium temperature PbTe-SrTe material, with added 2 wt% of tellurium.^[54] The samples had a thickness ranging from 20 to 30 μm . The electrical conductivity, Seebeck coefficient and the power factor of the produced samples were 84 S cm^{-1} , $\approx 400 \mu\text{V K}^{-1}$, and 1380 $\mu\text{W m}^{-1} \text{K}^{-2}$ respectively, all recorded at 623 K. Scanning electron microscopy (SEM) showed the addition of the extra tellurium into the material drastically reduced the porosity of the samples. The additional tellurium also prevented the charge carriers getting trapped via oxidation. One additional tellurium atom in the lattice structure resulted

in two extra holes being formed, so doping with additional tellurium would result in increased hole concentration. This was confirmed via room temperature hall measurements, where the hall carrier concentration increased from $2.09 \times 10^{19} \text{cm}^{-3}$ for PbTe-SrTe to $750 \times 10^{19} \text{cm}^{-3}$ with the addition of 2 wt% tellurium.

2.1.2. Shadow Mask Printed Tellurides

In 2019, a printed flexible TEG based on a Bi_2Te_3 -polyvinyl alcohol (PVA) composites was fabricated by Pires et al. using a shadow mask.^[55] Bi_2Te_3 was synthesized in a solid-state reaction then ball milled with the subsequent particle size distribution ranging between 10 and 300 μm . Surface oxidation occurred as evidenced by the formation of Bi_2O_3 which after HCl treatment was reduced with a subsequent improved power factor from 1.23 to 2.29 $\mu\text{W m}^{-1} \text{K}^{-2}$. The inorganic material was then mixed with PVA to give different wt% ratios. Thick films were printed by drop casting the ink onto a mask. The 75 wt% Bi_2Te_3 to PVA with HCl post-treatment was best performing, exhibiting a negative Seebeck coefficient of -158 $\mu\text{V K}^{-1}$, an electrical conductivity of 0.00172 S cm^{-1} and a power factor of 0.04 $\mu\text{W m}^{-1} \text{K}^{-2}$. The n-type composite had a relatively low curing temperature of 353 K for 2 hours. A 10 leg TEG module comprising of legs (0.2 cm \times 2.5 cm) was printed via the same technique, with silver paint used as the connecting electrode. The power was shown to increase at higher ΔT . A maximum power for the device of 9 $\mu\text{W cm}^{-2}$ was observed at a ΔT of 46 K.

2.1.3. Dispenser Printed Tellurides

Dispenser printing is another method that has been employed for telluride based printed thermoelectrics. Thermoelectric properties of dispenser printed tellurides reported in the literature are represented in **Figure 6** (also Table S2 in the Supporting Information), while examples of dispenser printed thermoelectric modules are highlighted in **Figure 7**.

Chen et al. first reported dispenser printed thermoelectric tellurides in 2009.^[56] N-type Bi_2Te_3 and p-type $\text{Bi}_2\text{Sb}_{1.5}\text{Te}_3$ were used mixed with epoxy. The electrical conductivity, thermal conductivity, Seebeck coefficient, and power factor of the materials at 300 K were 8 and 14.4 S cm^{-1} , 0.48 and 0.52 $\text{W m}^{-1} \text{K}^{-1}$, -159 and 272 $\mu\text{V K}^{-1}$, and 20 and 107 $\mu\text{W m}^{-1} \text{K}^{-2}$, for the n-type and p-type materials, respectively. ZT values at room temperature of 0.0126 and 0.0615 for n-type and p-type respectively, were achieved. The electrical conductivity values obtained are also far smaller than ones found in their respective bulk counterparts, due in part to the insulating properties of the epoxy binder. The insulating nature of the epoxy, however, also gives rise to a reduced thermal conductivity.

Chen et al. reported further work on dispenser printed thermoelectrics in 2010.^[57] n-type Bi_2Te_3 and p-type Sb_2Te_3 were used in conjunction with epoxy. The Seebeck coefficient of the p-type Sb_2Te_3 after curing at 473 K was reported to have a peak of $\approx 173 \mu\text{V K}^{-1}$ when measured across a temperature range of 293 to 343 K, which is higher than the bulk material made by SPS. When the p-type material was cured at 623 K the particles would sinter and show necking, the sample would show an

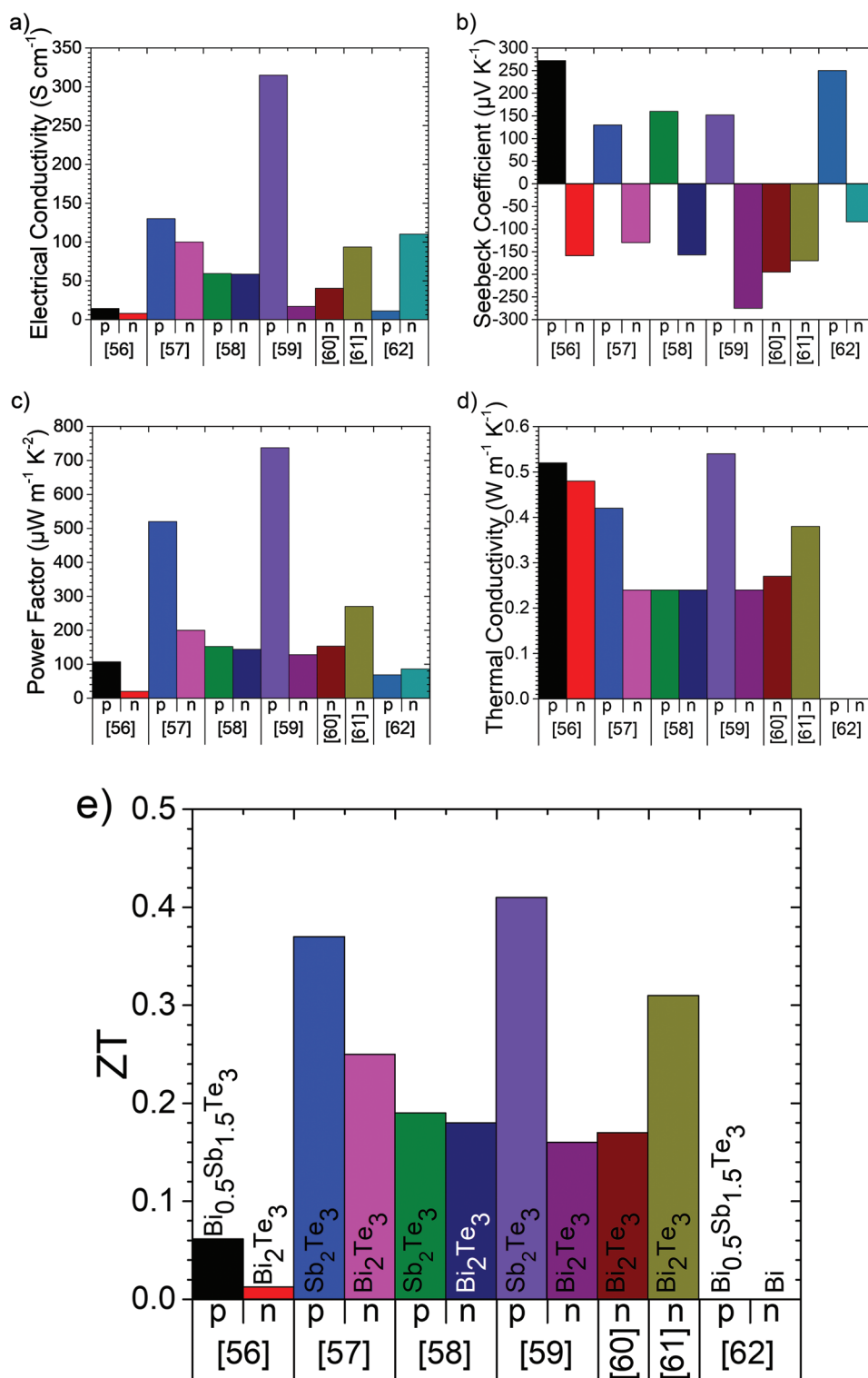


Figure 6. Thermoelectric properties of dispenser-printed tellurides (materials are labeled in part e). Values presented represent the sample and temperature where the peak ZT value was observed, if ZT was not reported then values represent the peak power factor measured: a) electrical conductivity, b) Seebeck coefficient, c) power factor, d) thermal conductivity and e) ZT. This data is also represented in Table S2 (Supporting Information).

increase in electrical conductivity by an order of a magnitude but a decrease of Seebeck coefficient to $120\ \mu V\ K^{-1}$. Despite this trade-off, however, the power factor for a sintered material was

higher. Due to the increased electrical properties and power factor for the sintered sample, a ZT of 0.37 was measured for the sintered sample. The Seebeck coefficient of Bi_2Te_3

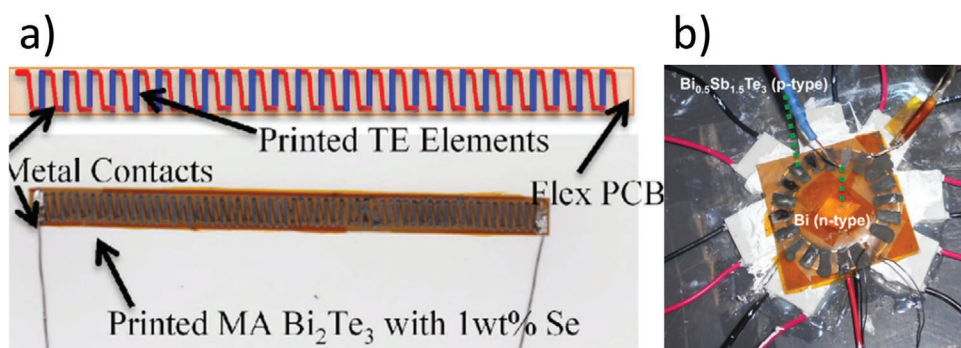


Figure 7. Dispenser printed thermoelectric modules. a) schematic illustration and photo of dispenser printed 62-element mechanically alloyed Bi_2Te_3 with 1 wt% Se planar thermoelectric device on a flexible polyimide-based PCB substrate. Reproduced with permission.^[61] Copyright 2012, ACS. b) Dispenser printed $\text{Bi}_{0.5}\text{Sb}_{1.5}\text{Te}_3/\text{Bi}$ circular thermoelectric device on top of a custom build measurement setup. Reproduced with permission.^[62] Copyright 2014, AIP.

had a peak of $\approx 180 \mu\text{V K}^{-1}$ when measured across the same temperature range (293 to 343 K). There were no appreciable improvements in thermoelectric properties whether the sample was cured at 473 or 623 K, but sintering was not possible for this sample as the temperature needed would exceed the degradation temperature of the binder. The Seebeck coefficient for the n-type material approached bulk values but the electrical conductivity was two orders of magnitude lower than bulk. The ZT value obtained for the n-type material was 0.25, this sample was cured at 473 K. These ZT values were a major improvement over previous work. The thermal conductivities for the p-type and n-type were 0.42 and $0.25 \text{ W m}^{-1} \text{ K}^{-1}$, respectively. Chen et al. also noted the ZT value of 0.15 for a non-sintered sample of the p-type material, the lower ZT was due to the lower electrical conductivity. TEGs were also produced in this body of work, made up of a 10-couple prototype with $5 \text{ mm} \times 500 \mu\text{m} \times 120 \mu\text{m}$ dimensions. The device produced a power output of $0.85 \mu\text{W}$ with 34.4 mV being produced with ΔT of 20 K. This value is larger than screen printed devices made around a similar time.^[47] Chen et al. noted the primary losses within the TEG came from device resistance, which was due to the contact resistance between the thermoelectric legs and the electrical contacts that bridge the legs together.

A year later in 2011, Chen et al. continued work on dispenser printed thermoelectrics.^[58] The same materials were used as before in conjunction with epoxy (n-type Bi_2Te_3 and p-type Sb_2Te_3). The films had thicknesses ranging from 100 to 200 μm . The ZT values at 302 K were 0.18 and 0.19 for the n-type and p-type respectively. The thermal conductivity for both n-type and p-type was $0.24 \text{ W m}^{-1} \text{ K}^{-1}$. The Seebeck coefficient for n-type and p-type was -157 and $160 \mu\text{V K}^{-1}$ with both samples cured at 523 K. While the ZT values (0.18 and 0.19 for n- and p-type respectively) are lower than that of their previous work,^[57] there were some key advancements in terms of TEGs production and performance. A 50 couple TEG device with dimensions $5 \text{ mm} \times 640 \mu\text{m} \times 90 \mu\text{m}$ was printed on polyimide. The device produced a power output of $10.5 \mu\text{W}$ (power density of $75 \mu\text{W cm}^{-2}$) at a ΔT of 20 K, with a current of $61.3 \mu\text{A}$ and a voltage of 171.6 mV . Chen et al. again noted the primary losses were from device resistance as explained in their previous work.

Also in 2011, Madan et al. worked on dispenser printed thermoelectrics.^[59] Here, the effect of different curing times and

temperatures were investigated. The n-type material was Bi_2Te_3 and Sb_2Te_3 the p-type. These materials were combined with an epoxy system consisting of diglycidyl ether of bisphenol F epoxy resin, EPON 862 (Hexion Specialty Chemicals, Inc) and methylhexahydrophthalic anhydride MHHPA (Dixie Chemicals, Inc) as the hardener. These were then dispenser printed on a glass substrate with printed film thicknesses ranging from 100 to 200 μm . Films were then subsequently cured at temperatures ranging from 423 to 623 K, for times ranging from 6 to 48 h. The curing temperature did not seem to alter the electrical conductivity of the n-type material significantly, but in the p-type material increasing curing temperatures increased the electrical conductivity by orders of magnitude. This is because at low curing temperatures charge carriers were limited by boundary scattering, but larger temperatures meant that sintering would take place. This effect was not present in the n-type material, as no sintering took place. The Seebeck coefficient for the p-type material decreased after curing at 473 K. For n-type materials, the absolute Seebeck coefficient would increase significantly with increasing curing temperature. Madan et al. stated that n-type defects are likely created by mechanical deformation, during powder formation, providing excess n-type carriers. These defects increase with curing temperature. The power factor for the n-type material increased as the curing temperature increased from 423 to 473 K, and after that temperature remained unchanged. The power factor within the p-type material increased with increasing temperature, due to the increased electrical conductivity. Increasing annealing time also increased electrical conductivity in the p-type material, due to grain growth, but no effect was observed in the n-type material. Increasing annealing time influenced Seebeck coefficient for the p-type material which matched increasing temperature previously explained. The absolute Seebeck coefficient for n-type material also increased with increasing annealing time. The power factor of the n-type and p-type films increased slightly with increasing curing time (6 to 12 h) but remained unchanged after. The peak characteristics were as follows for the n-type material: $\sigma = 24 \text{ S cm}^{-1}$ when cured at 473 K for 12 h, $S = -287 \mu\text{V K}^{-1}$ when cured at 623 K for 36 h, power factor = $150 \mu\text{W m}^{-1} \text{ K}^{-2}$. Thermal conductivity ($0.24 \text{ W m}^{-1} \text{ K}^{-1}$) was lower than the bulk material due to the insulating property of the epoxy. A maximum ZT of 0.16 was achieved (cured at

623 K for 12 h). Peak characteristics for the p-type material were as follows: $\sigma = 520 \text{ S cm}^{-1}$ when cured at 623 K for 36 h, $S = 174 \text{ } \mu\text{V K}^{-1}$ when cured at 473 K for 12 h, peak power factor = $840 \text{ } \mu\text{W m}^{-1} \text{ K}^{-2}$. Thermal conductivity ($0.54 \text{ W m}^{-1} \text{ K}^{-1}$) was lower than bulk material due to the insulating property of the epoxy. A maximum ZT of 0.41 was achieved (cured at 623 K for 12 h).

In 2012, Madan et al. continued their work on dispenser printing.^[60] In this work n-type Bi_2Te_3 and Bi_2Te_3 with 2 wt% Se were investigated along with the possibility of dispenser printing a single element type TEG. When 2% Se was added there was an increase to both electrical conductivity and Seebeck coefficient. The Seebeck coefficient was reported to be highest at $-200 \text{ } \mu\text{V K}^{-1}$ (at 293 K) and the electrical conductivity had a peak of approximately 475 S cm^{-1} (at 373 K). The sample showed a low thermal conductivity of $0.27 \text{ W m}^{-1} \text{ K}^{-1}$ due to the insulation properties of the polymer binder. The highest power factor was approximately $1500 \text{ } \mu\text{W m}^{-1} \text{ K}^{-2}$. A ZT value of 0.17 (at 300 K) was achieved in this body of work. The single element TEG generated $1.6 \text{ } \mu\text{W}$ at 40 mV and 40 μA with a ΔT of 20 K. The device had a power density of $25 \text{ } \mu\text{W cm}^{-2}$. Although these power values are lower than the previous work, this is for a single element TEG, whereas the previous work was for a thermocouple TEG. The authors noted primary losses again are due to device resistance.

Madan et al. enhanced their previous work the same year, again using dispenser printing.^[61] Bi_2Te_3 with 1 wt% Se was used as an n-type material and used to make a single element TEG. It was found that if the sample was cured after printing at 523 K, a ZT of 0.15 and a thermal conductivity value of $0.26 \text{ W m}^{-1} \text{ K}^{-1}$ was attainable. If the samples were cured at 623 K, however, then the ZT increased to 0.31 despite the thermal conductivity increasing to $0.38 \text{ W m}^{-1} \text{ K}^{-1}$. In both cases, the curing time was 12 h. The Seebeck coefficient was $\approx 170 \text{ } \mu\text{V K}^{-1}$. The electrical conductivity had a peak of 140 S cm^{-1} , which occurred when the sample was cured at 623 K. This electrical conductivity value, while lower than the bulk values due to the insulating properties of the polymer binder, is higher than most other printed thermoelectric samples. Due to the relatively high electrical conductivity within the film, the power factor was measured to be $470 \text{ } \mu\text{W m}^{-1} \text{ K}^{-2}$. A 62 single leg type TEG was also printed (Figure 7a), with dimensions $5 \text{ mm} \times 700 \text{ } \mu\text{m} \times 120 \text{ } \mu\text{m}$. The device produced a power output of $25 \text{ } \mu\text{W}$ at 0.23 mA and 109 mV at a ΔT of 20 K. This device had a power density of $130 \text{ } \mu\text{W cm}^{-2}$. This represents a big improvement from the previous work done by Madan et al. regarding ZT values and single element TEGs.^[60]

Madan et al. also explored the possibility of using Bi on its own as a thermoelectric material, in conjunction with a telluride compound as a p-type material.^[62] Bi was used as an n-type material, as it has decent electrical conductivity and is cheaper and less toxic than its telluride counterparts. The p-type material was $\text{Bi}_{0.5}\text{Sb}_{1.5}\text{Te}_3$ with 8 wt% extra Te. Both materials were combined with an unspecified epoxy. These were dispenser printed on glass and had an unspecified thickness. The electrical conductivity for both n- and p-type was lower than their bulk counterparts due to the insulating properties of the epoxy. The electrical conductivity values of the n-type and p-type films were 110 and 11 S cm^{-1} respectively. The absolute

Seebeck coefficient for Bi was the same as the bulk material ($84 \text{ } \mu\text{V K}^{-1}$), while for the p-type material, it was positive and was also similar to the bulk material ($250 \text{ } \mu\text{V K}^{-1}$). Power factor was the same for both the n- and p-type material, at $86 \text{ } \mu\text{W m}^{-1} \text{ K}^{-2}$. The thermal conductivity was not stated, thus neither was ZT . A prototype TEG was made (Figure 7b), which consisted of a 10-couple dispenser printed circular device printed on a custom made flexible PCB board (nickel and gold plated copper traces on polyimide). The device resistance was measured to be $100 \text{ } \Omega$ when cured at 523 K. An open-circuit voltage of 230 mV at a ΔT of 70 K was measured. A maximum power output of $130 \text{ } \mu\text{W}$ at a ΔT of 70 K was achieved and the device had a power density of $1230 \text{ } \mu\text{W cm}^{-2}$ at a ΔT of 70 K.

2.1.4. Inkjet Printed Tellurides

Tellurides and their related compounds have also been inkjet printed. The products that are produced this way are typically much smaller in thickness compared to screen and dispenser printing. Thermoelectric properties of inkjet printed tellurides reported in the literature are represented in **Figure 8** (also Table S3, Supporting Information) along with examples of inkjet printed thermoelectric modules.

Lu et al. used this method in their investigation in 2014 where $\text{Bi}_2\text{Te}_{2.7}\text{Se}_{0.3}$ and $\text{Sb}_{1.5}\text{Bi}_{0.5}\text{Te}_3$ were used as n-type and p-type, respectively.^[63] The thickness was not precisely stated but instead was given as “150 layers.” The ZT value was also not stated as the thermal conductivity was not measured in this case. The electrical conductivity, Seebeck coefficient and power factor for n-type and p-type were reported to be 60 and 20 S cm^{-1} , -139 and $177 \text{ } \mu\text{V K}^{-1}$ and 183 and $77 \text{ } \mu\text{W m}^{-1} \text{ K}^{-2}$, respectively. Lu et al. also printed both p- and n-type Bi_2Te_3 to print a complete TEG (Figure 8f,g). A single p–n leg produced 0.000341 W of power.

Chen et al. inkjet printed single-crystalline n-type Bi_2Te_3 , to produce phase pure thermoelectric nanowires in 2017.^[29] The thickness of these was reliant on the amount of printer passes or layers, that is, how many times the ink is deposited onto a certain area on the substrate. The thicknesses ranged from 25 passes ($0.4 \text{ } \mu\text{m}$) to 100 passes ($1.6 \text{ } \mu\text{m}$). These samples were then annealed in either a nitrogen or forming gas atmosphere. They concluded that a Seebeck coefficient of up to $-140 \text{ } \mu\text{V K}^{-1}$ is possible, with 100 passes and subsequently being nitrogen annealed. A power factor of $163 \text{ } \mu\text{W m}^{-1} \text{ K}^{-2}$ was also achieved, with 50 passes and forming gas annealing. They stated a ZT value of 0.26, due to a low thermal conductivity of $0.19 \text{ W m}^{-1} \text{ K}^{-1}$ from phonon scattering due to the presence of nanowires.

A year later Chen et al. investigated directly how thickness affects thermoelectric performance in the inkjet printing process.^[64] Bi_2Te_3 and $\text{Bi}_{0.5}\text{Sb}_{1.5}\text{Te}_3$ were used as n-type and p-type, respectively. The n-type material thickness ranged from 50 to 150 passes, whereas the p-type material thickness ranged from 25 to 100 passes. Each set number of passes corresponded to thicknesses of $0.57 (\pm 0.10) \text{ } \mu\text{m}$, $0.89 (\pm 0.06) \text{ } \mu\text{m}$, $1.56 (\pm 0.05) \text{ } \mu\text{m}$ for 50, 100, and 150 passes of Bi_2Te_3 . In the case of the $\text{Bi}_{0.5}\text{Sb}_{1.5}\text{Te}_3$ the thickness was $0.37 (\pm 0.04) \text{ } \mu\text{m}$, $0.62 (\pm 0.08) \text{ } \mu\text{m}$, and $0.94 (\pm 0.12) \text{ } \mu\text{m}$ for 25, 50, and 100 passes, respectively. In this investigation, the thermal conductivity was only recorded for selected samples, therefore ZT is only reported

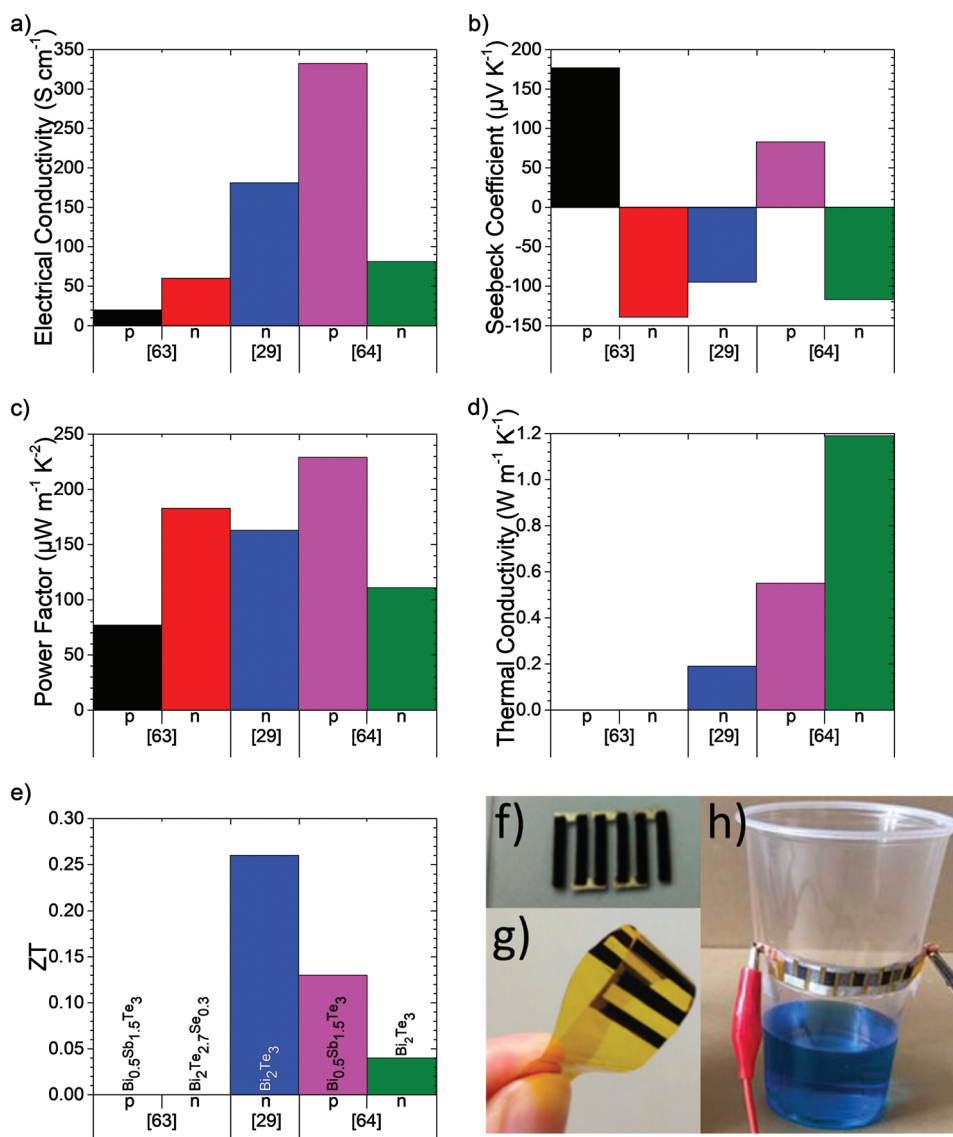


Figure 8. Thermolectric properties of inkjet-printed tellurides (materials are labeled in part e). Values presented represent the sample and temperature where the peak ZT value was observed, if ZT was not reported then values represent the peak power factor measured: a) electrical conductivity, b) Seebeck coefficient, c) power factor, d) thermal conductivity and e) ZT. This data is also represented in Table S3 (Supporting Information). Inkjet-printed telluride thermoelectric modules. f,g) Photos of inkjet-printed Bi₂Te_{2.7}Se_{0.3}/Sb_{1.5}Bi_{0.5}Te₃ modules consisting of 3 pairs of p–n legs on glass and polyimide respectively. Reproduced with permission.^[63] Copyright 2014, Wiley. h) Photograph of inkjet-printed Bi₂Te₃/Bi_{0.5}Sb_{1.5}Te₃ module wrapped around a plastic cup. Reproduced with permission.^[64] Copyright 2019, RSC.

for those samples. The two samples were 100 passes for the n-type Bi₂Te₃ and 50 passes for the p-type Bi_{0.5}Sb_{1.5}Te₃. The ZT values of the n-type and p-type were 0.04 and 0.13, respectively. The electrical conductivity, thermal conductivity, Seebeck coefficient and power factor of the n-type and p-type samples were approximately 81 and 332.5 S cm⁻¹, 1.19 and 0.55 W m⁻¹ K⁻¹, -117 and 83 μV K⁻¹, and 110 and 180 μW m⁻¹ K⁻² respectively. A p–n TEG was also produced, consisting of 5 p–n thermocouples (Figure 8h), generating 127 nW at a ΔT of 32.5 K, which at the time, was the highest reported value for an all printed thermoelectric generator with leg thicknesses under 5 μm. The experiment was simplistic, where the TEG was wrapped around

a plastic cup, deionized water was poured into the cup, and the temperature gradient came from the temperature of the water and the ambient air (cold side). Flexibility tests were also done on the TEG, where the TEG device was tightly wrapped around a rod. Subsequent testing showed no appreciable degradation of properties of the TEG.

2.1.5. Painted Tellurides

In 2016, Park et al. investigated shape-engineerable thermoelectric paint.^[65] This involved synthesizing a paint to be applied

to geometries of any shape. A Bi_2Te_3 based inorganic paint was made, using a Sb_2Te_3 chalcogenidometalate (ChaM) as a sintering aid. This ChaM was made by dissolving Sb and Te in a thiol–diamine mixture. The ChaM was mixed in with glycerol and ethyl glycol containing $\text{Bi}_{2.0}\text{Te}_{2.7}\text{Se}_{0.3}$ (n-type) and $\text{Bi}_{0.4}\text{Sb}_{1.6}\text{Te}_{3.0}$ (p-type) which were both made via ball milling. The room temperature ZT of the paints were noted to be 0.51 and 0.97 for the n- and p-type, respectively. These paints also had reasonable electrical conductivities which ranged from 650 to 750 S cm^{-1} , which originates from the high carrier mobilities of 149 and 141 $\text{cm}^2 \text{V}^{-1} \text{S}^{-1}$ for the n- and p-type, respectively. The Seebeck effect for the n-type hit a peak of $-134 \mu\text{V K}^{-1}$ at 375 K and $170\text{--}190 \mu\text{V K}^{-1}$ for the p-type. These relatively low values for Bi_2Te_3 and Sb_2Te_3 were due to the high carrier concentrations of $3.0 \times 10^{19} \text{ cm}^{-3}$ for the n-type samples and $2.9 \times 10^{19} \text{ cm}^{-3}$ for the p-type samples. The ChaM system also lowered the thermal conductivity of the n- and p-type samples to $0.5\text{--}0.6 \text{ W m}^{-1} \text{ K}^{-1}$ when compared to the bulk value of $1.5\text{--}2.5 \text{ W m}^{-1} \text{ K}^{-1}$ for bulk Bi_2Te_3 systems. A peak ZT of 0.67 and 1.21 was achieved for the n-type and p-type respectively at 373 K. Several devices were made, however, the device with the highest power density was a simple single thermoelectric couple with leg lengths of 5 mm. The device was assembled on an alumina hemisphere substrates and achieved a power output of 4.0 mW cm^{-2} with a ΔT of 50 K.

2.1.6. 3D Printed Tellurides

Recently, 3D printing (mostly using automated printing of viscoelastic colloidal inks from a dispenser) has been found to be a powerful tool in thermoelectrics. The first published 3D printed thermoelectric papers used telluride-based materials. Thermoelectric properties of 3D printed tellurides reported in the literature are represented in **Figure 9** (also Table S4 in the Supporting Information), while examples of 3D printed thermoelectric modules are highlighted in **Figure 10**.

In a progression from the painted work done by Park et al.,^[65] in 2018 Kim et al. used a Bi_2Te_3 based material with all-inorganic colloid inks using Sb_2Te_3 chalcogenidometalate (ChaM) ions as inorganic binders.^[34] These samples were 3D printed in varied geometries (cuboid, disc, and half ring). The p-type and n-type material was $\text{Bi}_{0.4}\text{Sb}_{1.6}\text{Te}_3$ and $\text{Bi}_2\text{Te}_{2.7}\text{Se}_{0.3}$, respectively, achieving a ZT of 0.9 and 0.6, respectively. The dispersion of ChaM particles within the Bi_2Te_3 decreased the void spaces within the sample, by allowing the Bi_2Te_3 to undergo electrostatic interactions, improving viscoelasticity and manufacturability. The amount of ChaM particles present in the ink ranged from 20 to 25 wt%. The large ZT value could be a result of the ChaM particles, as they decrease heat transfer within the sample, making the sample have an inherently lower thermal conductivity. The room temperature electrical conductivity and Seebeck coefficient of the cuboid, disc and half ring were 553.75 S cm^{-1} and $165 \mu\text{V K}^{-1}$, respectively. The temperature dependence performance of the material was characterized using cuboids of width 10 mm and thickness of 1.5–2.0 mm. The electrical conductivity of the p- and n-type materials was measured to be in the range of $500\text{--}550 \text{ S cm}^{-1}$, and decreased with increasing temperature. The Seebeck coefficient of the

p- and n-type materials had peaks of 199 and $145 \mu\text{V K}^{-1}$ respectively, at 448.15 to 473.15 K. The temperature-dependent thermal conductivity of the n- and p-type printed samples was $0.50\text{--}0.63 \text{ W m}^{-1} \text{ K}^{-1}$ over the entire measured temperature range (room temperature to 498 K). 3D Printed thermoelectric half rings were used to create a cylindrical TEG (**Figure 10a**), which was wrapped around an alumina pipe, which had hot water flowing through it. The TEG achieved a maximum output voltage of 270 mV and maximum power of 1.62 mW at $\Delta T = 39 \text{ K}$. The output power density was 1.42 mW cm^{-2} at the same temperature difference. It was noted that the device had a high contact resistance due to the use of Ag epoxy instead of solder.

A follow-up paper by Kim et al. refined the printing process to allow for much finer control over the 3D printing resolution, with dimensions $<200 \mu\text{m}$.^[66] This was achieved by optimizing the particle size, size distribution and surface states of the ink materials, this all allowed for the inorganic thermoelectric inks to have an extremely high viscoelasticity. The p-type ink was $\text{Bi}_{0.55}\text{Sb}_{1.45}\text{Te}_3$ with 25 wt% ChaM content of $\text{Sb}_2\text{Te}_4^{2-}$, while the n-type ink was $\text{Bi}_2\text{Te}_{2.7}\text{Se}_{0.3}$ with 10% of the same ChaM. At 300 K the n-type and p-type had electrical conductivities of ≈ 800 and $\approx 650 \text{ S cm}^{-1}$ respectively, with increasing measurement temperature came drops in the electrical conductivity up to the maximum measurement temperature of 500 K where electrical conductivities of the n- and p-type were ≈ 350 and 300 S cm^{-1} respectively. This drop in electrical conductivity with temperature is typical for metallic-like behavior. Seebeck coefficients are largely consistent through the measurement temperature range, with the p- and n-types exhibiting ≈ 200 and $\approx 120 \mu\text{V K}^{-1}$ respectively. Similarly, the thermal conductivities of both types do not change much with the measurement temperatures (300–525 K) and are $\approx 0.8 \text{ W m}^{-1} \text{ K}^{-1}$, with the exception that between 400 and 525 K the p-type thermal conductivity steadily increases to $\approx 1.2 \text{ W m}^{-1} \text{ K}^{-1}$. This leads to the p-type having a peak $ZT \approx 1$ at 350 K and the n-type having a peak ZT of ≈ 0.5 at 425 K. The intricate printing allowed for μTEGs (**Figure 10b**) to be produced, which yielded a maximum output voltage of 42.4 mV and a power of $2.8 \mu\text{W}$ at a ΔT of 82.9 K. Due to the μ nature of the devices, the power density is $479.0 \mu\text{W cm}^{-2}$.

The same research group in 2021 took the same colloidal 3D printing approach but applied the technique to PbTe .^[67] In this work, however, Na doping of PbTe (substituting Pb for Na) thermoelectric particles is used to achieve negative surface charges for the colloids. This is in contrast to the use of $\text{Sb}_2\text{Te}_3/\text{Sb}_2\text{Te}_4^{2-}$ in their previous work. The Na doping of PbTe lead to p-type printed samples. To make n-type, Sb was used instead of Na. This achieved positive surface charges which allowed for the formation of colloids. Various doping levels of Na and Sb (0.5%–2.0% Pb atomic substitution) were tried for the p- and n-type inks respectively. Higher Na content gave higher electrical and thermal conductivities, while yielding lower Seebeck coefficients. This can be understood when looking at the carrier concentration, which increased from 4.78×10^{19} to $1.6 \times 10^{20} \text{ cm}^{-3}$ when increasing Na doping from 0.5% to 2.0%. The best p-type ZT values overall were seen for 2.0% Na, which at 700 K had a ZT of 1.4 ($\sigma = 400 \text{ S cm}^{-1}$, $S = 230 \mu\text{V K}^{-1}$, $\kappa = 0.8 \text{ W m}^{-1} \text{ K}^{-1}$). As is typical for PbTe ,

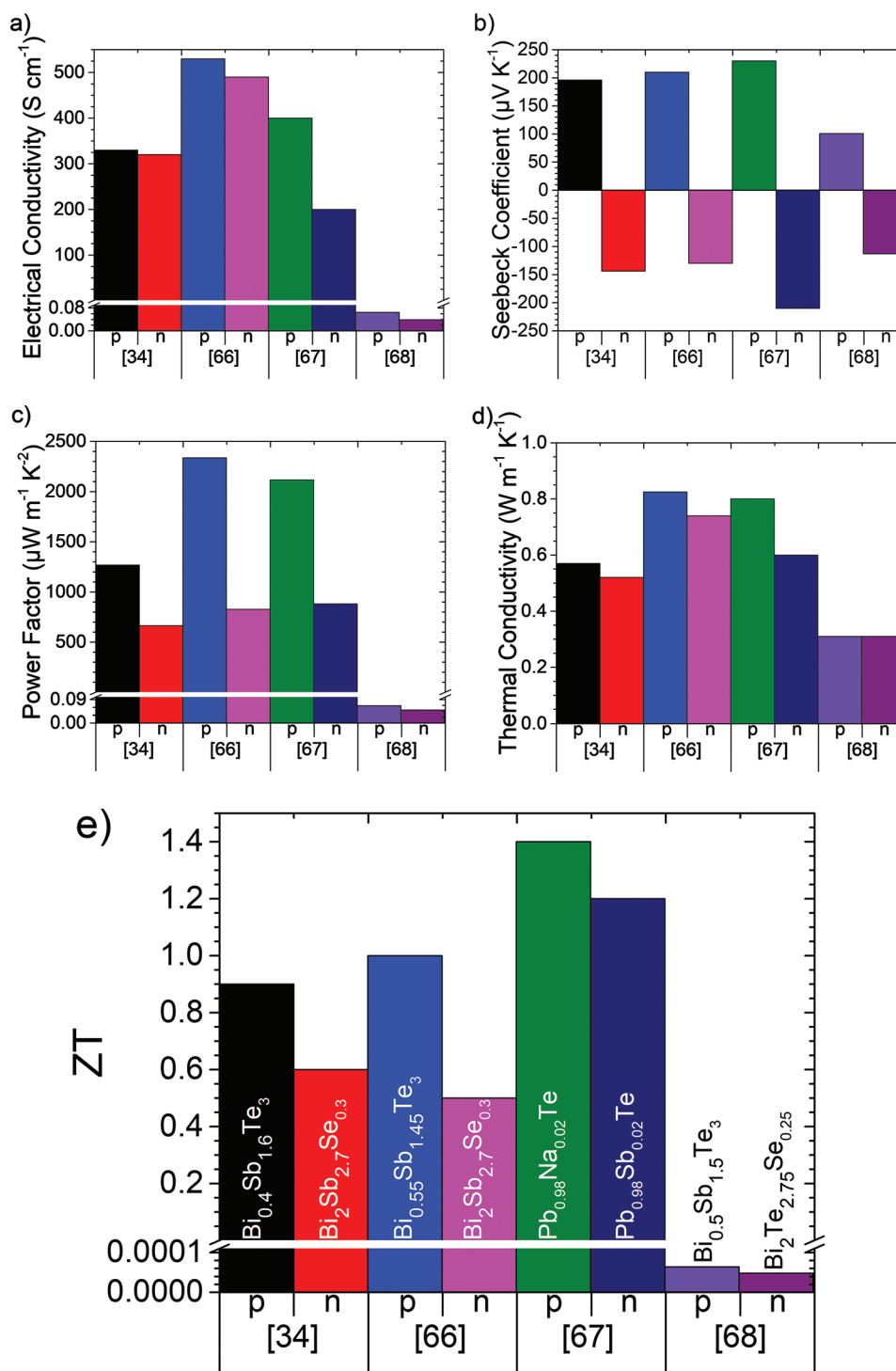


Figure 9. Thermoelectric properties of 3D printed tellurides (materials are labeled in part e). Values presented represent the sample and temperature where the peak ZT value was observed: a) Electrical conductivity, b) Seebeck coefficient, c) power factor, d) thermal conductivity and e) ZT. This data is also represented in Table S4 (Supporting Information).

conductivities (σ and κ) were higher towards room temperature, while Seebeck values are higher toward the maximum measurement temperature of 800 K. There was a less clear trend seen with varying Sb doping concentrations, although

again 2.0% doping was seen to give the highest ZT of 1.2 at 750 K ($\sigma = 200 \text{ S cm}^{-1}$, $S = -210 \text{ } \mu\text{V K}^{-1}$, $\kappa = 0.6 \text{ W m}^{-1} \text{ K}^{-1}$). The same thermolectric property trends with temperature are also seen. A new tubular thermolectric architecture is presented

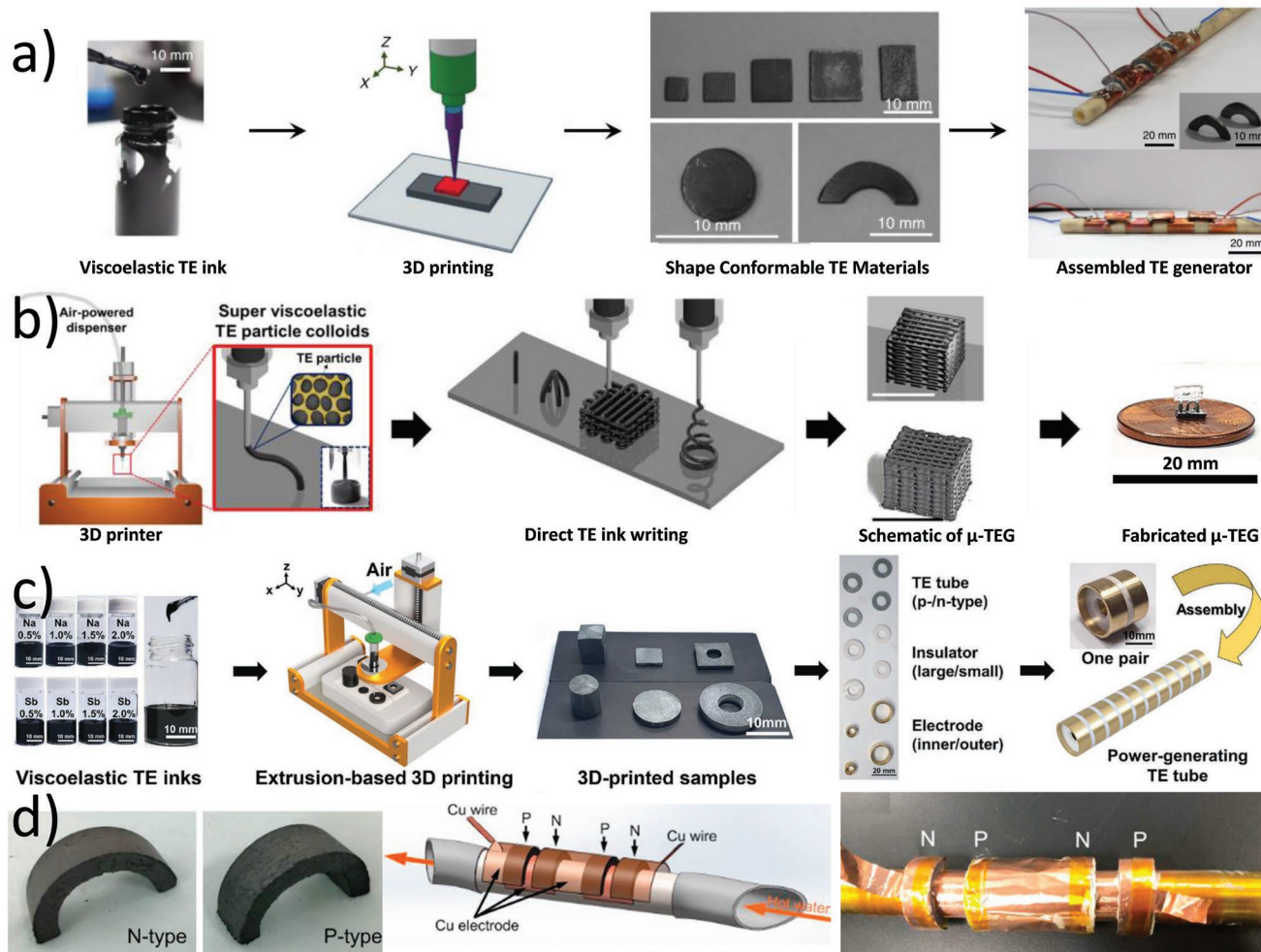


Figure 10. 3D-printed telluride thermoelectric modules. a) 3D printing of a $\text{Bi}_{0.4}\text{Sb}_{1.6}\text{Te}_3/\text{Bi}_2\text{Sb}_{2.7}\text{Se}_{0.3}$ module, from left to right: photograph showing viscoelastic telluride-based TE ink, illustration of 3D printing process, photographs of 3D-printed TE materials, and photographs of fabricated half-ring-based conformal TEG with an inset of the n- and p-type 3D printed half rings. Reproduced with permission.^[34] Copyright 2018, Nature. b) 3D printing of a $\text{Bi}_{0.55}\text{Sb}_{1.45}\text{Te}_3/\text{Bi}_2\text{Te}_{2.7}\text{Se}_{0.3}$ μ module with dimensions $<200 \mu\text{m}$, from left to right: schematic illustration of printer setup, illustration of direct ink writing for 3D TE architectures, illustrative models of the printed μTEGs , photograph of fabricated μTEG . Reproduced with permission.^[66] Copyright 2021, Nature. c) 3D printing of a $\text{Pb}_{1-x}\text{Na}_x\text{Te}/\text{Pb}_{1-x}\text{Sb}_x\text{Te}$ thermoelectric module, from left to right: Na and Sb doping-induced viscoelastic TE PbTe inks, schematic illustration showing the sequential 3D printing of $\text{Pb}_{1-x}\text{M}_x\text{Te}$ TE inks, photograph showing the 3D-printed PbTe structure with various shapes, photograph of the components for module assembly, photograph of the fabricated power-generating TE tube consisting of a unipair of p-type and n-type PbTe legs and schematic model of a power-generating tube consisting of ten pairs of TE legs. Reproduced with permission.^[67] Copyright 2021, Wiley. d) Photograph of dispenser printed and compression molded thermoelectric n- and p-type legs and, schematic and photograph of dispenser printed and compression molded thermoelectric module. Reproduced with permission.^[68] Copyright 2019, Elsevier.

for their printed thermoelectric materials, allowing p- and n-type materials to be easily connected around a pipe. A water-cooled thermoelectric generator was made (Figure 10c) that had a maximum output voltage of 83.2 mV and power output of 216.3 mW at a ΔT of 300 K. The device had a power density of 153.7 mW cm^{-2} . A passive cooled device managed to produce $\approx 140 \text{ mW}$, with the drop in power output being caused by the lower achievable maximum ΔT of 250 K.

In 2019, Wang et al. fabricated a TEG device to extract heat from a hot water pipe (Figure 10d). Dispenser printing was used where the pressure was supplied by a screw.^[68] In this work the n-type material was $\text{Bi}_2\text{Te}_{2.75}\text{Se}_{0.25}$ and the p-type material was $\text{Bi}_{0.5}\text{Sb}_{1.5}\text{Te}_3$ and both materials were combined

with polylactic acid (PLA). These materials were printed in a half-ring shape, and subsequently compressed. The rings had widths of 12 mm, thickness of 4.4 mm and an internal diameter of 20 mm. A TEG of two thermocouples was assembled with Cu foils ($20 \mu\text{m}$) acting as the electrodes. This TEG was then fitted on a stainless steel pipe that was 20 mm in diameter, and hot water was flowed through the pipe and natural air cooling was used at the cold side. The TEG had an output voltage of 3.4 mV and an output power of 126 nW with a ΔT of 10.5 K. The individual thermoelectric properties of the n-type material were measured and were recorded to be 0.039 S cm^{-1} , $-113 \mu\text{V K}^{-1}$, and $0.31 \text{ W m}^{-1} \text{ K}^{-1}$ for electrical conductivity, Seebeck coefficient and thermal conductivity, respectively. The individual

thermoelectric properties of the p-type material were as follows, 0.065 S cm^{-1} , $101 \mu\text{V K}^{-1}$ and $0.31 \text{ W m}^{-1} \text{ K}^{-1}$ for electrical conductivity, Seebeck coefficient and thermal conductivity, respectively. Theoretical experiments were also done to maximize efficiency. It was found that the larger the heat sink area was, the higher the ΔT was, and device thickness had a large effect on thermoelectric performance.

2.1.7. Laser Printed Tellurides

Another method of printing that is worth briefly mentioning is laser printing, with thermoelectric properties, materials and a device illustrated in **Figure 11** (thermoelectric properties are also shown in Table S5, Supporting Information). Laser printing is less popular for thermoelectric materials manufacturing than other printing techniques, due to the low thermal conductivity of thermoelectric materials hindering the laser's ability to melt the powder of the thermoelectric material. Nevertheless, lasers have been reported as being used for printing of thermoelectric materials in a few manuscripts. In 2013 laser-induced forward transfer (LIFT) fabrication was used to make a TEG (Figure 11f,g) by Feinaeugle et al.^[69] In this body of work two n-type materials were used, Bi_2Te_3 and Bi_2Se_3 ; along with a p-type material, $\text{Bi}_{0.5}\text{Sb}_{1.5}\text{Te}_3$. The approximate electrical conductivity values were 0.25, 3.33, and 16.67 S cm^{-1} for the Bi_2Se_3 , Bi_2Te_3 and $\text{Bi}_{0.5}\text{Sb}_{1.5}\text{Te}_3$, respectively. The Seebeck coefficients of the materials were -93 ± 8 , -49 ± 3 and $142 \pm 7 \mu\text{V K}^{-1}$ for the Bi_2Se_3 , Bi_2Te_3 and $\text{Bi}_{0.5}\text{Sb}_{1.5}\text{Te}_3$, respectively. The approximate power factor for each material was 0.22, 0.80 and $34 \mu\text{W m}^{-1} \text{ K}^{-2}$. A TEG device was also made in this body of work, which achieved a generator Seebeck coefficient of 0.17 mV K^{-1} per thermocouple and a resistance of $10 \text{ K}\Omega$, a power output was not stated.

In 2019 a telluride based material with a large ZT value for printed materials was made by Shi et al.^[70] In this body of work 100 mesh p-type $\text{Bi}_{0.5}\text{Sb}_{1.5}\text{Te}_3$ was 3D printed (Figure 11h) using selective laser sintering (SLS). A ZT of 1.29 at 400 K was achieved, which is comparable to that of bulk and nonprinted materials. The electrical conductivity was reported as 403 S cm^{-1} , lower than that of the bulk material stated in this work, which was reported to be a maximum of 736 S cm^{-1} . The Seebeck coefficient was higher than the bulk material, at $190.51 \mu\text{V K}^{-1}$. The thermal conductivity of the sample was measured to be $0.27 \text{ W m}^{-1} \text{ K}^{-1}$ at 327 K, less than 18% of the minimum found in the bulk material.

Qiu et al.^[71] also in 2019, manufactured 3D printed $\text{Bi}_{0.4}\text{Sb}_{1.6}\text{Te}_3$ via selective laser melting (SLM), also known as laser powder bed fusion (LPBF). A ZT of 1.1 at 316 K was achieved in the building direction and 0.65 at 326 K perpendicular to the building direction. To achieve this the samples were annealed at 673 K for 24 h postprinting. In the building direction, the electrical conductivity was highest at room temperature (1200 S cm^{-1}), with the Seebeck coefficient peaking at $\approx 325 \text{ K}$ ($195 \mu\text{V K}^{-1}$) and thermal conductivity reaching a minimum at $\approx 325 \text{ K}$ ($1.1 \text{ W m}^{-1} \text{ K}^{-1}$). The printed samples had a high preferential orientation factor (up to 0.9), which is close to that of zone-melted single crystals. The SLM samples exhibited up to a 195% increase in compressive strength (91 MPa) compared

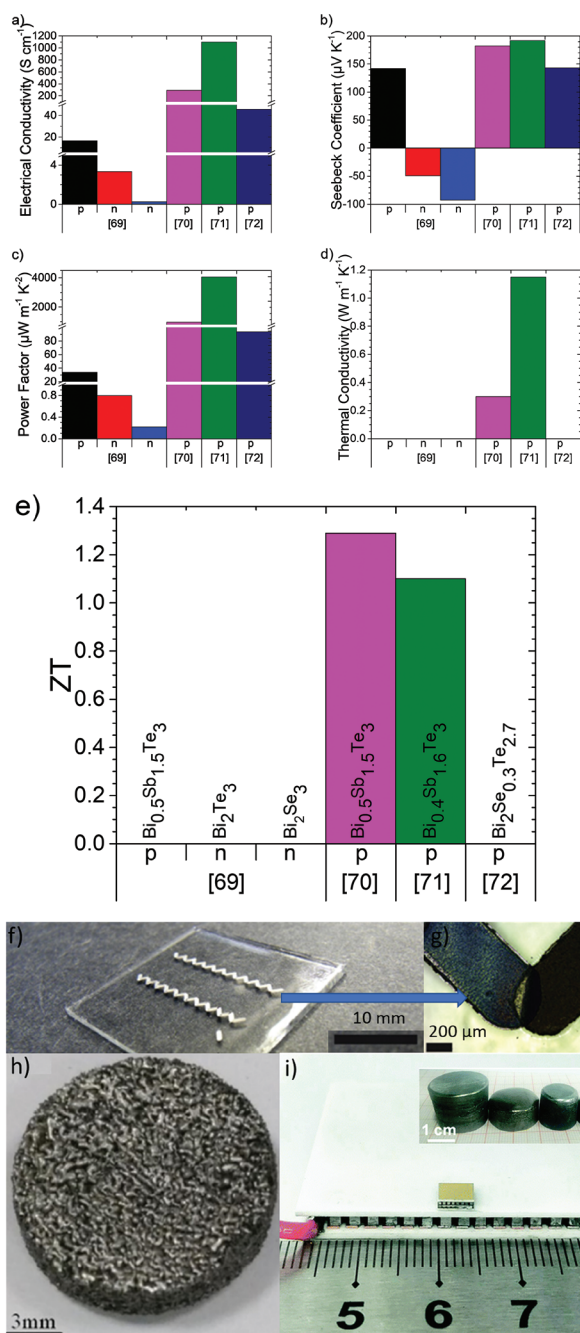


Figure 11. Thermoelectric properties of laser-printed tellurides (materials are labeled in part c). Values presented represent the sample and temperature where the peak ZT value was observed, if ZT was not reported then values represent the peak power factor measured: a) electrical conductivity, b) Seebeck coefficient, c) power factor, d) thermal conductivity and e) ZT . This data is also represented in Table S5 (Supporting Information). Images of laser-printed tellurides: f) photograph of two laser-induced forward transferred $\text{Bi}_2\text{Te}_3/\text{Bi}_{0.5}\text{Sb}_{1.5}\text{Te}_3$ modules each with 10 thermocouples, g) is a magnification of one of the junctions (reproduced with permission.^[69] Copyright 2013, IOP). h) $\text{Bi}_{0.5}\text{Sb}_{1.5}\text{Te}_3$ sample prepared by selective laser sintering 3D printing (reproduced with permission.^[70] Copyright 2019, Elsevier), i) photograph of selective laser melted micro and macro $\text{Bi}_{0.4}\text{Sb}_{1.6}\text{Te}_3$ thermoelectric generators, with zone melted and SPS $\text{Bi}_2\text{Te}_{2.7}\text{Se}_{0.3}$ n-type legs, the insert is of as printed p-type $\text{Bi}_{0.4}\text{Sb}_{1.6}\text{Te}_3$ bulks (reproduced with permission.^[71] Copyright 2019, RSC).

to zone-melted samples. Micro (4 mm × 4 × mm × 1.2 mm, 28 leg pairs) and macro (4 cm × 4 × cm × 4 mm, 127 leg pairs) thermoelectric modules were made (Figure 11i), by using a Bi₂Te_{2.7}Se_{0.3} n-type legs manufactured by zone melting and spark plasma sintering for the macro and micro modules respectively. The power output of the micro module was not measured, but the macro module was seen to generate up to 1.45 W.

In 2021 Welch et al. used selective laser melting (SLM) to manufacture selenium doped bismuth telluride.^[72] The process resulted in highly textured columnar grains orientated in the build direction with nanoscale inclusions and a shift in the primary charge carriers resulting from sparse oxide inclusions and a tellurium segregation. The p-type material was seen to have a peak Seebeck coefficient of 143 μV K⁻¹ at 368 K, while the electrical conductivity was seen to be highest at 488 K (48.2 S cm⁻¹). No other thermoelectric properties were measured, however.

2.1.8. Printed Tellurides Summary

Recent work by Kim et al.,^[34,66] Lee et al.,^[67] Shi et al.,^[70] and Qiu et al.,^[71] all on 3D printed tellurides, yield ZTs around or slightly above 1. While these 3D printing techniques are exciting as they allow devices more akin to commercial ones produced by SPS or hot pressing to be produced, more importantly, they produce similar ZT values to bulk materials prepared by SPS or hot pressing. Thicker samples typically made by 3D printing are also seen to correlate to higher device performance, as revealed in Table 1. These telluride based works highlight the progression that has been made in thermoelectric printing within the last 3 years and indicate a trajectory toward outcompeting traditional thermoelectric manufacturing techniques.

2.2. Selenides

While the current materials of choice in commercial thermoelectric generators are Bi₂Te₃ and PbTe for low and medium temperature applications respectively, in sustainability terms these are problematic due to the low Earth-abundance of Te, which is similar to that of Pt (1 μg kg⁻¹).^[73] While Te is relatively cheap at 78 \$ Kg⁻¹ in 2021 (aluminum is 329 \$ Kg⁻¹),^[74,75] if Te thermoelectric generators were used in scale this cost would almost certainly rise sharply as resources dwindled.

Selenides have recently received more attention as possible printed thermoelectric materials. These materials, much like tellurides can be printed in a variety of ways. An example of a selenide is lead selenide (PbSe). PbSe has an electrical bandgap of ≈0.3 eV and so shows promise as a thermoelectric material. It has decent electrical conductivity and can be doped. In general, however, the thermoelectric performance of PbSe is not as good as PbTe as the electron mobility of PbSe is smaller than that of PbTe, although they do have similar lattice thermal conductivity values.^[76] A ZT value of approximately 1.6 at 923 K was achieved by Zhao et al. in 2013, which at the time was the highest ZT value of a non-telluride chalcogen thermoelectric compound.^[77] PbSe was doped with 2% Na and 3% CdS,

however, this was done using spark plasma sintering, a high energy method. Copper selenides, Cu₂Se is another promising selenide which has the potential to be used in thermoelectrics. This compound undergoes intensified phonon scattering due to the complex structure and has a low thermal conductivity of approximately 0.5 W m⁻¹ K⁻¹ at 1000 K.^[76] Liu et al. achieved a ZT value of 1.5 at 1000 K using Cu₂Se in 2012.^[78] Liu et al. noted that copper ions are highly disordered around the Se sublattice and are superionic with liquid-like mobility, hence the high ZT.

Perhaps the most promising of the selenides is, however, tin selenide (SnSe). SnSe's desirable thermoelectric properties stem from the ultralow thermal conductivity value due to the very low lattice thermal conductivity (κ_L), which is among the lowest for crystalline materials (<0.4 W m⁻¹ K⁻¹ at 923 K).^[9,79] Along the *b*-axis SnSe has a zig-zag structure, along which the ultralow thermal conductivity is observed. The strong anharmonicity in bonding gives rise to the low thermal conductivity. Thanks to these properties, Zhao et al. reported a substantial ZT value of 2.6 (±0.3) at 923 K along the *b*-axis of single crystals of SnSe.^[9] Single crystals of SnSe however are energy expensive to manufacture due to the high temperature and pressure conditions needed.

Polycrystalline SnSe has also been investigated. Sassi et al. produced polycrystalline SnSe in quartz tubes and these were then densified by SPS, this polycrystalline SnSe showed a ZT value of 0.5 at 823 K.^[80] Shi et al. also produced polycrystalline SnSe (self-doped) by solvothermal synthesis followed by SPS, which again produced a large ZT value of 1.36 ± 0.12 at 823 K.^[81] Much like single-crystal SnSe and traditional chalcogenide thermoelectric materials however, these results required expensive, high energy conditions. In 2018, Burton et al.^[82] produced thin films of SnSe using a simple evaporation technique, this reinforced the previous work done on the low thermal conductivity of SnSe, as the samples showed even lower thermal conductivity of 0.08 W m⁻¹ K⁻¹ between 375 and 450 K. This was explained by the propagation pathway that the phonons must travel through on the SnSe nanosheets that had been formed by the thermal evaporation technique. The first reported working SnSe TEG was also manufactured in this study, which produced a power output of 0.09 μW. All these results are also only for the inherently p-type SnSe. The literature and research into doping of SnSe to make it n-type is relatively scarce compared to the p-type material.

Cu₂Se has been shown to be spin coated,^[83] Ag₂Se to be printed,^[84–86] and SnSe to be 3D printed.^[36] Thermoelectric properties of these printed selenides are represented in **Figure 12** (also Table S6, Supporting Information), along with images of the printed materials and schematics of manufacturing techniques. Printed Se thermoelectric generators with a reported power output are summarized in **Table 2**.

2.2.1. Spin Coated Selenides

Lin et al. successfully made a Cu₂Se thermoelectric film by spin coating in 2017.^[83] This device was different to the previous devices mentioned so far in this review as it contains more Earth-abundant elements. The printed materials had a thickness of 55 nm, which is the thinnest device mentioned

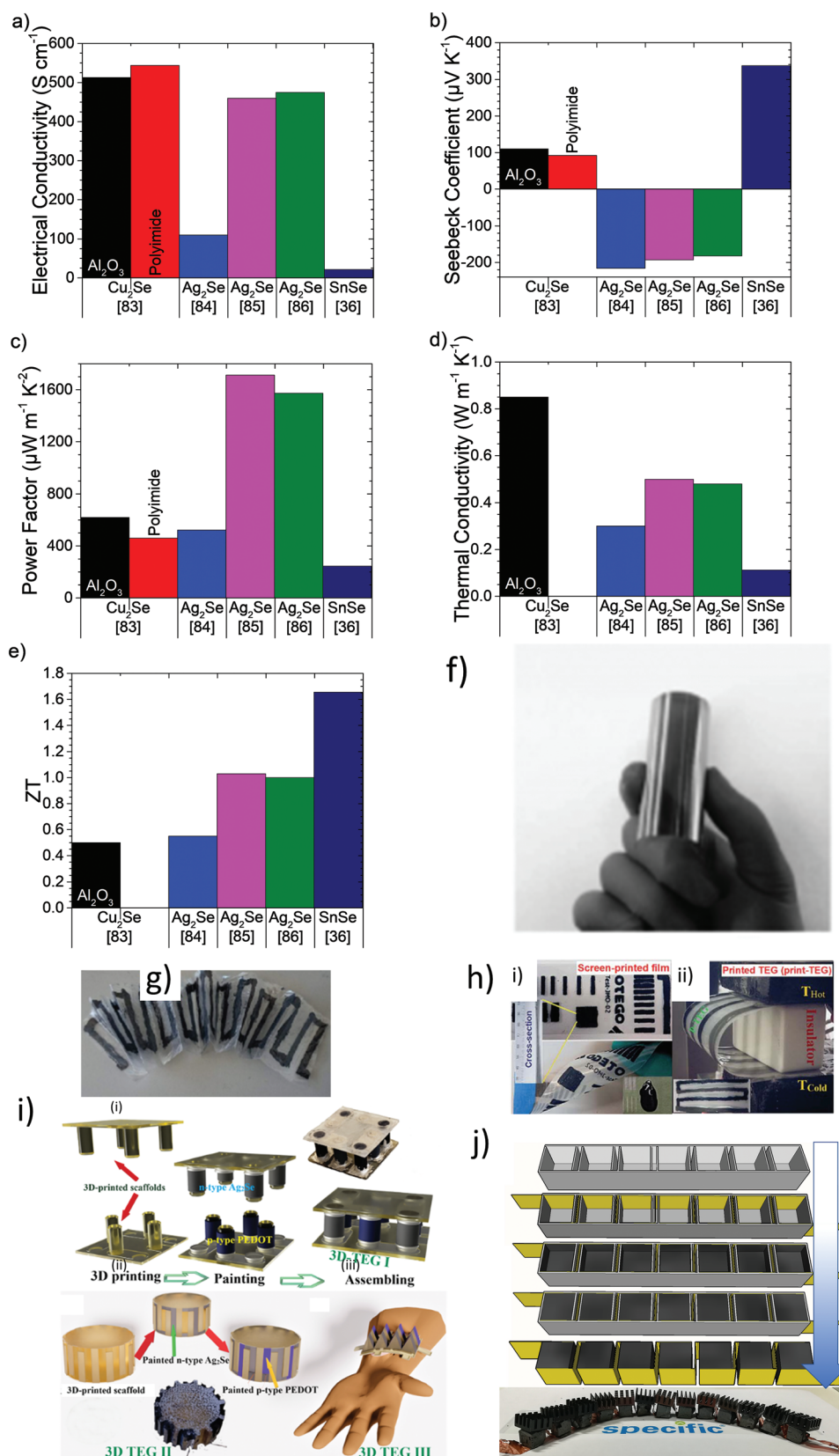


Figure 12. Thermoelectric properties of printed selenides, with material printed displayed below the chart and substrates displayed in the bars. Values presented represent the sample and temperature where the peak ZT value was observed, if ZT was not reported then values represent the peak power factor measured: a) electrical conductivity, b) Seebeck coefficient, c) power factor, d) thermal conductivity and e) ZT. This data is also represented in

Table 2. Summation of Se based printed thermoelectric generators that report power outputs.

Material	Printing technique	Substrate	Thickness [mm]	Power [μW]	Power density [mW cm^{-2}]	Cure time [min]	Cure temperature [K]	Refs.
PEDOT:PSS/ $\text{Ag}_{0.3}$ to $\text{Se}_{0.7}$ wt% with polystyrene	Screen	PET	0.04	83.7	0.321	N/A	N/A	[84]
PEDOT:PSS/ $\text{Ag}_{0.27}$ to $\text{Se}_{0.63}$ wt% with polystyrene	Screen	PET	0.04	0.19	N/A	10	473	[85]
PEDOT:PSS/ Ag_2Se	Painting	High temp resin	N/A	7	N/A	20	473	[86]
SnSe with carboxymethylcellulose	3D	ABS mold	10	20	N/A	10	393	[36]

in the chalcogenide section (thinner than inkjet). The thin film exhibits a power factor of $620 \mu\text{W m}^{-1} \text{K}^{-2}$ at 684 K ($\kappa = 0.85 \text{ W m}^{-1} \text{K}^{-1}$, $ZT = 0.5$) when printed on Al_2O_3 and $460 \mu\text{W m}^{-1} \text{K}^{-2}$ at 664 K when printed on flexible polyimide. These values were higher than other literature values mentioned in the body of work ($<100 \mu\text{W m}^{-1} \text{K}^{-2}$) and according to Lin et al. among the highest for all flexible thermoelectric films to date. A sample (Figure 12f) also showed no degradation after bending cycles (1000 cycles in this case) much like has been shown by screen-printed Bi_2Te_3 previously.^[50]

2.2.2. Printing Silver Selenides

In 2020, Mallick et al. produced Ag–Se based n-type thermoelectric materials.^[84] Here Se powder was mixed with dried Acheson silver DAG 1415M in a solution of polystyrene and toluene. These inks were then printed via doctor blading and screen printing, before being sintered for the formation of Ag_2Se . The wt% of Se in the films was Ag_{1-x} to Se_x where x varies from 0 to 0.80. A Seebeck coefficient of $-216 \mu\text{V K}^{-1}$ was achieved, with an electrical conductivity of 110 S cm^{-1} . A peak power factor of $522 \mu\text{W m}^{-1} \text{K}^{-2}$ was achieved for the film (0.3)Ag–(0.7)Se. A ZT of approximately 0.55 was achieved for an n-type material at room temperature due to a thermal conductivity of $\approx 0.3 \text{ W m}^{-1} \text{K}^{-1}$ being observed. A flexible TEG (Figure 12g) $\text{Ag}_{0.3}$ to $\text{Se}_{0.7}$ wt % was made, and PEDOT:PSS was used as the p-type ink. The TEG consisted of 13 thermocouples and generated an open-circuit voltage of 181.4 mV and a maximum output power density of $321 \mu\text{W cm}^{-2}$ at a ΔT of 110 K. The TEG was also demonstrated by placing on a wrist and made an output voltage of 72.2 mV at ΔT of 30 K.

Mallick et al. employed a one-pot synthesis method for thermoelectrics, in 2020.^[85] Here in this work, a one-pot method was used to make a Ag_2Se based material as an n-type material. Ag and Se powders were mixed with 2 wt% BYK additive in a polystyrene–toluene solution, followed by mixing for 72 h at 1200 rpm. The ink was then doctor bladed and screen printed to produce thin films. Different samples were made with

varying wt% of Se Ag_{1-x} to Se_x where x varied from 0.1 to 0.6. The orthorhombic $\beta\text{-Ag}_2\text{Se}$ is formed after printing by thermally annealing at a moderate temperature, due to the dissociative adsorption of volatilized Se by Ag particles which allows a high conductivity transport path. A ZT value of over 1 was achieved, while an average ZT of 0.94 was attained at room temperature. The film with $x = 0.40$ was found to have the highest Seebeck coefficient of $-210 \mu\text{V K}^{-1}$. The electrical conductivity ranged from 500 to 100 S cm^{-1} . A power factor of $\geq 1000 \mu\text{W m}^{-1} \text{K}^{-2}$ was observed for films where x was between 0.20 and 0.40. It was also found that thermal conductivity ranged from 0.31 to $0.50 \text{ W m}^{-1} \text{K}^{-1}$. A device was also made (Figure 12h) via printing where a generator consisting of two thermocouples yielded a output voltage of 17.6 mV with a high maximum power output of $0.19 \mu\text{W}$ for ΔT of 60 K. In this device, the p-type material was commercially available PEDOT:PSS.

More recently, a 2021 paper by Mallick et al. have also investigated new ways of incorporating 3D printing into the production of thermoelectric devices.^[86] Mallick et al. first 3D printed three “scaffold” structures, each with different shapes and painted these scaffolds with commercially bought p-type PEDOT and their own formulated Ag_2Se as the n-type material (Figure 12i). The n-type Ag_2Se was again made using a one-pot method where silver and selenium were mixed with polystyrene and N-methyl-2-pyrrolidone, followed by an addition of ≈ 2 wt% BYK 430 additive. This mixture was left to stir for 72 h at 1000 rpm at room temperature. For characterization purposes, thin films were made of the p-type and n-type inks, and the Seebeck coefficient was found to be ≈ -183 and $9.2 \mu\text{V K}^{-1}$ for n-type and p-type, respectively. The electrical conductivities were ≈ 472 and 600 S cm^{-1} for n-type and p-type, respectively, at room temperature. The κ value for both inks was also found to be in the range of 0.5 and $0.7 \text{ W m}^{-1} \text{K}^{-1}$. The ZT values for the n-type Ag_2Se ink was found to be ≈ 1 at room temperature and 10^{-2} for the p-type PEDOT.

A high-temperature resin was used to 3D print the scaffolds, and the inks were then painted onto these structures, and connected electrically in series and thermally in parallel. These painted scaffold TEGs were then sintered at 473 K for 20 min

Table S6 (Supporting Information). Images of the printed materials and schematics of manufacturing techniques: f) photograph of spin-coated Cu_2Se thin film on polyimide (reproduced with permission.^[83] Copyright 2017, Wiley). g) Photograph of PEDOT:PSS with screen printed $\text{Ag}_{0.3}$ to $\text{Se}_{0.7}$ wt% with polystyrene thermoelectric generator (reproduced with permission,^[84] Copyright 2020, ACS). h) Photographs of screen printed Ag_2Se films. i) various screen printed patterns with cross-section image taken using an optical microscope in the inset (ii) the printed-TEG of two thermo-couples during operation (Reproduced with permission.^[85] Copyright 2020, RSC) i) schematic diagrams of the 3D-TEG fabrication process of Ag_2Se thermoelectric modules for 3 different designs (reproduced with permission.^[86] Copyright 2021, ACS), j) schematic diagram of the fabrication process of a printed SnSe and a photograph of a working device (Reproduced under the terms of an Attribution 4.0 International [CC BY 4.0] license.^[36] Copyright 2019, The Authors. Published by Wiley).

to allow the formation of β -Ag₂Se in the n-type legs. These scaffold structured TEGs were then tested for performance with temperature differences of 10–70 K. The dimensions of the first TEG were 3 cm × 3 cm × 1.2 cm, and it produced ≈0.4 μW. The second TEG had 9 pairs of thermocouples and had a cylindrical gear like shape to it, the diameter and the height of the second TEG were 2 and 1 cm, respectively, where the dimensions of the thermocouple legs were ≈6 mm × 2 mm. The second TEG produced 7 μW for ΔT of 70 K. The third TEG had a saw-like design and was placed onto body skin. The third TEG produced an open-circuit voltage of 4.2 mV at room temperature when it is integrated on body skin.

2.2.3. Pseudo-3D Printed SnSe

In 2019, Burton et al. used a mold to form printed SnSe 3D cuboids (Figure 12j) and achieved a *ZT* value of 1.7 at 758 K.^[36] 1.7 is the highest *ZT* of any printed thermoelectric material to date, exceeding even the values achieved in tellurides. In this study, p-type SnSe was used and a cube of approximately 1 cm³ was made. This was achieved by additive manufacturing, depositing ≈2 mm in a mold at a time with a SnSe ink containing a carboxymethyl cellulose binder, allowing this to set on top a hot plate at 393 K in air before further filling the mold another ≈2 mm. This process was repeated until the desired size sample was achieved. A maximum power factor of 280 μW m⁻¹ K⁻² was observed at 855 K. A proof-of-concept all p-type TEG was produced, which produced a maximum power output of 20 μW at 772 K. This power value was a vast improvement over the SnSe thin-film counterparts (0.09 μW), also done by Burton et al.^[82] This power output is far lower than the high *ZT* suggests is possible, this can be attributed to the large contact resistances between the thermoelectric elements and the Cu tape electrical connectors.

2.3. Sulfides

Another chalcogen that can be employed is sulfur and its related compounds. Sulfur is four to five time orders of magnitude more abundant than its related chalcogens, and so in theory would be cheap to use for thermoelectric applications.^[87] Binary metal sulfides such as Bi₂S₃ and Cu₂S are among the most researched sulfides for thermoelectric applications, although many chalcocite (Cu₂S) related minerals have been investigated, such as stannite (Cu₂FeSnS₄), kesterite (Cu₂SnS₄), chalcopyrite (CuFeS₂), bornite (Cu₅FeS₄), colusite (Cu₂₆V₂[As,Sn,Sb]₆S₃₂) and tetrahedrite ([Cu,Fe]₁₂Sb₄S₁₃).^[87]

Chen and Uher studied the bulk properties of Bi₂S₃ in 1997.^[88] They found that Bi₂S₃ has a *ZT* slightly in excess of 0.05 at 250 K. While they found Bi₂S₃ compounds can have thermal conductivities comparable to or even lower than Bi₂Te₃, the lower *ZT* was attributed to a wide bandgap for thermoelectrics of 1.3 eV which results in a low electrical conductivity of 10⁻⁴ S cm⁻¹ at room temperature. He et al. showed that Cu deficient Cu₂S exhibits a maximum *ZT* of 1.7 at 1000 K.^[89] The high *ZT* is largely attributed to the low thermal conductivity of lower than 0.6 W m⁻¹ K⁻¹ over the whole temperature range studied (300–1000 K).

2.3.1. 3D Printed Cu₂S

In 2019, Burton et al. applied their pseudo 3D printing technique of additive layer mold printing, previously applied to SnSe,^[36] to Cu_{2-x}S and achieved a *ZT* of 0.63 (±0.09) at 966 K.^[37] While this is considerably lower than the *ZT* achieved in SnSe, Cu_{2-x}S has the benefits of containing more Earth-abundant elements than SnSe and being non-toxic. The *ZT* of 0.63 was achieved in Cu_{1.97}S at the maximum temperature studied, while no higher temperatures were studied due to the thermal instability of Cu_{2-x}S at more elevated temperatures. Thermoelectric measurements were repeated on the same samples, which showed a steady drop in *ZT* with each cycle due to the thermal instability of Cu_{2-x}S. Nevertheless at 966 K, the electrical conductivity, Seebeck coefficient, and thermal conductivity were 43 S cm⁻¹, 250 μV K⁻¹ and 0.42 W m⁻¹ K⁻¹, respectively. The mechanically alloyed (MA) power, the ink, a schematic of the printing process and a photo of a typical printed sample can be seen in Figure 13.

3. Other Inorganic

While printed inorganic thermoelectrics have been extensively studied using chalcogenide materials, printing of other inorganic materials has been much more limited. A number of papers have been published, however, which span from well-studied thermoelectric material groups such as oxides and zinc-based compounds, to less well investigated thermoelectric materials such as silicon and even pure metals. A variety of devices have been constructed from these printed materials which have been shown to have a diversity of functions, including thermocouples, hydrogen sensors, and heat flow sensors. Devices with reported power outputs are summarized in Table 3.

3.1. Metal

In 1794, the Seebeck effect was first observed by Alessandro Volta in an iron rod,^[90] however, while metals exhibit high electrical conductivity they exhibit low Seebeck coefficients and have high thermal conductivities compared to semiconductors. This leads to heavily doped semiconductors having the highest *ZT* values.^[4] Metals are still used in thermocouples however, and there have been a few studies looking at printing thermocouples which may also have the ability to be self-powered using the thermoelectric effect. Their thermoelectric properties are depicted in Figure 14 (also Table S7, Supporting Information), along with images of the printed materials and schematics of manufacturing techniques. Printing of materials is also known to lower their thermal conductivity due to increased phonon scattering sites compared to fully dense materials, therefore printed metals may act more like heavily doped semiconductors than typical metals and therefore be of interest to study.

Duby et al.^[93,94] were the first to study the Seebeck coefficient of printed metals. NiCr, Fe, Ni, Ag, Ni/panipol and NiCr/Ag were all screen printed with a variety of binders (polyester, cellulose, polyaniline) and gave Seebeck coefficients of 9.37,

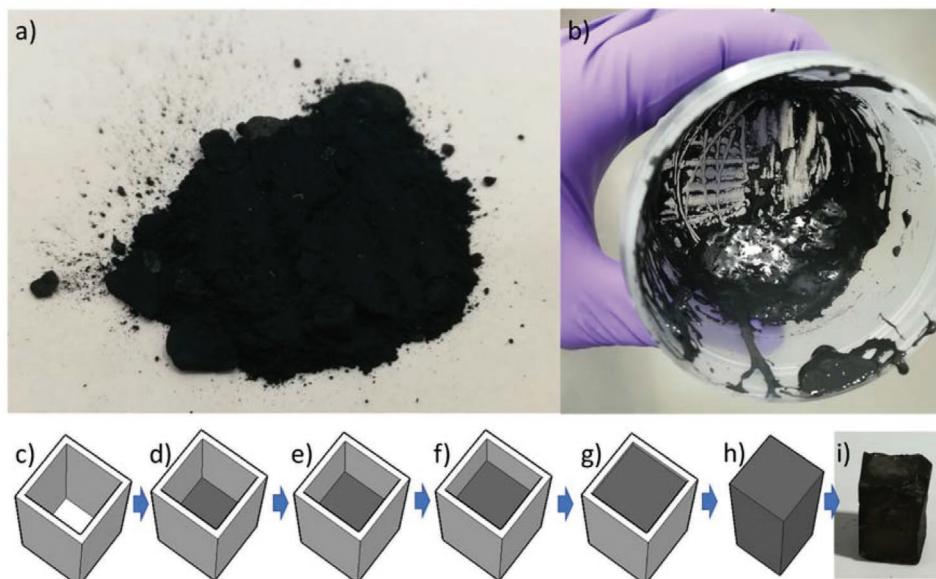


Figure 13. Schematic illustration and photos of the 3D printed process used to fabricate printed Cu_{2-x}S : a) MA Cu_{2-x}S powder, b) ink made of the MA powder and a water and sodium carboxymethyl cellulose binder solution, c–h) schematic diagram of the layer-by-layer mold printing technique, i) a photograph of a typically produced sample. Reproduced under the terms of an Attribution 4.0 International (CC BY 4.0) license.^[37] Copyright 2019, The Authors. Published by RSC.

4.96, -10.3, 2.57, -12.5, and $4.14 \mu\text{V K}^{-1}$ respectively. Thermocouple devices were made, and while the current output and thus power was not measured, device voltages of up to 3.5 mV were reported. This work highlighted the ability to print thermocouples but failed to fully investigate the thermoelectric properties of the materials that were printed.

Markowski et al.^[91,95–97] published a series of papers on screen printed PdAg, Ag, and Ni, while these were also used as thermocouples they were also intended for thermoelectric microgenerators. While the thermoelectric properties of the isolated materials were not measured, the thermoelectric properties of the printed thermoelectric microgenerators were at near room temperature. The best results were observed when using Ag and Ni legs. These legs gave a combined Seebeck coefficient of $25 \mu\text{V K}^{-1}$, a conductivity of $18\,300 \text{ S cm}^{-1}$

and a power factor of $1140 \mu\text{W m}^{-1} \text{ K}^{-2}$. The devices themselves (Figure 14d) gave an output power of up to $110 \mu\text{W}$ with a ΔT of 190 K, after having been cured at 973 K.

Markowski et al.^[98,99] also looked into the thermoelectric properties of magnetron sputtered Ge doped with different combinations of Sb, W, Ta, Au, V, and Hf to make thermoelectric microgenerators and laser power sensors with the other thermocouple arm being made from screen printed metal. The best magnetron sputtered thermoelectric materials properties were seen with atomic percentage composition of 88.6:8.2:3.2 Ge: Au: Hf. A Seebeck coefficient of $140 \mu\text{V K}^{-1}$, electrical conductivity of 200 S cm^{-1} and a resulting power factor of $392 \mu\text{W m}^{-1} \text{ K}^{-2}$ were observed. While this composition offered the best material properties, the best thermoelectric generators were formed with 93:2.5:4.5 Ge: Sb: W as they could form

Table 3. Summation of nonchalcogenide based printed inorganic thermoelectric generators that report power outputs.

Material	Printing technique	Substrate	Thickness [mm]	Power [μW]	Power density [mW cm^{-2}]	Cure time [min]	Cure temperature [K]	Refs.
Ag/Ni	Screen	Low temperature cofired ceramic	N/A	110	N/A	N/A	973	[91]
$\text{Ge}_{93}\text{Sb}_{2.5}\text{W}_{4.5}^{\text{a)}}$ /PdAg	Screen	Low temperature cofired ceramic	0.003	$19.6^{\text{a)}}$	N/A	N/A	N/A	[99]
Ag/Ni-2	Dispenser	Polyimide	0.053	14.6	N/A	180	623	[92]
$\text{MnSi}_{1.74}/\text{Mn}_{0.7}\text{Fe}_{0.3}\text{Si}_{1.68}$ with PVC	Doctor-blade	N/A	0.500	N/A	11.7	60	423	[108]
ZnSb with α -terpineol and DisperBYK-110	Screen	Si wafer	0.026	N/A	0.22	20	573	[109]
ZnSb/CoSb ₃ with α -terpineol and DisperBYK-110	Screen	Alumina	0.050	N/A	0.1	10	773	[110]
IZO	Spin coating	Glass	0.000015	0.0001	N/A	70	373–623	[112]
TiN/NbN	Screen	α -alumina	0.002	N/A	100	60	1273	[117]

^{a)}The $\text{Ge}_{93}\text{Sb}_{2.5}\text{W}_{4.5}$ p-type legs were not printed.

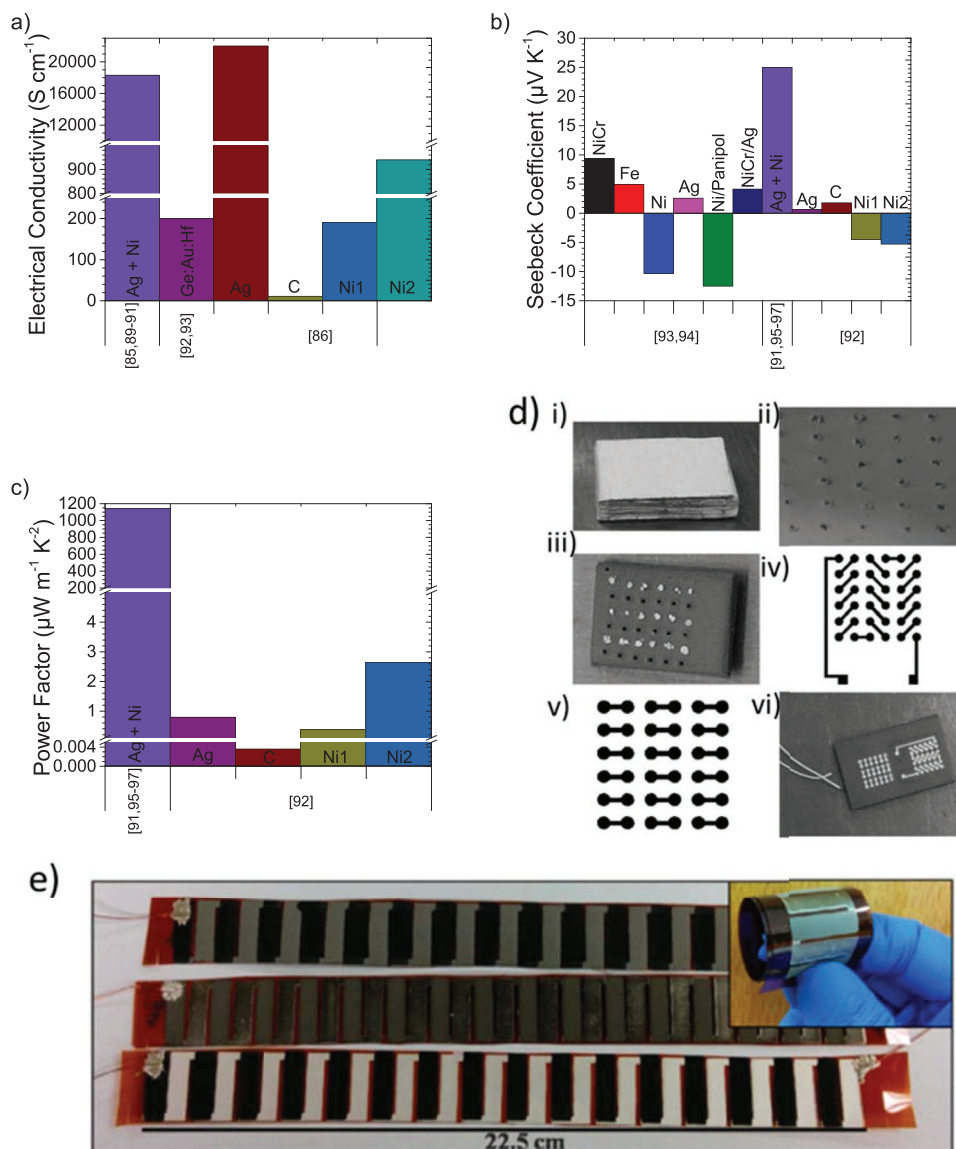


Figure 14. Thermolectric properties of printed metals. Values presented represent the sample and temperature where the peak power factor was measured: a) electrical conductivity, b) Seebeck coefficient, c) power factor. This data is also represented in Table S7 (Supporting Information). Images of printed metallic thermolectric modules: d) photographs and diagrams of Ag/Ni module assembly i) low temperature cofired ceramic substrate, ii) after vias drilling, iii) after filling with Ag legs and curing (875 °C for 2 h), iv) mask for screen-printing top junction paths, v) mask for screen printing bottom junction paths, vi) final structure (reproduced with permission.^[91] Copyright 2008, Elsevier), e) photographs of nickel, carbon and silver modules on Kapton (reproduced with permission.^[92] Copyright 2016, Springer).

3 μm layers, instead of 0.7 μm of Ge:Ag:Hf. Using screen printed PdAg as the second thermocouple arm and having 35 junctions, an output power of 19.6 μW at a ΔT of 100 K was observed.

More recently Ankireddy et al.^[92] investigated the thermolectric properties of printed Ag, Ni, and carbon. In this study, the thermolectric properties of the individual materials were studied, with the values measured at room temperature. Ag and carbon were seen to be p-type with Seebeck coefficients of 0.6 and 1.8 $\mu\text{V K}^{-1}$, respectively. Two types of Ni were also printed which were called Ni-1 and Ni-2. The inks both used PVP as a binder, but the source of Ni and dispersion solvent

was different. Nonetheless, both printed types of Ni were observed to be n-type with Seebeck coefficients of -4.5 and -5.3 $\mu\text{V K}^{-1}$ for Ni-1 and Ni-2. All of the Seebeck coefficients were seen to be lower than those of the bulk materials, but by no more than an order of magnitude. The electrical conductivities of the samples were 22 000, 11, 190, 940 S cm^{-1} for Ag, carbon, Ni-1, and Ni-2, respectively. This is also the first work to investigate the thermal properties of the printed metal samples for thermolectric applications. The thermal conductivity was not measured, however, the thermal resistance of all the films is stated as 3.42×10^3 , 2.65×10^6 , 1.78×10^5 , and $2.73 \times 10^4 \text{ K W}^{-1}$ for Ag, carbon, Ni-1, and Ni-2, respectively.

Thermoelectric generators of every p–n type combination were made, with example devices pictured in Figure 14e. The optimum combination was seen to be Ag with Ni-2, that generated a power output of 14.6 μW at the largest ΔT of 113 K.

3.2. Silicon

In 2007, Lechner et al.^[100] studied the thermoelectric properties of printed nanocrystalline layers. The printed layers' carrier concentration was modified with B to make p-type Si and with P to make n-type Si. The films were made by spin coating Si nanocrystals dispersed in ethanol onto polyimide. The resulting 0.7 μm thin films were laser annealed. Samples doped with B to give a carrier concentration of 10^{19} cm^{-3} gave a Seebeck coefficient of 300 $\mu\text{V K}^{-1}$, while those doped with P to three times the carrier concentration gave a Seebeck coefficient of 220 $\mu\text{V K}^{-1}$ and an electrical conductivity of 0.4 S cm^{-1} . This yields a power factor of 1.9 $\mu\text{W m}^{-1} \text{ K}^{-2}$, which is roughly a factor of 10^3 smaller compared to bulk Si of the same carrier concentration.^[101] The authors conclude this is due to the high porosity of the samples causing a large number of interfaces between the layers. This should have a benefit in lowering the thermal conductivity however, and from studying the Stokes-to-anti-Stokes intensity ratio in the micro-Raman as a function of the laser power, they conclude the upper limit for the thermal conductivity of these samples is $<10^{-2} \text{ W K}^{-1} \text{ cm}^{-1}$, which is at least 130 \times smaller than bulk Si. This gives a conservative estimate of ZT at 10^{-3} , although in reality it could be closer to that of bulk Si at 10^{-2} .^[102]

Silicon thin films were inkjet-printed and photonic annealed by Drahi et al.,^[103–105] while they were not investigated for full thermoelectric performance a thermal conductivity as low as 0.26 $\text{W m}^{-1} \text{ K}^{-1}$ was observed.

Si thermoelectric generators were printed by Khan et al.^[106] using Si microwires. Si microwires were developed through standard photolithography and etching steps then transferred from a silicon on insulator wafer onto polyimide using stamp-assisted transfer printing.^[107] No thermoelectric material parameters were measured of the microwires, but a device was made using the technique (Figure 15a) and was shown to have an open-circuit voltage of 9.3 mV at a ΔT of 54 K. Power output is unknown, however, as no measurements of current were reported.

Manganese–silicon has also been investigated as a printable thermoelectric material, with the formation of both p-type $\text{MnSi}_{1.74}$ and n-type $\text{Mn}_{0.7}\text{Fe}_{0.3}\text{Si}_{1.68}$ allowing for a complete thermoelectric generator to be printed.^[108] The devices were printed by the doctor-blade method using a polyvinyl butyl alcohol binder and methylbenzene solvent. Several 45 μm thick layers of the n-type material were printed on top of each other, with the optimum generator made with thickness layers of 500 μm . These were dried and then insulated with a screen-printed $\text{SiO}_2\text{--B}_2\text{O}_3$ 25 μm thick layer. On top this process was repeated with the p-type ink. This layering pattern was repeated with the optimum generator consisting of 10 of these p/n-pair layers. The printed devices were then hot pressed at 50 MPa in Nitrogen at 423 K for 60 min followed by SPS at the same pressure for 15 min at 1173 K. While no thermoelectric materials properties were measured, the printed devices were able to generate 11.7 mW cm^{-2} with a hot side of 973 K and a cold side of 293 K, while a device mounted on an engine exhaust (Figure 15b) was able to produce up to 5.5 mW cm^{-2} .

3.3. Zinc

Another material set that has been printed for thermoelectric investigation is Zn-based compounds. In 2011, Lee et al.^[109]

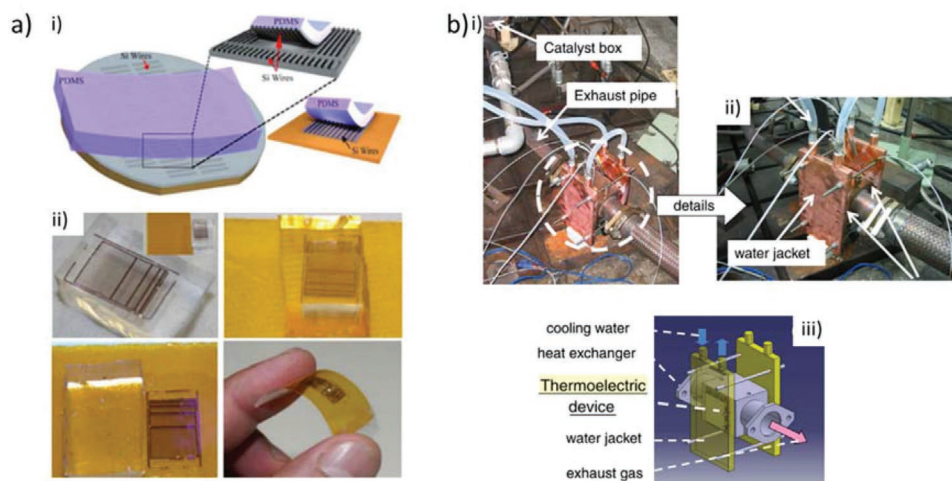


Figure 15. Printing of Si thermoelectric modules. a) transfer printing of Si nanowires: i) the steps related to transfer printing of Si wires from silicon on insulator wafers to flexible substrates, ii) results at stages of the transfer printing, wired picked-up by PDMS stamp (top left), PDMS stamps on adhesive SU-8 layer (top right), wires transferred to substrate after removing PDMS (bottom left), wires in bent mode (bottom right). Reproduced under the terms of an Attribution 4.0 International (CC BY 4.0) license.^[107] Copyright 2016, The Authors. Published by IEEE. b) $\text{MnSi}_{1.74}/\text{Mn}_{0.7}\text{Fe}_{0.3}\text{Si}_{1.68}$ printed module mounted onto an engine exhaust of an engine test bench consisting of 0.66-L turbo engine, heat exchanger and water jackets: i) overview of thermoelectric heat harvesting system, ii) thermoelectric devices are held between the heat exchanger and water jacket, iii) schematic view of heat exchanger and thermoelectric devices/water jacket. Reproduced with permission.^[108] Copyright 2014 Springer.

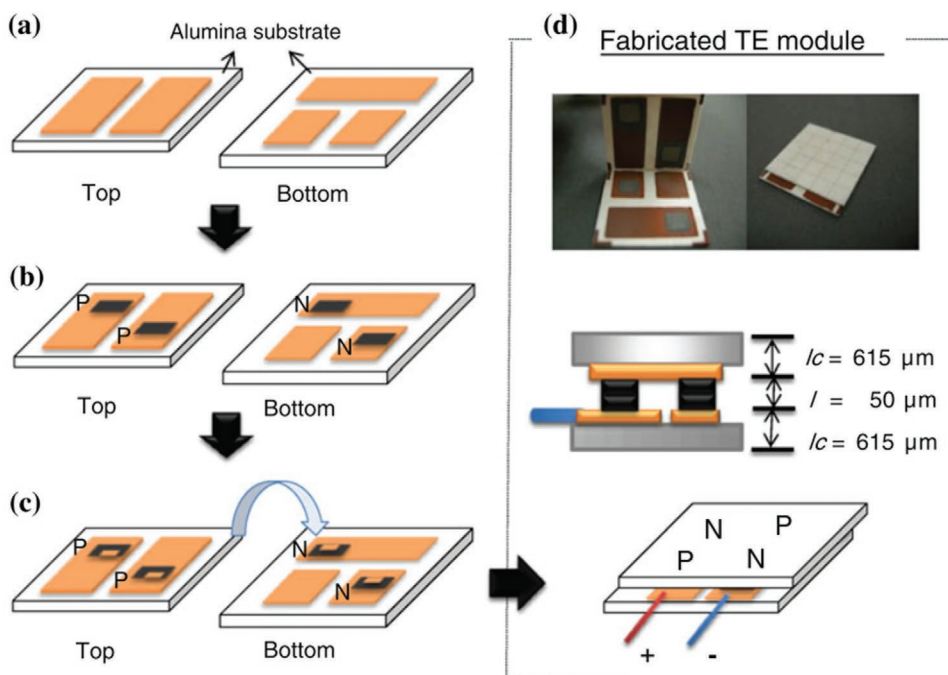


Figure 16. Process flow for the fabrication of a ZnSb/CoSb₃ thermoelectric module using screen-printing. a) First step: Cu paste is deposited via screen-printing on an alumina substrate and annealed at 773 K for 10 min, b) second step: ZnSb is deposited on the top substrate as a p-type material, and CoSb₃ is deposited on the bottom substrate as an n-type material. The sample is then annealed at 773 K for 10 min. c) Third step: the top and bottom substrates are bonded using Cu paste. d) Photographs and schematics of the fabricated thermoelectric module. Reproduced with permission.^[110] Copyright 2011, Elsevier.

screen printed ZnSb in Si wafers. The ZnSb inks were made with a mixture of α -terpineol and DisperBYK-110 and the printed films were cured 20 min at 573 K followed by a further cure for 10 min at 853 K. The screen-printed films were 26 μm thick and at 853 K exhibited a Seebeck coefficient of $109 \mu\text{V K}^{-1}$ and an electrical conductivity of 892 S cm^{-1} , with a resulting power factor of $1060 \mu\text{W m}^{-1} \text{ K}^{-2}$. While the thermal conductivity was not measured, basic devices consisting of 4 legs were made consisting of legs $2.5 \text{ cm} \times 0.5 \text{ cm}$ in dimension. The maximum power output of these devices was measured to be 0.22 mW cm^{-2} at a working temperature of 523 K with a ΔT of 70 K.

The same group used the screen-printed ZnSb in conjunction with screen-printed CoSb₃ to make a full p and n leg printed thermoelectric device.^[110] The CoSb₃ was observed to produce a Seebeck coefficient of $-49 \mu\text{V K}^{-1}$ and an electrical conductivity of 211 S cm^{-1} at 773 K, giving a power factor of $50.5 \mu\text{W m}^{-1} \text{ K}^{-2}$. The ZnSb with CoSb₃ devices can be seen in **Figure 16** and consist of 2 legs of ZnSb and 2 legs of CoSb₃, which are connected via screen-printed Cu paste and sandwiched between alumina. Each leg was $5 \text{ mm} \times 5 \text{ mm}$ and $50 \mu\text{m}$ thick, with 5 mm gaps between the legs. The thermoelectric generator was able to output up to 0.1 mW cm^{-2} with an output voltage of 27 mV, both with a temperature difference of 50 K. This is seen to be lower than ZnSb by itself however, which is attributed to the structure not having been optimized and to the high contact resistance caused by the non-optimized bonding process. Nevertheless, a working all printed alternating p and n leg thermoelectric device was produced using abundant materials.

3.4. Oxides

Oxides of Zn compounds have also been investigated for printed thermoelectrics, with thermoelectric performances summarized in **Figure 17a–c** (also Table S8, Supporting Information). In the simplest form, Hoong et al.^[111] looked at inkjet-printed ZnO which was seen to be n-type, while also looking at inkjet printed Zn_xFe_{3-x}O₄ which was seen to be p-type. Curing for 6 h at 473, 573, and 673 K were investigated, however, optimum results were seen with the curing at 673 K for ZnO and there was negligible difference between curing temperature for Zn_xFe_{3-x}O₄, therefore only results for curing at 673 K will be discussed here. The substrate for the inkjet-printed films was glass and all thermoelectric properties were measured at room temperature. A minimum of 50 print cycles needed to obtain homogeneous films, the thickness of which was $9 \mu\text{m}$. The electrical conductivity of undoped ZnO was seen to be modest at 15 S cm^{-1} , however with an aluminum doping level of 0.04 the conductivity was improved to 90 S cm^{-1} . The corresponding Seebeck coefficients for these samples were -18 and $-14 \mu\text{V K}^{-1}$, respectively, which gives corresponding power factors of 0.49 and $1.77 \mu\text{W m}^{-1} \text{ K}^{-2}$. Compared to pellets of the same materials, the electrical conductivity is seen to be slightly improved, something rarely seen for printed materials. The Seebeck coefficients are seen to be lowered by approximately a factor of 3 however, so the power factors are ultimately significantly lower. Zn_xFe_{3-x}O₄ was investigated as a p-type material, with various x values from 0.2 to 1.0 investigated. The optimum x value was seen to be 1.0, so only ZnFe₂O₄ will be discussed in more detail. Electrical conductivity was seen to

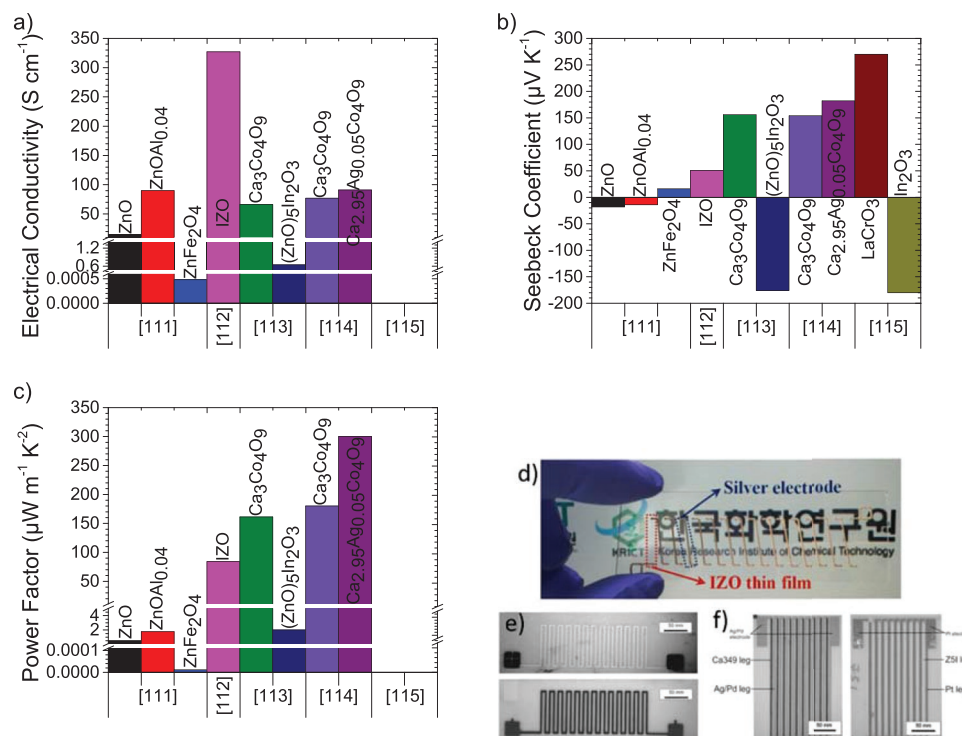


Figure 17. Thermolectric properties of printed oxides. Values presented represent the sample and temperature where the power factor was measured: a) electrical conductivity, b) Seebeck coefficient, c) power factor. This data is also represented in Table S8 (Supporting Information). Images of printed oxide modules: d) IZO module consisting of 15 legs (2 mm × 15 mm) separated with 2 mm gaps and connected with silver electrodes. Reproduced with permission.^[112] Copyright 2016, ACS. e, f) (ZnO)₅In₂O₃ (e top and f right) and Ca₃Co₄O₉ (e bottom and f left) screen printed modules. Reproduced with permission.^[113] Copyright 2015, Elsevier.

be $0.48 \times 10^{-3} \text{ S cm}^{-1}$ and the Seebeck coefficient $16 \mu\text{V K}^{-1}$, while the electrical conductivity seen to be similar to the pellets while the Seebeck coefficient was roughly half. Due to the low electrical conductivity, the films show a very low power factor of $12.3 \times 10^{-6} \mu\text{W m}^{-1} \text{ K}^{-2}$. The large difference in the electrical conductivities between the n- and p-type materials is likely the cause for the lack of thermoelectric devices being produced, despite showing the ability to print both types of semiconductors.

Indium zinc oxide (IZO) has also been investigated through spin coating onto glass, using soluble metal oxide precursors containing metal-coordinated fuel and oxidizer ligands.^[112] The films were 15 nm thick and the thermoelectric properties were only measured at room temperature. The highest power factor of $84 \mu\text{W m}^{-1} \text{ K}^{-2}$ was seen with a In to Zn ratio of 6:2 which gave an electrical conductivity of 327 S cm^{-1} and a Seebeck coefficient of $50.6 \mu\text{V K}^{-1}$. Before measurement, the spin-coated films were cured at 373 K for 10 min followed by a cure at 623 K for 1 h. A primitive device (Figure 17d) was made with the IZO films consisting of 15 legs (2 mm × 15 mm) separated with 2 mm gaps and connected with silver electrodes fabricated using a dispenser. With a ΔT of 10 K across the device an output power of 0.10 nW was achieved and an open-circuit voltage of 11 mV.

(ZnO)₅In₂O₃ and Ca₃Co₄O₉ thick films of an unspecified thickness were screen printed on alumina with 70 wt% active ingredient, 29.4 wt% of an in-house organic vehicle, and 0.6 wt% wetting agent ESL 809.^[113] The printed films needed

to be cured to achieve the best results, with the highest power factors being observed when Ca₃Co₄O₉ was cured at 1173 K and (ZnO)₅In₂O₃ was cured at 1623 K. Both were cured in a belt furnace for 15 min in an unspecified atmosphere. Power factors were only reported at 573 K and were 161 and $2 \mu\text{W m}^{-1} \text{ K}^{-2}$ for Ca₃Co₄O₉ and (ZnO)₅In₂O₃ respectively with Seebeck coefficients of 156 and $-176 \mu\text{V K}^{-1}$, and electrical conductivities of 66.2 and 0.646 S cm^{-1} . The electrical conductivity of Ca₃Co₄O₉ was seen to rise to 73.0 S cm^{-1} at 773 K. While the electrical characteristics were seen to be inferior to those of the bulk materials, the Seebeck coefficients were seen to be similar and in some cases higher. The results show that it would be possible to screen print a complete n and p leg oxide TEG, however, this was not done in this work, presumably due to the $\approx 100\times$ difference observed in electrical conductivity. While power output is not stated, individual TEGs of each material were printed (Figure 17e,f).

Ca₃Co₄O₉ was also screen printed by Nong et al.,^[114] with films of $\approx 60 \mu\text{m}$ being printed onto a $290 \mu\text{m}$ thick Ce_{0.9}Gd_{0.1}O_{1.95} (CGO) substrate (KERAFOL). The ink was a powder dispersant binder mixture of unspecified quantities. The optimum results were seen when the printed films were sintered for 2 h in air at 1223 K. The samples produced here, are similar to those produced by Rudež et al.,^[113] but they also explore Ag doping. At 612 K, the electrical conductivity was 76.9 S cm^{-1} , while with small Ag doping (Ca_{2.95}Ag_{0.05}Co₄O₉) the electrical conductivity was improved to 90.9 S cm^{-1} . At this temperature, the Seebeck coefficient was seen to be 182 and

154 $\mu\text{V K}^{-1}$ for with and without silver respectively, with power factors of 300 and 180 $\mu\text{W m}^{-1} \text{K}^{-2}$.

$\text{La}_{1-x}\text{Sr}_x\text{CrO}_3$ and In_2O_3 have also been screen printed onto alumina.^[115] Ethyle cellulose and terpenol were used to make the ink and glass power was also used in the In_2O_3 inks. The printed films were calcined at 1523 K for 2 h before any contacts were added to perform measurements. Increasing Sr content in $\text{La}_{1-x}\text{Sr}_x\text{CrO}_3$ was seen to simultaneously decrease the electrical resistivity and Seebeck coefficient, with $\text{La}_{0.6}\text{Sr}_{0.4}\text{CrO}_3$ (the highest level of Sr doping studied) having a Seebeck coefficient of $\approx 200 \mu\text{V K}^{-1}$ at 1400 K (LaCrO_3 has a Seebeck of $\approx 270 \mu\text{V K}^{-1}$ at 1400 K). This is due to SrCrO_3 having metallic behavior,^[116] and the closer LaCrO_3 become to SrCrO_3 , the higher the carrier concentration becomes and thus the lower the electrical resistivity and Seebeck coefficient becomes.^[4] The electrical resistivity (and thus conductivity) is hard to interpret due to the sharp reduction in electrical resistivity with increasing Sr content making the plot hard to read, however the electrical resistivity has dropped from $>4 \text{ K}\Omega \text{ cm}$ to $<0.1 \text{ K}\Omega \text{ cm}$ when going from 10% to 40% Sr content. Data for the electrical conductivity of In_2O_3 is not shown, however, the Seebeck of LaCrO_3 and In_2O_3 are simultaneously measured, implying In_2O_3 has a Seebeck coefficient of $\approx -180 \mu\text{V K}^{-1}$ at 1400 K. While no power output of a TEG was measured, a thermocouple of $\text{La}_{0.7}\text{Sr}_{0.3}\text{CrO}_3\text{-In}_2\text{O}_3$ was produced that produced 400 mV with a ΔT of 1200 K. The thermocouple shows promise as a thermal sensor with a high sensitivity for temperature sensing in harsh environments.

NiO doped with Li and Na were screen printed onto alumina, to make a thermoelectric hydrogen sensor. The inks also contained a blend of terpineol and ethyl cellulose. Each printed layer ($\approx 13 \mu\text{m}$) of the films was dried for 5 min at 473 K, before being dried again at 1273 K for 2 h. Multiple layers were printed to achieve a thickness of up to 56 μm . While no thermoelectric properties were measured, a primitive device was able to output a potential of up to 8 mV when exposed to temperatures more than 358 K.

3.5. Nitrides

While not a typical thermoelectric material group, Hashimoto et al. screen-printed 0.5 cm^2 Ti and Nb films before exposing them to a $\text{NH}_3\text{-H}_2$ atmosphere at 1273 K to turn them into 2 μm films of TiN and NbN respectively.^[117] The NbN films exhibited conductivity values of up to 1000 S cm^{-1} at 673 K. Thermoelectric devices were seen to give a power output of up to 0.1 W cm^{-2} .

4. Organic/Carbon

Carbon-based thermoelectrics are advantageous over inorganic materials in that they are largely nontoxic and are significantly lighter, making them potentially ideal for applications such as wearable thermoelectrics. Carbon-based thermoelectric materials have been shown to be processable onto flexible substrates such as polyimides, polyethylene terephthalates (PETs), and paper.^[118,119] When examining the materials properties for

use in wearable textile TEG devices for example, it is essential that the design considerations account for mechanical durability and allow tuning for desired viscoelastic traits.^[120] This is because the devices will be under mechanical stress when bent or stretched.^[121–123] Printed TEGs formed from light weight and low atomic mass elements such as carbon, nitrogen, or sulfur offer potential for environmentally more sustainable atom economy than devices composed of less abundant Earth minerals such as germanium, selenides, and tellurides.^[124–126] Carbon-nanotubes (CNTs), graphene, aniline, pyrrole, and thiophene-based polymers and nanomaterials are prime examples.^[127–131] For the printed carbon-based TEGs to be commercialized and useful in functional electronic devices, several optimizations must occur.^[120,124,132] For instance, improving printing quality to yield homogenous films with high process reproducibility is necessary.^[133] Other improvements involve synthesizing materials with thermal stability at least slightly higher than the operating temperature. The human body is not comprised of flat surfaces therefore, the materials should be malleable during product development and designed to fit the body's curvature and offer potential for large surface area coverage.^[124,134,135] If the TEG is introduced into clothing or in close/direct contact to human skin, it should be nontoxic and non-reactive during its operation lifetime.^[120,136,137]

Most carbon-based thermoelectrics are solution processable, therefore inks with various rheological properties like viscosity, particle size, diameter, as well as surface tension can be tuned for an appropriate printing system.^[138–142] When using inkjet or flexographic printing techniques, the ink viscosity is usually lower than in a technique like screen printing. This, however, is an oversimplification because even if the appropriate viscosity for each printing system is obtained, it is also important to tune for appropriate surface tension between the substrate and ink to prevent spreading beyond the designated pattern.^[129,140,143] It is paramount therefore, to tune the surface energy of inks relative to the substrate to allow for droplets to wet on substrate and spread with a desired flow to form films within the expected pattern.^[144,145] This is a challenge for large area film formation as the surface energy is dependent on the surface area of the substrate.^[146,147]

The thermoelectric performance of printed carbon-based thermoelectrics varies significantly in the literature. To allow for comparison of the components that make up ZT and ZT itself, the peak ZT or power factor values reported for all papers in this section are summarized in **Figure 18** (also Table S9, Supporting Information). Devices with reported power outputs are summarised in **Table 4**.

4.1. Printed Carbon-Nanotube (CNT) Based Thermoelectrics

CNTs can be printed as well dispersed suspensions can be formed.^[141] In 2010 Najeeb et al.^[148] conducted a study whereby a carboxylic acid functionalized, and a nonfunctionalized single-walled carbon nanotube/poly(3,4-ethylenedioxythiophene) polystyrene sulfonate (SWNT/PEDOT:PSS) composites were synthesized. A piezoelectric inkjet printer was employed to create patterned conductive strips from the solution with a width of 100 μm and lengths ranging between 1 and 5 cm. It

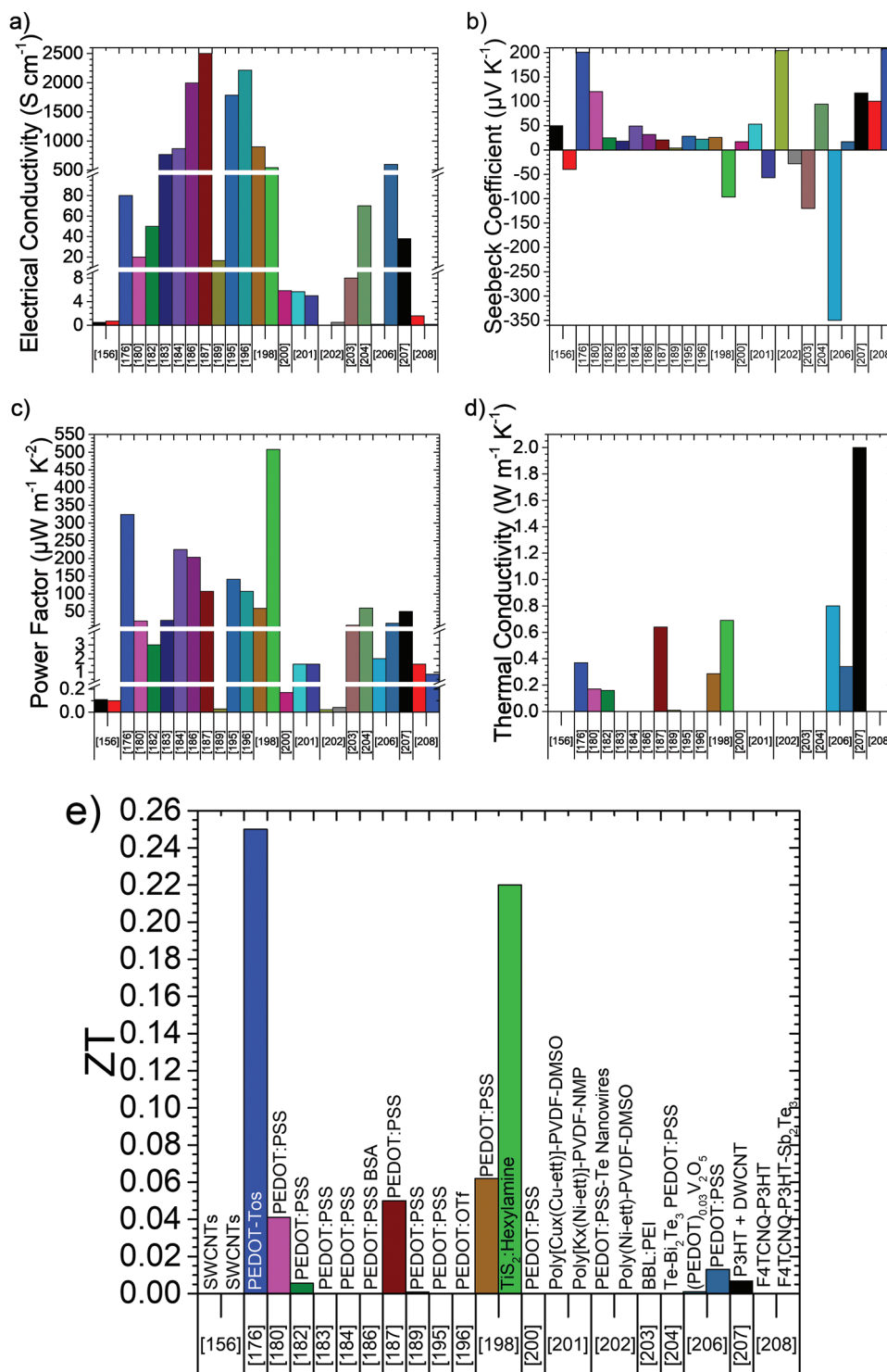


Figure 18. Thermoelectric properties of carbon based printed thermoelectrics (materials are labeled in part e). Values presented represent the sample and temperature where the peak ZT value was observed, if ZT was not reported then values represent the peak power factor measured: a) electrical conductivity, b) Seebeck coefficient, c) power factor, d) thermal conductivity and e) ZT. This data is also represented in Table S9 (Supporting Information).

was discovered that the electrical conductivity for the functionalized patterns was four times higher than that of the nonfunctionalized SWNT composites due to improved dispersibility

of CNTs owing to more hydrophilic interactions between the carboxylic groups and PSS components in the polymer matrix. Further still, when the natural gum (gum arabica) was used

Table 4. Summation of organic based printed thermoelectric generators that report power outputs.

Material	Printing technique	Substrate	Thickness [mm]	Power [μ W]	Power density [mW cm^{-2}]	Cure time [min]	Cure temperature [K]	Refs.
MWCNT	Casting	PVDF	0.04	0.137	N/A	960	373	[149]
CNT-polystyrene	Screen	Polyethylene naphtholate	0.075	N/A	0.0055	N/A	N/A	[150]
PEDOT-Tos/carbon	Inkjet	Silicon	0.003	0.00113	N/A	N/A	308	[176]
TTF-TCNQ+PVC/PEDOT-Tos	Inkjet	Silicon	0.03	0.128	0.023	N/A	383	[176]
PEDOT:PSS + ethylene glycol	Screen	Paper	0.02	50	N/A	423	30	[183]
PEDOT:PSS/graphene	Roll to roll	"plastic"	0.02	1.92	0.000024	N/A	N/A	[127]
PEDOT-Tos/ Bi_2Te_3	Casting	PET	0.006	0.160	N/A	N/A	N/A	[185]
PEDOT:PSS	Casting	PES	0.003	N/A	0.099	N/A	N/A	[187]
PEDOT:PSS	Casting	Polyimide	\approx 0.001	N/A	0.001	"overnight"	353	[195]
PEDOT:OTf	Spraying	Polyimide	0.00065	1	N/A	10	343	[196]
PEDOT:PSS/ TiS_2 :hexylamine	Screen	PEN	0.007	240	N/A	2	413	[198]
PEDOT:PSS/PTEG-1	Inkjet	PEN	0.025	N/A	0.0000305	"overnight"	393	[199]
PEDOT:PSS	Dispenser	Glass	N/A	0.00517	N/A	30	413	[200]
Poly[Cux(Cu-ett)]-PVDF-DMSO/ Poly[Kx(Ni-ett)]-PVDF-NMP	Inkjet	PET	0.005	0.045	N/A	600	363	[201]
PEDOT:PSS-Te nanowires/ poly(Ni-ett)-PVDF-DMSO	Calligraphy	Paper	0.08	0.028	0.000015	30	333	[202]
PEDOT:PSS/BBL:PEI	Spraying	PEN	0.01	0.056	N/A	N/A	413	[203]
Sb_2Te_3 -PEDOT:PSS/ Bi_2Te_3 -PEDOT:PSS	Aerosol Jet	Polyimide	0.001	0.141	0.1	30	403	[205]
PEDOT + $\text{V}_2\text{O}_5 \cdot n\text{H}_2\text{O}$	Inkjet	Paper	0.004	0.0034	0.266	"overnight"	373	[206]
P3HT + DWCNT	Dispenser	PET	0.03	0.0145	N/A	30	423	[207]

to aid dispersion of the functionalized SWNT an increase in the electrical conductivity (18 \times) was observed relative to the nonfunctionalized SWNT composite owing to the improved extended network between the SWNTs and PEDOT:PSS chains. The study showed that for ink-jet printing, controlling the dispersion of SWNT is vital in preparing the most conductive materials.

In a 2012 study conducted by Hewitt et al., a TEG module was fabricated by creating multiple layers of alternating p- and n-type multiwalled carbon nanotube (MWCNT) sandwiched between the insulating polyvinylidene fluoride (PVDF) layer, to separate the p and n components as expressed in **Figure 19a**.^[149] The as assembled layers mimicked felt fabric and resulted in light weight and flexible modules which resulted in a power factor (PF) and power output that was directly proportional to the number of repeating layers. For the 72-layer module at a load resistance of 1270 Ω , an optimal power output of 137 nW was produced. Due to the unique layer by layer design with an insulating PVDF layer, it was realized that the resistivity was low due to the low concentration of carbon nanotubes at the p–n junction since the main constituent of the junction was comprised of the insulating polymer. Thus, for higher power outputs different designs with higher concentration of CNTs within the p–n junction, and or increasing the number of layers would be required.

In 2013 a flexible functional (carbon nanotube-thermoelectric generator) CNT-TEG was synthesized on a polyethylene naphtholate substrate via a printing procedure utilizing a

printing plate and the solution of the CNT-polystyrene composite as shown in **Figure 19b**.^[150] The device had a low weight per unit area of 15.1 mg cm^{-2} . At a temperature difference of 70 K, the TEG (**Figure 19c**) produced a maximum surface area power density of 55 mW m^{-2} . The module however due to not having a corresponding n-type counterpart exhibited potentially lower power than if both p- and n-type thermoelectric legs were present. The device's performance did not reduce much even at induced mechanical stress (bending). This provides researchers a potential route for printed CNT based devices with significant need for optimization.

Other printing techniques involve using commercially available instruments such as inkjet printers, offering more control than screen and printing plate-based processes with further potential to create patterned electrodes and legs through fine precision of, size (thickness)/(width), and shape (design) of elements in the modules.^[151] Previous studies have shown it is possible to utilize inkjet systems to design patterned functional CNT-based semiconductor devices such as transistors.^[145,152–155] A flexible CNT-based thin film TEG was realized via an inkjet printing procedure by Horike et al.^[156] The group utilized an oxygen electron injection from the HOMO (highest occupied molecular orbital) of the polyvinyl derivative into the LUMO (lowest unoccupied molecular orbital) of the CNT to form relatively stable n-type CNTs. The n-type CNTs were relatively stable with the CNTs retaining n-type characteristics for over 3 weeks in which a module was derived by folding p- and n-type SWCNTs on a flexible substrate. It became

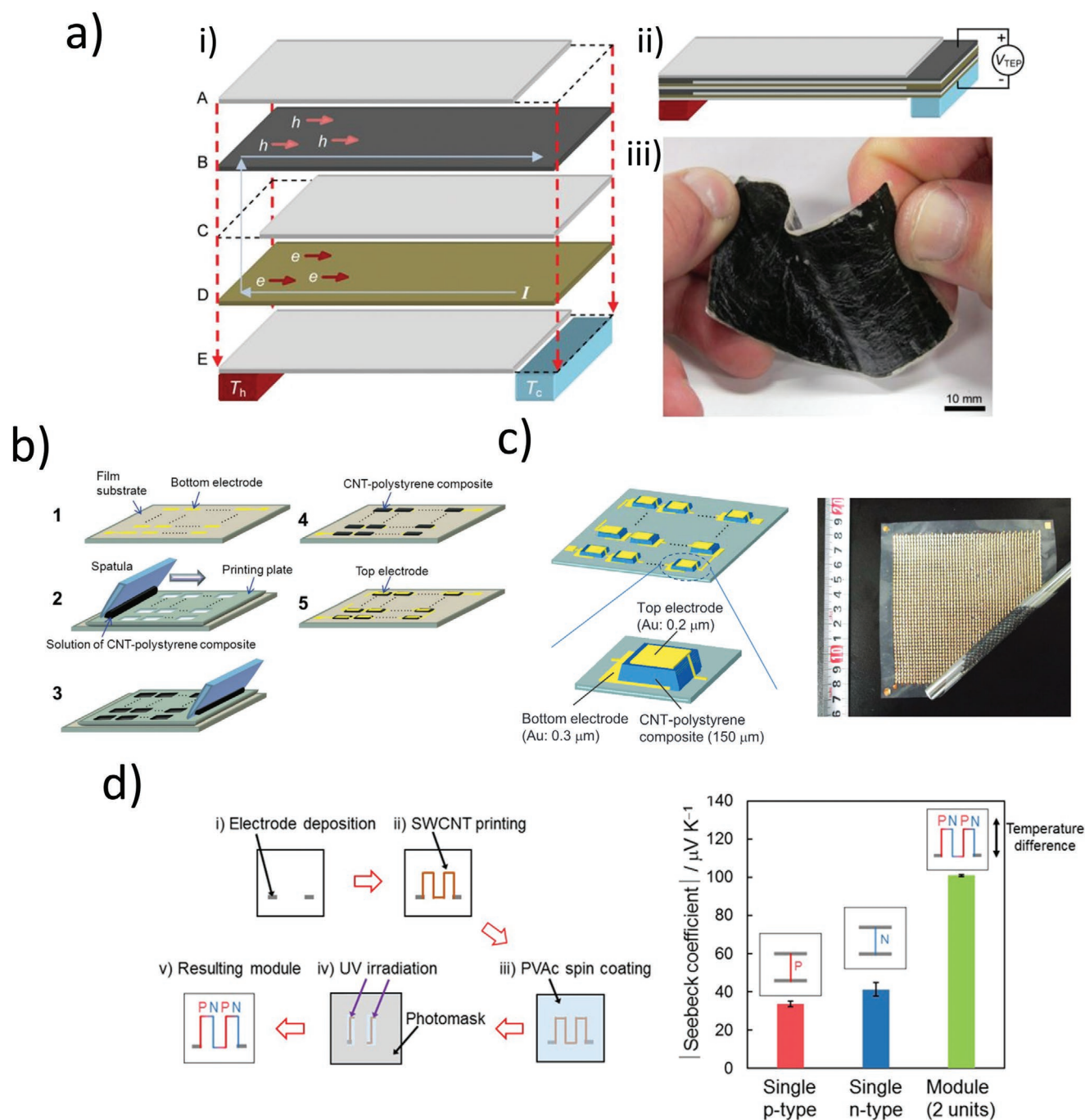


Figure 19. Schematics for making and images of printed CNT based thermoelectric generators. a) Fabrication of all CNT thermoelectric module (i) Layer arrangement for the multi-layered fabric. CNT/PVDF conduction layers (B,D) are alternated between PVDF insulation layers (A,C,E). Every other conduction layer contains p-type CNTs (B), while the others contain n-type CNTs (D). The shorter insulating layers allow for alternating p/n junctions when the stack is pressed and heated to the polymer melting point of 450 K to bond the layers. Layers A–D can be repeated to reach the desired number of conduction layers N. When the film is exposed to a temperature gradient ΔT , charge carriers (holes h , or electrons e) migrate from T_h to T_c resulting in a thermoelectric current I . (ii) The resulting thermoelectric voltage V_{TEP} can be read across the ends of the first and last conduction layers. (iii) The thermoelectric fabric remains flexible and lightweight. Reproduced with permission.^[149] Copyright 2012, ACS. b) Schematic for printing CNT-polystyrene composite TEG and c) dimensions and image of the manufactured TEG. Reproduced with permission.^[150] Copyright 2013, AIP. d) Schematic for the manufacturing of an all SWCNT thermoelectric module by utilizing UV radiation to turn half of the n-type inkjet printed SWCNT legs p-type and a plot of the modules Seebeck performance. Reproduced with permission.^[157] Copyright 2018, Elsevier.

evident that the dopants with the highest HOMO level generally produced n-type SWCNTs with higher negative Seebeck

coefficient. The same relationship however was not observed between the HOMO level and increased electrical conductivity.

The improved stability seemed to be due to the monomers remaining on the CNTs surface thereby creating an encapsulation reducing oxidation.

The Seebeck coefficient of the pristine p-type SWCNT was around $50 \mu\text{V K}^{-1}$ meanwhile the electrical conductivity was 0.5 S cm^{-1} resulting in a power factor of $0.11 \mu\text{W m}^{-1} \text{ K}^{-2}$. For the best-performing SWCNT film treated with the n-type dopant PVA, the Seebeck coefficient of $-40 \mu\text{V K}^{-1}$, an electrical conductivity of 0.7 S cm^{-1} and PF of $0.10 \mu\text{W m}^{-1} \text{ K}^{-2}$ was observed. A TEG consisting of 3 pairs of p- and n-type legs produced a voltage output of 2.2 mV at a ΔT of 10 K. There was a linear trend with increased output voltage when going from 1 pair to 3 pairs of legs, thus inferring low contact resistance. It would be interesting to see if the low contact resistance remains after several hundred legs are connected.

In 2018 Horike et al., further developed the inkjet printing technique to formulate modules more efficiently (Figure 19d).^[157] The group deposited the metal electrode on the quartz substrate and later inkjet printed the SWCNT leg patterns, later doped by the polyvinyl (acetate) by spin coating. Unlike the module design presented in their earlier work, this module was already preconnected having many n-type elements. To form the p-type elements, a photo mask was placed, and ultraviolet (UV) irradiation was used to de-dope (convert the n-type legs back to p-type) to formulate an alternating p-n module. The module produced a thermopower of $100 \mu\text{V K}^{-1}$ for a 2 units (p–n, p–n) system. The easy fabrication process exhibited potential for large area TEG design with room for improvement.

4.2. Printed PEDOT:PSS-Based Thermoelectrics

The discovery of electrically conductive π conjugated organic semiconductors in 1977,^[158] ultimately led to their research for thermoelectric applications.^[159,160] The initial electrical conductivity and power factor of materials such as polyaniline were low at $<8 \text{ S cm}^{-1}$ and $<10 \mu\text{W m}^{-1} \text{ K}^{-2}$, respectively.^[161] Advances have since been made by utilizing molecular dopants such as acids, solvents, and ionic liquids to tune the power factor.^[160,162] Other methods to improve power factor include forming nanocomposites with highly conductive fillers such as silver nanowires, graphene nanorods, and carbon nanotubes whereby electrical conductivities of $\approx 800\text{--}1000 \text{ S cm}^{-1}$ are routinely obtained by various research groups.^[163–165] A two-step methanol and H_2SO_4 treatment under thermal stress were shown to yield higher conductivities in PEDOT:PSS as exhibited in a record high 4600 S cm^{-1} in a paper by Norfolk et al.^[166] Reducing agents like NaBH_4 , OH^- , NH_3 etc. have been also been employed to tune the Seebeck coefficient of polymers such as PEDOT:PSS^[167] and polyaniline (PANI)^[168] composites through reducing the polymer's charge carrier concentration.

Spin coating is one of the most widely employed printing method in organic electronics research, however due to scale up considerations, it is not ideal for processing thermoelectric modules. This is because most spin coating equipment print on substrates in the surface area range of a few millimeters squared,^[169] although larger areas such as 8" Si wafers have been used with spin coating.^[170] When fabricating modules,

a printing method that delivers potential for large area device production is more ideal. To this end, the focus of this section will expand on printing techniques such as screen printing, inkjet, drop casting and other methods with greater scalability.^[120,171,172]

PEDOT:PSS has emerged as one of the more successful inks in formulating organic thermoelectric generators.^[126] It is, however, difficult to find fully PEDOT:PSS TEG modules in literature due to challenges fabricating stable n-type legs to complement the widely available p-type version. This is because when a carbon-based material (such as p-type SWCNTs) is doped via an electron injection from the HOMO of the donor (reducing agent) to the LUMO of acceptor (p-type SWNT), n-type characteristics are introduced (depending on the treatment conditions).^[126] These n-type characteristics are normally instantly lost in PEDOT:PSS, as the polymer is readily oxidized. In the case for PEDOT:PSS it is rare for PEDOT:PSS films to be turned n-type without compositing with nanoparticles.^[173] When n-type PEDOT is achieved typically low electrical conductivity is observed, due to PEDOT losing hole carriers as they are reduced which are not sufficiently replaced by electron carriers. In the case for SWCNT, however, an increase in the electrical conductivity has been observed when treated with reducing agents.^[174] PEDOT:PSS based TEG modules therefore are usually fabricated by connecting p-type legs in parallel with silver or copper electrodes while in some cases, the PEDOT:PSS is composited with foreign particles like copper chloride to induce n-type characteristics.^[175]

In 2011 Bubnova et al.^[176] synthesized poly (3,4-ethylenedioxythiophene) tosylate (PEDOT-Tos) TEGs via an oxidative polymerization of EDOT (3,4-ethylenedioxythiophene) monomers with a solution of iron (III) tris-p-toluenesulfonate. The choice of PEDOT-Tos as opposed to PEDOT:PSS was due to pristine PEDOT-Tos films reportedly exhibiting significantly higher electrical conductivities ($200\text{--}1000 \text{ S cm}^{-1}$) depending on the polymerization method.^[177] Pristine PEDOT:PSS films, however, tend to exhibit much lower electrical conductivity between 0.5 and 50 S cm^{-1} depending on grade and processing conditions.^[178,179] The difference can be explained due to the tosylate anions being smaller than the much larger insulating polystyrene sulfonate anion thereby leading to fewer cases of charge carrier impedance across thiophene chain.^[176] The as synthesized polymer film had a conductivity of 300 S cm^{-1} , a Seebeck coefficient of $40 \mu\text{V K}^{-1}$ leading to a power factor of $38 \mu\text{W m}^{-1} \text{ K}^{-2}$ at room temperature. When treated with tetrakis (dimethylamino)ethylene (TDAE) reducing agent at different rates (minutes), the as prepared PEDOT-Tos films exhibited a significantly higher Seebeck coefficient while invariably suffering a significant decrease in the electrical conductivity. The trade-off was marked at specific oxidation profiles as determined by the XPS measurements in response to different exposure times to the reducing agent. At 22% oxidation an extremely high power factor of $324 \mu\text{W m}^{-1} \text{ K}^{-2}$ was realized. Employing the 3ω -method for thermal conductivity determination in thin-film materials, a lateral thermal conductivity of $0.37 (\pm 0.07) \text{ W m}^{-1} \text{ K}^{-1}$ was measured. When considering the thermoelectric properties, a record high ZT at the time of 0.25 was calculated. A simple TEG was constructed with a carbon leg and a p-type PEDOT-Tos leg, to make a thermocouple to which a ΔT of

1.5 K was applied across. The printed TEG gave different power outputs depending on the level of oxidation (altered by exposure time to TDAE) in response to different load resistances. The highest power output recorded was 1.13 nW. The decreased power output above an exposure time of 10 minutes is related to the decreased electrical conductivity due to excessive reduction of PEDOT.

The group then synthesized a 54 leg TEG via the inkjet technique. Since PEDOT-Tos is insoluble, the group carried out an in situ polymerization of EDOT and tosylate inside the ink cartridges and used pyridine to slow polymerization enough to allow for an appropriate ink dispensation. Due to not having an n-type PEDOT-Tos, tetrathiafulvalene-tetracyanoquinodimethane (TTF-TCNQ) blended with polyvinyl chloride (PVC) was used for the n-type leg which exhibited a Seebeck coefficient of $-48 \mu\text{V K}^{-1}$. At the highest ΔT of 10 K the device gave a maximum power output of 23 nW cm^{-2} .

In 2012 Bubnova et al.^[180] utilized an organic electrochemical transistor (OECT) to tune the thermoelectric properties of PEDOT:PSS. An inkjet printer was employed to pattern the TEG to allow a voltage gate channel. Increasing the voltage was corresponded with an increased Seebeck coefficient. At 1.3 V a high Seebeck coefficient of $400 \mu\text{V K}^{-1}$ was measured. Due to the OECT reducing the oxidation state of PEDOT:PSS at higher voltage however, a retardation of the electrical conductivity was observed. An initially low power factor of $2.3 \mu\text{W m}^{-1} \text{K}^{-2}$ at 0 V was optimized to $23.5 \mu\text{W m}^{-1} \text{K}^{-2}$ at 0.9 V due to a high Seebeck coefficient of around $120 \mu\text{V K}^{-1}$ and electrical conductivity of around 20 S cm^{-1} . A ZT of 0.041 was estimated using the optimized thermoelectric properties and a literature thermal conductivity of $0.17 \text{ W m}^{-1} \text{K}^{-1}$.^[181] Although a way to tune the power factor of a PEDOT:PSS TEG was found, the limit on how high the power factor can be optimized via the redox-based improvements resulted in the relatively low ZT .

Other printing techniques involve simple ink soaking on paper substrates as demonstrated by Jiang et al.^[182] The thermoelectric paper was prepared as shown in **Figure 20a**. The novel substrate produced a film with a very low thermal conductivity of $0.16 \text{ W m}^{-1} \text{K}^{-1}$. To optimize the power factor, the PEDOT:PSS/paper composites were treated with different solvents (DMSO and Ethylene glycol) to form inks with varying concentration of solvent to PEDOT:PSS solution (0, 5, 30, and 50 v/v%). The Seebeck coefficient of the Pristine PEDOT:PSS was $30 \mu\text{V K}^{-1}$ which reduced to $25 \mu\text{V K}^{-1}$ for the optimized 30% v/v PEDOT:PSS-EG film. The electrical conductivity however improved from 0.2 to 50 S cm^{-1} , thus, a power factor of $3.0 \mu\text{W m}^{-1} \text{K}^{-2}$ that led to a ZT of 0.0055. The film printed on paper had several advantages over those printed on glass substrates as the Van der Waals forces between the paper and PEDOT:PSS created a bond that could withstand water damage better than the one printed on glass substrate.

In 2014 Wei et al.^[183] utilized a screen printing technique to create the first flexible PEDOT:PSS module printed on paper for practical applications. They utilized a standard 5% v/v ethylene glycol/PEDOT:PSS treatment that resulted in a power factor of $25 \mu\text{W m}^{-1} \text{K}^{-2}$ at 25°C . This was due to a high electrical conductivity and Seebeck coefficient of 770 S cm^{-1} and $18 \mu\text{V K}^{-1}$ respectively. To show large area application potential, a module with 300 legs was created, which was later used to power an LED.

The module dubbed M2 produced a power of $50 \mu\text{W}$ at a load resistance of less than 10Ω as well as an open circuit voltage of over 40 mV at $\Delta T \approx 100 \text{ K}$. Due to the low voltage, however, a step-up converter was used. The converter required an input voltage of 20 mV to give a 2.2 V at no extra power input leading to an LED being powered. The device suffered stability issues. After 100 hours of usage at above 100°C the device performance halved but the individual legs maintained their performance. It was therefore deduced that it may have been an interface-related degradation. This was confirmed by XPS showing PSS segregation at the interfacial layer thereby creating a larger surface area at the contact with the insulating component. Part of the reason why a higher power output was not achieved was due to not having an optimized device design and not having n-type counter legs. In addition, the interfacial instability would need to be solved. Therefore, to maximize power generation one would need to find a conductive paste that does not react with PEDOT or PSS. Thicker films than the $20 \mu\text{m}$ films produced in this work would ideally also need to be produced, issues surround thicker pastes in that the electrical conductivity is reduced. In the same year Wei et al.^[184] used the same printing method to print a module with 11 legs. In this case after an experiment that showed an apparent increased Seebeck coefficient with increased humidity, the modules power output was tested while spraying it with water. The films power factor improved from 23 to $225 \pm 130 \mu\text{W m}^{-1} \text{K}^{-2}$ from 30 to 90% humidity mostly due to its increases in Seebeck coefficient from 17 to $>49 \mu\text{V K}^{-1}$ and a minor increase in electrical conductivity (805 to 870 S cm^{-1}).

The issue commonly observed with screen printing surrounds the requirement for high viscosity inks in which thermoelectric properties alter significantly, as well as the requirement for posttreatments to try off-set the loss in electrical conductivity. In 2016, Zhang et al.^[127] created a TEG utilizing flexographic printing in a roll to roll (R2R) setup whereby PEDOT:PSS was utilized as the p-type component and a nitrogen-doped graphene for the n-type component. A maximum voltage of 3 mV and a power output of 0.24 mW m^{-2} was obtained at a ΔT of 10 K. **Figure 20b** represents the printing method employed. The procedure involved 3 cylinders dipped in the appropriate ink and applied sequentially to a substrate as shown in **Figure 20bi**. **Figure 20bii,iii** on the other hand depicts the importance of controlling surface energy of the interface between the ink and substrate. To determine wettability the UV treated plastic substrate was compared to that of the plasma treated one. In appearance and surface coverage of ink and performance, it appeared that the plasma-treated substrate was more effective (**Figure 20biii**). For large-scale continuous printing, a R2R system would be more ideal as it is not as sensitive to viscosity as inkjet printing, however challenges remain on improving wettability of substrates as well as finding stable n-type components with high thermoelectric power factor.

A 36 leg thermoelectric generator with thermoelectric voltage output of 36 mV at a ΔT of 7.9 K and power output of 115 nW (160 nW at a ΔT of 10 K) was created by Park et al.^[185] via solution casting polymerization. PEDOT-Tos was utilized as the p-type component meanwhile Bi_2Te_3 was utilized as the n-type blocks connected to a PET flexible substrate. The TEG exhibited higher power output with temperature as well as great stability

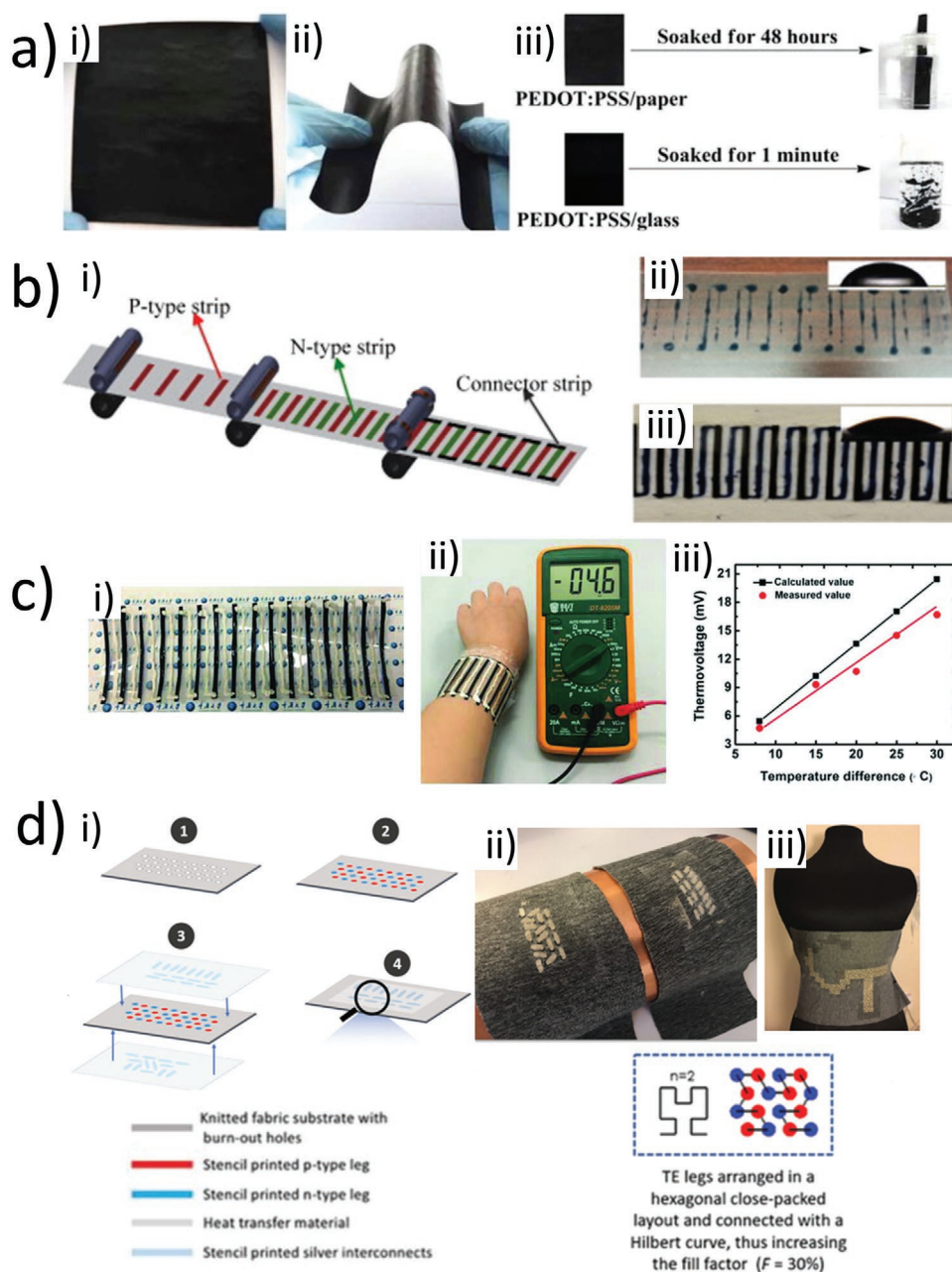


Figure 20. A selection of PEDOT:PSS based printed thermoelectrics. a) PEDOT:PSS soaking on paper: i,ii) The flexibility of freestanding PEDOT:PSS/paper composite films, iii) The soaking stability in water. Reproduced with permission.^[182] Copyright 2014, Wiley. b) Roll to roll (R2R) printing a PEDOT:PSS module: i) Illustration of R2R printing of flexible thermoelectric devices; ii) UV treated plastic substrate and iii) plasma-treated plastic substrate. The inset images show the contact angle between substrate and the inks. Reproduced with permission.^[127] Copyright 2016, Elsevier. c) Painted PEDOT:PSS/silver thermoelectric module: i) Image of the flexible and twistable TEG comprising 16 legs, ii) generation of thermovoltage by the TEG attached on the forearm at room temperature of 25 °C, iii) dependence of calculated and measured thermovoltage values with temperature differences. Reproduced with permission.^[186] Copyright 2018, Wiley. d) PEDOT:PSS/Poly[Na(NiETT)] embedded textile thermoelectric module. i) Step-by-step device fabrication and assembly process for a textile-integrated TEG: 1) Burning out holes through the knitted fabric, 2) Stencil printing p-type (red) and n-type (blue) material on both sides of the fabric to fill the holes, 3) Stencil printing silver interconnects (light blue) on a heat transfer membrane (light gray) for both sides of the device, and 4) Transfer printing interconnects by heat pressing the heat transfer membrane on both sides of the device. ii) Wearable TEG integrated into knitted fabric consisting of 32 p- and n-type legs arranged in a hexagonal close-packed layout and connected according to the Hilbert curve. iii) device consisting of 1072 polymer TE legs deposited on a 25 cm x 25 cm area of knitted fabric. Reproduced with permission.^[123] Copyright 2019, Wiley.

whereby the resistance did not increase by a significant factor even after 120 d. Furthermore, the group showed this TEG

fabrication procedure coupled with the conducting polymer (PEDOT-Tos) and inorganic block (Bi_2Te_3) to be stable upon

(bending) up to several cycles up to a curvature of 4 cm without significant increase in the resistivity.^[185]

A year later in 2018 Wang et al.^[186] used a redox doping strategy to achieve a power factor in PEDOT:PSS of $203.1 \mu\text{W m}^{-1} \text{K}^{-2}$ at room temperature. The optimized power factor was due to BSA (benzene sulfonic acid) addition to the PEDOT:PSS solution to improve conductivity from $<50 \text{ S cm}^{-1}$ to 1996 S cm^{-1} . The effects of treating PEDOT:PSS solutions with sulfonic acid derivatives (differing in molecular size/functional groups) were studied, resulting in the discovery that steric effects may be responsible for the observed difference in electrical conductivity measured. As the acid protonates the PSS-anion to PSSH, this reduces the coulombic interaction with PEDOT. This in turn allows PSSH to be selectively removed from the PEDOT:PSS increasing the carrier mobility, as was determined by Hall effect measurements. Generally, the study showed that the largest molecule the CSA (camphor sulfonic acid) had the lowest electrical conductivity (580 S cm^{-1}) meanwhile the smaller molecules had higher electrical conductivity $>1940 \text{ S cm}^{-1}$. A wearable TEG was formed by connecting 16 crudely printed legs in parallel. There was no n-type leg, therefore, silver paste was used to connect the p-type legs as shown in Figure 20c. Due to interfacial contact resistance however, there was a difference between the theoretical thermoelectric voltage of 5.6 mV and measured output of 4.6 mV at a ΔT of 8 K (human skin to outside environment). The wearable TEG showed potential to generate more power during winter times.

In 2018 a record high power output for a purely organic TEG was recorded as $99 \mu\text{W cm}^{-2}$ at a ΔT of 29 K.^[187] The optimized Seebeck coefficient and electrical conductivity were $20.6 \mu\text{V K}^{-1}$ and 2500 S cm^{-1} respectively, leading to a room temperature power factor of $107 \mu\text{W m}^{-1} \text{K}^{-2}$. The thermal conductivity was recorded as $0.64 \text{ W m}^{-1} \text{K}^{-1}$ at room temperature, resulting in a modest ZT of 0.05. A facile freestanding film technique developed by the same authors previously was utilized.^[188] The printing method (casting), whereby PEDOT:PSS particles were dispersed in strong acid and a subsequent vacuum-assisted filtering was conducted, produced highly uniform PEDOT:PSS freestanding films that could be cut into required shape (legs). As indicated by XRD and Raman, the films produced a highly ordered PEDOT (π - π) stacking that contributed to the extremely high electrical conductivity. The TEGs were stable up to $250 \text{ }^\circ\text{C}$, thereby showing promise for varied application. The interesting printing method allows for controlling larger PEDOT particles, leading to higher power factor and thus power output. The facile method allows several stacks of freestanding films to be potentially folded to scale up an organic TEG, a weakness in the design strategies for organic TEGs. The issue with R2R and ink-jet based systems is maintaining a high temperature gradient due to thin films obtained. The study showed progress and potential applications for more diverse TEG designs.

To test the effectiveness of printed organic printed TEGs on different paper as opposed to a plastic substrate like PET (polyethylene terephthalate), Andersson et al. used PEDOT:PSS and Ag inks to power an electronic circuit on paper.^[119] In general, the films had a low power factors, with $1.3 \mu\text{W m}^{-1} \text{K}^{-2}$ for the TEG printed on PET, and $0.8 \mu\text{W m}^{-1} \text{K}^{-2}$ and $0.9 \mu\text{W m}^{-1} \text{K}^{-2}$ on photo paper and cardboard respectively. The purpose of the experiment, however, was to determine optimum

substrate conditions. In this respect, the PET substrate had the most homogeneously spread film with the lowest roughness, meanwhile the cardboard had the highest surface roughness in which the film thickness was more varied. The paper surfaces were porous, PET was not, which may explain the higher electrical conductivity achieved by PET as there were fewer impedance of carrier mobility by insulating paper fibers. The carbon paper and PET TEGs had a thermovoltage of 0.4 mV at ΔT 15 K, the photopaper 0.3 mV. There was a slight variation in the Seebeck coefficients, PET and carbon paper had $25.5 \mu\text{V K}^{-1}$, photopaper had $21.5 \mu\text{V K}^{-1}$. The most notable difference, however, was the resistance. Carbon paper had the highest resistance at 760Ω , while the smoother photopaper and PET substrates produced lower resistances of 380 and 390Ω , respectively. The Ag resistance did not vary significantly, showing the contact resistance between silver and PEDOT was relatively similar for all substrates. More post or pre-printing PEDOT:PSS optimization via acid treatments, ionic liquids, reducing agents, or a mixture would be required to explore higher power factors.

More developments by Khoso et al.^[189] in 2019 showed that by systematically altering the PEDOT to oxidant (FeCl_3) ratio in the polymerization of the monomer EDOT in the ratios 1:3, 1:6, and 1:9 would lead to PEDOT nanowires, nanotubes, and nanocubes of different shapes and sizes. As shown by other studies where control of size and shape may contribute to thermoelectric properties of organic TEGs.^[187,190–192] Khoso et al.^[189] showed that, as the proportion of PEDOT lowered the nanosphere became nanocubes and the original size of 50–200 nm range became 50–300 nm. As the ratio reached 1:9 the cubes became less homogenous. The as prepared PEDOT coated textiles had relatively low thermoelectric properties with electrical conductivity, Seebeck coefficient, and thermal conductivity at 309 K of 16.67 S cm^{-1} , $4.0 \mu\text{V K}^{-1}$ and $0.009 \text{ W m}^{-1} \text{K}^{-1}$ respectively. This corresponds to a power factor and ZT of $0.027 \mu\text{W m}^{-1} \text{K}^{-2}$ and 0.0009 respectively. When the mostly nanocube PEDOT textile TEG was fabricated, however, the device had a significantly improved performance with an electrical conductivity of 560 S cm^{-1} and thermovoltage 19.5 mV thus showing potential for human body heat waste recovery. Although some limitations in the studies method are the creation of the nanospheres and nanocubes in which it would create extra steps for large-scale formulations. As printed TEGs have untapped potential in wearable electronics, new methods to make films that are mechanically resistant in response to several bends folds and repeated thermal cycling would yield more commercialized products. Looking into the unique abilities of ionic liquids to imbed into polymers like PEDOT:PSS, not only to improve the conductivity as high as 1439 S cm^{-1} , but depending on the ionic or anionic counterpart they can act as the reducing agent too to improve Seebeck and electrical conductivity simultaneously.^[163,193] The unique properties of ionic liquids may have greater potential in printing technologies as they can increase the viscosity of PEDOT:PSS solutions, creating thicker materials with higher conductance.^[194]

Elmoughni et al.^[123] synthesized a 32 leg PEDOT:PSS and poly[Na(NiETT)] imbedded textile TEG (Figure 20d) giving rise to an open circuit voltage (3 mV) at ΔT 3K (natural convection) and later scaled up to 864 legs in which the thermovoltage was

recorded as 47 mV at the same ΔT . The study is the first in synthesizing a fully organic p- and n-type textile TEG. To achieve skin contact, where the thermal gradient is maximized, hexagonal holes were burned in a commercial fabric and a stencil printing technique employed to print p and n legs with a design to maximize fill factor yet allowing for flexibility of fabric. Cracks were discovered on the textile surface as inks dried due to mechanical folds. For the 32 leg device, at a doubled ΔT of 6 K, an open circuit voltage of <6 mV was observed. If a similar relationship with ΔT for the 864-leg device with correction for contact issues was seen, one would potentially have a thermovoltage of over >84 mV. This device shows promise for self-heated clothing as well as power for microelectronic devices, especially for winter applications as the thermal gradient may be higher due to body heat of 37 °C and outside environment of potentially <0 °C.

Xu et al. fabricated a PEDOT:PSS TEG by drop casting, which they powered with the heat from a human arm. PEDOT:PSS was optimized with triple postcasting treatments of CH_3NO followed by H_2SO_4 and NaBH_4 .^[195] The acid treatments improved the carrier mobility by removing the insulating PSS anions from the polymer meanwhile the reducing agent treatment was optimized to tune the oxidation state of the polythiophene molecules by reducing carrier concentration. Following sequences of treatments at varying temperatures and concentrations of (NaBH_4) the TEG produced a power density of $1 \mu\text{W cm}^{-2}$ and a thermovoltage of 2.9 mV at a ΔT of 12 K. A Seebeck coefficient of $28.1 \mu\text{V K}^{-1}$ and an electrical conductivity of 1786 S cm^{-1} and power factor of $141 \mu\text{W m}^{-1} \text{ K}^{-2}$ were determined for the optimized film. After the H_2SO_4 treatment following the initial CH_3NO treatment, the carrier concentration increased from (1.1 to $1.35 \times 10^{21} \text{ cm}^{-3}$) probably due to increased H^+ ions from the acids dissociating to the polymer. After the NaBH_4 treatment, however, the carrier concentration halved as expected with a corresponding decreased electrical conductivity. The carrier mobility, however, did not decrease significantly. A favorable treatment condition to mitigate the thermoelectric trade-off (S to σ) was discovered. **Figure 21a** reveals that the TEG did not contain an n-type alternative which remains an issue in the development of an all organic TEG, as PEDOT:PSS p-type shows promise. The p-type legs were $2 \times 0.35 \text{ cm}^2$. The facile free-standing films have the potential to be cut into appropriate shapes or increase thickness. Challenges lie, however, in large-scale reproducibility using current printing technologies. Increasing the container the films are created in and post-processed, could also increase the size of the TEGs.

In 2020 Yvenou et al,^[196] used an ExactCoat Benchtop Ultrasonic Spraying System to print a poly(3,4-ethylenedioxythiophene), fluoromethanesulfonate (PEDOT:OTf) thermoelectric composite. This was achieved via an in situ oxidative polymerization of EDOT and iron(III) trifluoromethanesulfonate (FeOTf_3). The printing technique allows for large area deposition of the polymer film with some control of thickness depending on the time and angle of spraying or viscosity of the solution which may depend on concentration of additives such as cosolvents. The study found that N-methyl-2-pyrrolidone (NMP) improved the electrical conductivity as reported in other studies. In general, increasing the NMP concentration

lowered the resulting thin film's thickness, dropping from 800 nm with no NMP to $\approx 50 \text{ nm}$ at 6% NMP. There is a clear dependence of NMP concentration and the resulting electrical conductivity, with electrical conductivity increasing up to 5 wt%, until it decreases drastically at 6 wt%. No clear dependence for the Seebeck coefficient was seen. 5 wt% NMP obtained maximum electrical conductivity of $2215 (\pm 665) \text{ S cm}^{-1}$, with a film thickness of 132 nm thickness, a Seebeck coefficient of $\approx 22 \mu\text{V K}^{-1}$ and a corresponding power factor of $\approx 107 \mu\text{W m}^{-1} \text{ K}^{-2}$. The improved conductivity via polymerization with NMP was attributed to slower polymerization rate with more crystalline packing of polymers.^[197]

The printed TEG shown in **Figure 21b** was fabricated utilizing the optimized 5 wt% NMP. 156 p-type spray printed PEDOT:OTf legs were printed with 156 silver electrodes thereby making a total of 312 legs on a $25 \mu\text{m}$ polyimide foil. A stack was made with four printed polymer films to increase film thickness, whereby one stack is 132 nm and the four stack is 650 nm. This was done to improve the temperature difference between the hot and cold sides. **Figure 21bii** shows the rolled TEG fabricated by rolling up the LEGs printed on the polyamide foil and connecting them at each end with silver electrode. Nine thermocouples of the polymer silver TEG were cut off as shown in **Figure 21bi** to be used for power density measurements.

Nine thermocouples had a surface area of 15.12 cm^2 ; each thermocouple had a mean surface area of around 1.68 cm^2 . When a load resistance of 167.4Ω is applied the surface area power density is 16.5 nW m^{-2} . When the TEG was exposed to a ΔT of 48.1 K, a $1 \mu\text{W}$ power output was observed. This result is similar to other PEDOT-based screen printed thermoelectrics and the researchers showed potential for controlling crystallinity of films through the concentration of NMP during polymerization. It is also interesting that the researchers were able to fabricate a 3D TEG by rolling up the thermocouples, allowing for the devices to curve to match the heat source. The printing method also allows for a scalable approach to fabricating TEGs. In keeping with other organic TEG development, development of an n-type counter leg is needed to improve power output; silver as a proxy for the n-type leg yields near 0 positive Seebeck voltage.

Rösch et al. used an origami approach to make a device with a substantial number of thermocouples.^[198] They used PEDOT:PSS nanowires as the p-type material, while the n-type was a TiS_2 :Hexylamine-complex. A screen-printing machine was used to semiautomate the manufacturing process of the TEGs. In order to maintain minimal heat conduction through the substrate a $6 \mu\text{m}$ thin substrate foil of PEN was used, to which the $7 \mu\text{m}$ thick layers of the p- and n-type materials were printed. The p-type PEDOT:PSS nanowires ZT was estimated using a literature value of the thermal conductivity to be 0.062 at 300 K ($\sigma = 900 \text{ S cm}^{-1}$, $S = 25.6 \mu\text{V K}^{-1}$, $\kappa = 0.286 \text{ W m}^{-1} \text{ K}^{-1}$), while the n-type TiS_2 :hexylamine-complex ZT was 0.22 at 300 K ($\sigma = 544 \text{ S cm}^{-1}$, $S = -96.6 \mu\text{V K}^{-1}$, $\kappa = 0.69 \text{ W m}^{-1} \text{ K}^{-1}$) again estimated using a literature value of the thermal conductivity. The thermoelectric materials were printed in an alternating (checkerboard) fashion (**Figure 21ci**) on a single substrate, this then underwent two folding steps (one along each axis, **Figure 21ii-v**) to produce a vertically standing compact device (**Figure 21cvi**). The performance of the device was investigated

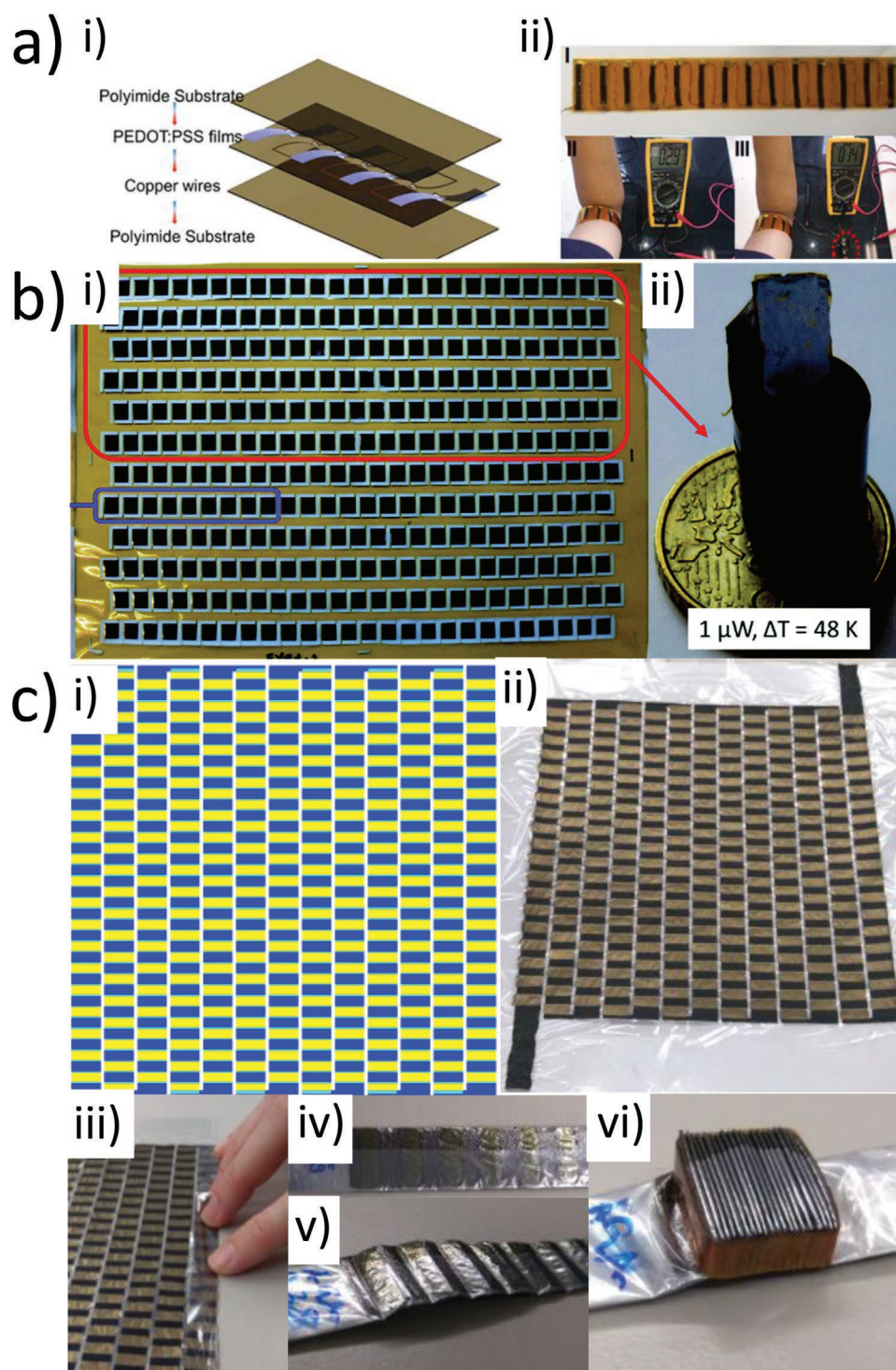


Figure 21. A selection of PEDOT:PSS based printed thermoelectrics. a) PEDOT:PSS dropcast module: i) Schematic diagram of the homemade flexible thermoelectric device, ii) Photograph of the homemade device (I), measurement setup for the open-circuit thermovoltage (II), and measurement setup for voltage on an external resistor framed by the red dot cycle (III). Reproduced with permission.^[195] Copyright 2019 ACS. b) Spray printed PEDOT:OTf thermoelectric composite: i) picture of 312 spray-coated legs on a 25 μm thick polyimide foil, ii) 3D TEG composed of 156 linked and rolled thermocouples ($R = 2.9 \text{ K}\Omega$). Reproduced with permission.^[196] Copyright 2020, RSC. c) Origami screen printed PEDOT:PSS/TiS₂:hexylamine-complex module: i) 2D print layout for an origami TEG with 254 p-legs (blue) and 253 n-legs (yellow), ii) screen printed TEG, iii) first folding step stacking all columns plus one extra strip of substrate, iv) fully folded thermoelectric ribbon, v) thermoelectric ribbon creased at the fold lines, vi) fully folded thermoelectric generator fixed with a Kapton ribbon. Reproduced under terms of an Attribution 4.0 International (CC BY 4.0) license.^[198] Copyright 2021, The Authors. Published by Springer Nature.

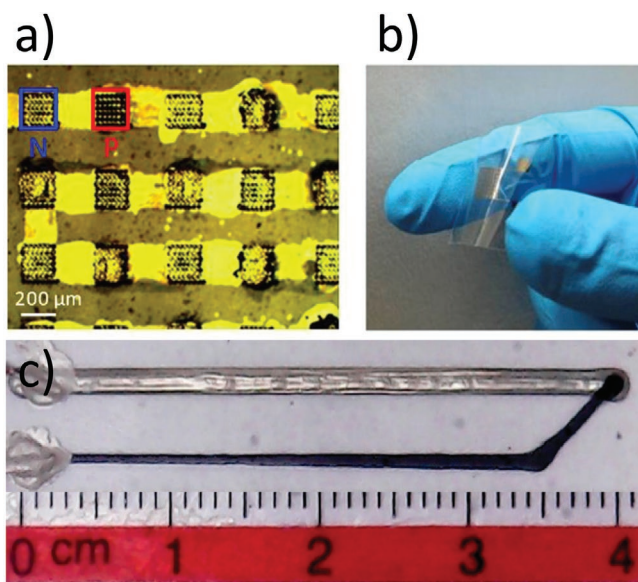


Figure 22. a) optical microscope image and b) photograph of μ -OTEG consisting of PEDOT:PSS and PTEG-1. Reproduced with permission.^[199] Copyright 2020, Elsevier. c) Photograph of a dispenser printed μ -OTEG using PEDOT:PSS, with silver used to complete the circuit. Reproduced with permission.^[200] Copyright 2021, Elsevier.

which was shown to have a power output of $63.4 \mu\text{W}$ at a ΔT of 30 K which increased to $\approx 240 \mu\text{W}$ at a ΔT of 60 K.

The aforementioned organic work looks into macrothermoelectric generators, however, there have been recent developments in the printing of organic microthermoelectric generators (μ -OTEG). In 2020 Massetti et al.^[199] inkjet printed into laser etched cone-shaped cavities (top diameter $20 \mu\text{m}$, bottom diameter $6 \mu\text{m}$) in $25 \mu\text{m}$ thick polyethylene naphthalate (PEN). PEDOT:PSS was used as the p-type material, while PTEG-1 (a [60]fulleropyrrolidine, with an additional polar triethylene glycol ether side chain) was used as the n-type material. The devices were cured overnight at 393 K in a N_2 atmosphere, then capped with a poly(methyl methacrylate) layer. No thermoelectric properties of the materials were characterized. As can be seen in Figure 22a, the devices used an array of microcavities for each p- and n-type leg, this avoided the issue of a single misprinted micro-leg breaking the circuit of the device (Figure 22b). A maximum power density of 30.5 nW cm^{-2} was observed at a ΔT of 25 K.

In 2021, Shakeel et al.^[200] fabricated a p-type only microthermoelectric generator by dispenser printing PEDOT:PSS onto glass. The samples were cured at 413 K for 30 min post-printing. The thickness of the printed samples was not specified. The electrical conductivity was seen to be 5.85 S cm^{-1} , the Seebeck coefficient $17 \mu\text{V K}^{-1}$, and the power factor $0.17 \mu\text{W m}^{-1} \text{ K}^{-1}$. The device (Figure 22c) yielded a power output of 5.17 nW at a ΔT of 120 K.

4.3. Printed Organic n-Type Thermoelectric Polymers

Due to oxidation, forming stable n-type polymers is challenging, especially under printing conditions. There are examples in the

literature, however. Organometallic polymers are widely used to form n-type polymers. In 2014, Jiao et al.^[201] inkjet-printed poly(metal 1,1,2,2-ethenetetrathiolate(ett)s/polymer composites to produce both p- and n-type materials. The n- and p-type organometallic coordination polymers (poly[$\text{K}_x(\text{Ni-ett})$] and poly[$\text{Cu}_x(\text{Cu-ett})$] respectively) were insoluble, so were ball milled with polymer solutions to make them solution processable. To characterize the thermoelectric properties, samples were cast onto glass substrates, followed by drying in a vacuum at 383 K for 10 h. Devices were made by inkjet printing $2\text{--}5 \mu\text{m}$ thick composite films onto PET, and drying the samples at 363 K for 10 h. The optimal power factors were found when the organometallic polymers were mixed with PVDF in a 1:2 ratio, with NMP being used with the n-type and DMSO being used with the p-type. The maximum n-type power factor was $1.6 \mu\text{W m}^{-1} \text{ K}^{-2}$ at 400 K ($\sigma = 5 \text{ S cm}^{-1}$, $S = -57 \mu\text{V K}^{-1}$) and again $1.6 \mu\text{W m}^{-1} \text{ K}^{-2}$ at 400 K for the p-type ($\sigma = 5.7 \text{ S cm}^{-1}$, $S = 53 \mu\text{V K}^{-1}$). A six thermocouple inkjet printed thermoelectric generator was shown to produce a output voltage and short-circuit current of $\approx 15 \text{ mV}$ and $\approx 3 \mu\text{A}$ respectively with a ΔT of 25 K. A maximum power output of 45 nW was observed, which was noted to be low due to the large contact resistance between the device's gold electrodes and the thermoelectric materials.

In 2016 Menon et al.^[202] also relied on organometallic polymers to print an n-type material, using poly(Ni-ett) blended with PVDF/DMSO. PEDOT:PSS with tellurium nanowires was used as the p-type material. The samples were printed using calligraphy to both sides of an $80 \mu\text{m}$ thick paper substrate. The samples were then dried at 333 K for 30 min. The p-type power factor was $0.021 \mu\text{W m}^{-1} \text{ K}^{-2}$ at 295 K ($\sigma = 0.0049 \text{ S cm}^{-1}$, $S = 204.1 \mu\text{V K}^{-1}$) and $0.041 \mu\text{W m}^{-1} \text{ K}^{-2}$ at 295 K for the p-type ($\sigma = 0.5 \text{ S cm}^{-1}$, $S = -28.3 \mu\text{V K}^{-1}$). A radial design was used to make a thermoelectric generator which consisted of 15 thermocouples producing 15 nW cm^{-2} at a ΔT of 45 K with a voltage of up to 85 mV being measured.

In 2021 Yang et al.^[203] reported on a printable n-type polymer poly(benzimidazobenzophenanthroline):poly(ethyleneimine) (BBL:PEI) as an ethanol based n-type conductive ink. $10 \mu\text{m}$ films were spray coated on a PEN substrate in air then annealed at 413 K in a nitrogen atmosphere before being encapsulated in CYTOP. To make a device PEDOT:PSS was used as the p-type material and was processed under the same conditions. While power factors are not explicitly reported, the peak electrical conductivity of BBL:PEI is shown to be 8 S cm^{-1} and is when the weight ratio between BBL and PEI is 1:1. At this concentration, a Seebeck coefficient of $\approx 120 \mu\text{V K}^{-1}$ is reported that correlates to a power factor of $11.5 \mu\text{W m}^{-1} \text{ K}^{-2}$. The device consisting of a single thermocouple produced a power output of 56 nW at a ΔT of 50 K.

4.4. Organic Based Nanocomposite TEGs

Bae et al.^[204] synthesized Te-Bi₂Te₃ nano-barbell structures coated with PEDOT:PSS via a low-temperature solution reaction. Utilizing a spray-printing process, the solution was deposited on a flexible polyimide substrate. Different acid concentrations were used to treat the films to improve their performance. Higher H_2SO_4 concentrations led to higher

electrical conductivity and lower Seebeck coefficient. At 80% H_2SO_4 concentration, the electrical conductivity was 70 S cm^{-1} , the Seebeck coefficient $94 \mu\text{V K}^{-1}$, and the power factor $60 \mu\text{W m}^{-1} \text{K}^{-2}$. Despite the loss in the Seebeck coefficient, the power factor was higher than the untreated film due to the significant increase in conductivity. A p- only type TEG device was made using a shadow mask to make several sprayed p-type $\text{Te-Bi}_2\text{Te}_3$ PEDOT:PSS composite legs, which were then connected hot side to cold side with printed silver electrodes. There was a strong positive correlation between the ΔV and the number of legs at any specific ΔT . 6 legs had an open-circuit voltage of 1.54 mV at ΔT of 10 K.

Ou et al. synthesized Bi_2Te_3 nanoparticles and Sb_2Te_3 nanoflakes via a solvothermal process.^[205] Different concentrations of each material were then mixed with a PEDOT:PSS solution with a 5% ethylene glycol internal treatment to form two types of composites. A linear incremental relationship between the power factor and temperature was observed for both materials. The 15% w/w Bi_2Te_3 -PEDOT:PSS and the 50% w/w Sb_2Te_3 -PEDOT:PSS TEG had an optimal power factor of $\approx 50 \mu\text{W m}^{-1} \text{K}^{-2}$ at 362 K. An aerosol jet printer was utilized to print one leg of each material on a substrate. An external load resistance of 50Ω at a 70 K ΔT was applied to the printed materials. The 15% w/w Bi_2Te_3 -PEDOT:PSS composite had a power output of 13 nW and a power area density of $100 \mu\text{W cm}^{-2}$, meanwhile the power output for the 15% w/w Sb_2Te_3 -PEDOT:PSS was 10 nW. Employing an AutoCAD design and the same printing procedure, 20 legs comprising of both materials type were fabricated on a polyimide substrate. The legs were connected electrically in series and thermally in parallel by silver electrodes. The open-circuit voltage was 12.5 mV, the short current was $11.3 \mu\text{A}$, and the maximum power of 141 nW at a ΔT of 50 K. The module shows potential for application in wearable devices and medium temperature heat recovery such as hot water pipes after some optimization.

Ferhat et al. inserted PEDOT within nanotemplates of vanadium pentoxide gel ($\text{V}_2\text{O}_5 \cdot n\text{H}_2\text{O}$) to enhance the carrier concentration.^[206] This was achieved by dissolving V_2O_5 in a 30% H_2O_2 water solution and stirred for several days, EDOT was then added dropwise to form the viscous solution. The solution was then diluted further in water to achieve a reduced viscosity from around 30 to 5 mPa s. An optimized molar ratio of EDOT to V_2O_5 was found at 0.03:1 to account for trade-offs between Seebeck coefficient and electrical conductivity. To reduce the high surface tension of 71 mN m^{-1} to an optimized 31 mN m^{-1} , 0.6% vol/vol of Triton X-100 surfactant was introduced to the $(\text{PEDOT})_{0.03}\text{V}_2\text{O}_5$ ink. This is because if the surface tension is too high it compromises the jetting of the ink, meanwhile if the surface tension is too low the nozzle does not hold the ink. The ink was printed on photo paper via a DIMATIX DMP-381 multimaterial inkjet printer. A large negative Seebeck coefficient of $-350 \mu\text{V K}^{-1}$, an electrical conductivity of 0.16 S cm^{-1} , and a power factor of $2 \mu\text{W m}^{-1} \text{K}^{-2}$ was recorded. A thermal conductivity of $0.68 \text{ W m}^{-1} \text{K}^{-1}$ was measured resulting in a reported ZT of 1×10^{-3} . In comparison the p-type PEDOT:PSS had a Seebeck coefficient of $17 \mu\text{V K}^{-1}$, an electrical conductivity of 600 S cm^{-1} , a power factor of $17 \mu\text{W m}^{-1} \text{K}^{-2}$, a thermal conductivity of $0.34 \text{ W m}^{-1} \text{K}^{-1}$, and ZT of 1.3×10^{-2} at room temperature. For the module (Figure 23a), an optimal leg length

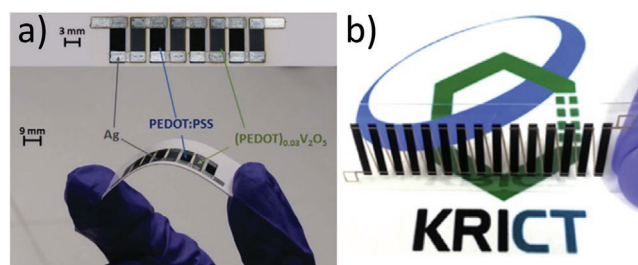


Figure 23. Photographs of organic based nanocomposite thermoelectric modules. a) PEDOT within nanotemplates of vanadium pentoxide gel. Reproduced with permission.^[206] Copyright 2018, RSC. b) P3HT/DWCNT composite. Reproduced with permission.^[207] Copyright 2017, Elsevier.

of 5 mm, width of 3 mm, and leg thickness of $4 \mu\text{m}$ was selected after accounting for the trade off between maintaining a high ΔT and low internal resistance in the flexible substrate. At a ΔT of 20 K and load resistance of $515 \text{ K}\Omega$ a maximum power output of 0.34 nW was seen when 4 legs are connected. This led to an area power density of $0.266 \mu\text{W cm}^{-2}$. The study expressed progress in hybrid organic-inorganic n-type thermoelectrics, as evidenced by the $(\text{PEDOT})_{0.03}\text{V}_2\text{O}_5$ composite maintaining n-type character for over 6 months. Although the synthesis process required several steps and days, the process was relatively simple. The low electrical conductivity of the material and the low power factor observed, mean the material requires further research. Optimizing the electrical conductivity of the n-type material would be a step towards commercialization, as printing using ink jet devices has the potential for large area printing.

In a study by An et al.,^[207] poly(3-hexylthiophene-2,5-diyl) (P3HT) was mixed with double-walled carbon nanotube (DWCNT) to form a P3HT/DWCNT composite. The resultant Seebeck coefficient, electrical conductivity, and power factor were $69.2 \mu\text{V K}^{-1}$, 80 S cm^{-1} , and $40 \mu\text{W m}^{-1} \text{K}^{-2}$, respectively, at room temperature. A different composite was synthesized through a chemical bond between an amino terminated P3HT and functionalized DWCNT to form the long and short P3HT-g-DWCNT composites. The short P3HT-g-DWCNT film outperformed the long P3HT-g-DWCNT. The P3HT-g-DWCNT composites had lower amount of DWCNT aggregation than in the P3HT/DWCNT mixture, thus leading to better solubility. The Seebeck coefficient in the P3HT-g-DWCNT composites was significantly higher than the P3HT/DWCNT mixture at $116.6 \mu\text{V K}^{-1}$, meanwhile the electrical conductivity decreased slightly to 38 S cm^{-1} leading to a power factor of $\approx 50 \mu\text{W m}^{-1} \text{K}^{-2}$. The measured thermal conductivity for the P3HT-g-DWCNT was $2 \text{ W m}^{-1} \text{K}^{-1}$. The pristine DWCNT had a thermal conductivity of $3.5 \text{ W m}^{-1} \text{K}^{-1}$. In comparison, the mixed P3HT/DWCNT was lower with a thermal conductivity of $3 \text{ W m}^{-1} \text{K}^{-1}$. This showed that compositing DWCNTs inside the polymer reduced thermal conductivity, chemically grafted DWCNT as exhibited in the P3HT-g-DWCNT gave a material with an even lower thermal conductivity. The ZT for the pristine DWCNT was <0.0038 , the short P3HT-g-DWCNT 0.0068, the mixed P3HT/DWCNT 0.0045. A Flexible TEG (Figure 23b) was synthesized via a dispenser printer utilizing the p-type P3HT-g-DWCNT to form 15 legs at 2 mm widths and 15 mm lengths connected by silver electrodes. At a ΔT of 20 K, the optimal power output was 14.5 nW, at a load resistance of $\approx 18.2 \text{ K}\Omega$.

Jang et al. utilized a simple drop casted printing method to prepare a Sb_2Te_3 -P3HT composite thermoelectric material.^[208] The material was composed of a 2,3,5,6-tetrafluoro-7,7,8,8-tetracyanoquinodimethane (F4TCNQ) doped P3HT polymer mixed with varying amounts of Sb_2Te_3 . To determine the effect of F4TCNQ, varying concentrations of the dopant were mixed with P3HT. The electrical conductivity could be improved from $1 \times 10^{-7} \text{ S cm}^{-1}$ for the pristine P3HT film to 1.6 S cm^{-1} for the 17% F4TCNQ film. A corresponding Seebeck coefficient of $100 \mu\text{V K}^{-1}$ was observed, resulting in a power factor of $1.6 \mu\text{W m}^{-1} \text{ K}^{-2}$ at room temperature. The Sb_2Te_3 -P3HT-F4TCNQ composite however had an inferior power factor compared to the film without Sb_2Te_3 . This is because the conductivity was significantly lower when the inorganic compound was composited with the polymer. 17% F4TCNQ doped P3HT with 98% wt Sb_2Te_3 gave the highest thermoelectric performance relative to other % wt Sb_2Te_3 loading. The reduced conductivity was attributed to greater phase separation between the constituents of the composite at higher concentration of F4TCNQ in the films. An electrical conductivity of 0.16 S cm^{-1} , a Seebeck coefficient of $208 \mu\text{V K}^{-1}$, and power factor of $0.86 \mu\text{W m}^{-1} \text{ K}^{-2}$ were observed for the optimized 17% F4TCNQ-P3HT- Sb_2Te_3 film.

5. Conclusion

In this review, we summarized printed thermoelectric materials into three groups: chalcogenides, other inorganic, and organic. The most advanced of these is the printing of chalcogenides, which within, the most advanced group of materials are the tellurides. Screen printing, dispenser printing, and inkjet printing were all used to make tellurides, however, only one literature example is shown to exhibit a ZT of ≥ 1 and this is for PbTe which has a much higher ZT than Bi_2Te_3 when manufactured by traditional methods such as spark plasma sintering. Of the three aforementioned printing techniques, screen printing does on an average yield the highest ZT values. For printing films of tellurides for thermoelectric applications, therefore, screen printing is most likely to yield the best performing material. Since 2018, however, examples of 3D printing tellurides have been reported in the literature. Using 3D printing techniques for tellurides is seen to yield ZT s of ≥ 1 , and almost all the other ZT values reported are still of a significant value ($ZT \geq 0.5$). Comparing PbTe, for example, 3D printing is seen to yield a ZT of 1.4 for 3D printing, compared to 1 for screen printing. The development of 3D printing of tellurides, therefore, in addition, to be being able to manufacture elements of dimensions required for efficient thermoelectric generators and being able to form bespoke shaped generators, also provides improved thermoelectric material properties compared to printed films. Indeed, the ZT values for 3D printed tellurides are in the order of 70% of those manufactured by the more costly, time-consuming and shape restrictive current commercial manufacturing techniques such as spark plasma sintering. 3D printing has shown to be able to produce modules that can match the curvature of pipes (a common place where waste heat is found) or produce micro devices that could be used on microchips.

Comparably to general thermoelectric materials research, in the area of printed thermoelectrics, selenides have not been studied in as much detail as tellurides. Cu_2Se has been spin coated, Ag_2Se printed and SnSe 3D printed, however, with Ag_2Se yielding a ZT of ≈ 1 and SnSe exhibiting the highest ZT of any printed material of 1.7. While the 3D printed SnSe value is the largest seen to date, due to single-crystal SnSe having the largest reported ZT (2.6) the 3D printed ZT value is again in the order of 70% of the value seen compared to the material manufactured by spark plasma sintering. While possibly coincidental due to the low sample size, there are early indications that 3D printed samples should aim for 70% of the ZT seen for the same material manufactured via more traditional techniques. To date, the only other 3D printed thermoelectric material is Cu_2S , which is shown to achieve a ZT of 0.63 (37% of that seen in SPS Cu_2S).

Besides chalcogenides, many other printed inorganic materials have been investigated for their thermoelectric performance. Metals such as Fe, Ni, and Ag have been studied, however, these are largely with the aim for making thermocouples. This has led to many Seebeck coefficient measurements for these materials, but not many of electrical conductivity and none for thermal conductivity. The high conductivity of these materials would most likely result in them having low ZT values, but without thermal conductivity measurements, this is not known. In contrast, Si has a conductivity value typically considered too low for thermoelectric applications. Nevertheless, thermoelectric generators have been printed using Si nanowires and manganese-silicon. The doctor blade printed $\text{MnSi}_{1.74}/\text{Mn}_{0.7}\text{Fe}_{0.3}\text{Si}_{1.6}$ module was mounted onto an engine exhaust and produced 5.5 mW cm^{-2} . A screen-printed ZnSb/CoSb₃ module was able to produce 0.1 mW cm^{-2} . Several oxides have been printed, however no ZT values have been reported. The most promising of these groups seems to be the cobaltates where power factors of up to $300 \mu\text{W m}^{-1} \text{ K}^{-2}$ have been seen.

Printed organic materials have also been investigated for their thermoelectric properties. These can be split into the groups of carbon nanotubes, conductive polymers, and composites. The main limitation with this group of materials is forming a stable n-type material. To circumvent this issue many groups have made p-type only devices or relied on an inorganic material to form the n-type material. Very limited thermoelectric properties have been reported for printed CNTs, however, a module that was stable with flexing was shown to produce 55 mW m^{-2} . This highlights printed CNTs as a potential route to wearable thermoelectric generators. Conductive polymers are a more established area for thermoelectrics, with PEDOT:PSS being the go to material. The thermoelectric properties of PEDOT:PSS have been investigated after many printing techniques: inkjet printing, soaking, stencil, screen printing, roll to roll, casting, and spraying. Screen printing was the technique that allowed for the device with the highest power output to be achieved $240 \mu\text{W}$, while stencil printing allowed for the device with the most polymer legs to be formed (1072). Again many of the PEDOT:PSS thermoelectric generators created were flexible, indeed the stencil printed device was printed into fabric. This highlights that much of the aim of printed organic thermoelectrics is to make wearable thermoelectric generators. Many organic composites have been printed utilizing

PEDOT:PSS including Bi₂Te₃, Sb₂Te₃, and V₂O₃. While one of the aims of these composites was to gain improved thermoelectric performance in organic thermoelectrics, the results were mixed with most performing worse than pure polymer examples presented in this review. V₂O₃ with PEDOT:PSS did make an n-type sample, albeit the sample was 97 molar% V₂O₃.

In summary, many printing techniques have been applied to thermoelectrics over the last few decades. These have historically often led to the formation of flexible devices as their unique selling point, due to their comparatively low *ZT* values compared to typical thermoelectric materials (e.g., Bi₂Te₃, PbTe) manufactured via traditional high energy and temperature techniques (e.g., SPS). The advent of 3D printing of thermoelectrics, however, within the last five years has led to printing being a viable alternative to conventional thermoelectric manufacturing techniques, achieving *ZT*s of around 70% of SPS alternatives. With the advantages of making custom shapes to match waste heat surfaces (e.g., pipes) and potentially lower cost of manufacturing (due to low temperature and pressure manufacturing), printing of thermoelectrics holds great promise to become the dominant future manufacturing technique for thermoelectrics.

In order to become the dominant future manufacturing technique for thermoelectrics, there are a few challenges that printing must overcome. Printed materials result in lower electrical conductivities than standard manufacturing techniques (e.g., SPS), in order to overcome this suitable dopants or conductive binders will need to be found to increase the electrical conductivities of typical thermoelectric materials. An alternative approach would be to utilize materials that are typically deemed too conductive for thermoelectrics. This review has shown that printed metals can act as thermoelectric materials with higher Seebeck coefficients than typical production routes for metals, but they are still too conductive for optimal thermoelectric performance. Intermediate bulk material with higher carrier concentrations than typical thermoelectric materials (10¹⁹–10²¹ cm⁻³),^[4] could potentially yield the optimal *ZT*s for printed thermoelectrics. As is the issue with recently discovered thermoelectric materials,^[43] finding suitable electrical contacts that minimize contact resistance between legs in thermoelectric generators yet do not chemically react with the thermoelectric materials will be key to allowing commercial success of printed thermoelectrics. Due to the often-rough nature of printed materials solid contacts cannot easily be added, therefore, printed contacts may hold the key as they can mold to the texture of the printed thermoelectric materials. Much of the cost of thermoelectric generator production can go on heat exchangers.^[209,210] In order to utilize the advantage of bespoke shaped thermoelectric generators that printing offers, low cost heat exchangers will need to be produced that match the printed geometric shapes. One way to potentially circumvent this is to use a series of small heat exchanges instead of a single large heat exchanger that are used with commercial devices today.

Supporting Information

Supporting Information is available from the Wiley Online Library or from the author.

Acknowledgements

M.R.B and M.J.C would like to thank EPSRC (EP/N020863/1) and the European Regional development Fund [c80892] through the Welsh Government for funding. G.H. and J.A. would like to acknowledge the M2A funding from the European Social Fund via the Welsh Government (c80816), EPSRC (EP/L015099/1) and Tata steel that has made this research possible.

Note: Figures were amended on May 3, 2022, after initial publication online to correct a mistake in the unit W m⁻¹ K⁻¹ (previously written as W⁻¹ m⁻¹ K⁻¹).

Conflict of Interest

The authors declare no conflict of interest.

Keywords

printed thermoelectrics, TEG, thermoelectric generators

Received: October 12, 2021

Revised: January 7, 2022

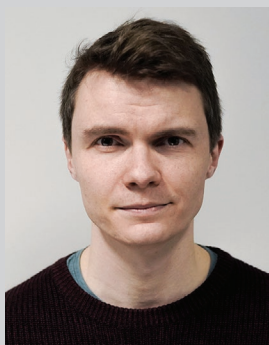
Published online: March 23, 2022

- [1] D. MacKay, *Sustainable Energy-without the Hot Air*, UIT, Cambridge **2008**.
- [2] J. Besseling, H. Pershad, *The Potential for Recovering and Using Surplus Heat from Industry Final Report*, London **2014**, <https://www.gov.uk/government/publications/the-potential-for-recovering-and-using-surplus-heat-from-industry>, (accessed: February 2021).
- [3] DEFRA, *Act on CO₂ Calculator: Public Trial Version Data, Methodology and Assumptions Paper*, **2007**, <http://www.stuffit.org/carbon/pdf-research/statistics/actonco2-calc-methodology.pdf>, (accessed: July 2021).
- [4] G. J. Snyder, E. S. Toberer, *Nat. Mater.* **2008**, *7*, 105.
- [5] D. A. Wright, *Nature* **1958**, *181*, 834.
- [6] A. F. Joffe, L. Stil'bans, *Rep. Prog. Phys.* **1959**, *22*, 306.
- [7] Y. He, P. Lu, X. Shi, F. Xu, T. Zhang, G. J. Snyder, C. Uher, L. Chen, *Adv. Mater.* **2015**, *27*, 3639.
- [8] G. Tan, F. Shi, S. Hao, L.-D. Zhao, H. Chi, X. Zhang, C. Uher, C. Wolverton, V. P. Dravid, M. G. Kanatzidis, *Nat. Commun.* **2016**, *7*, 12167.
- [9] L.-D. Zhao, S.-H. Lo, Y. Zhang, H. Sun, G. Tan, C. Uher, C. Wolverton, V. P. Dravid, M. G. Kanatzidis, *Nature* **2014**, *508*, 373.
- [10] A. F. Ioffe, *Physics of Semiconductors*, Academic, New York **1960**.
- [11] H. J. Goldsmid, *Introduction to Thermoelectricity*, Springer, Berlin **2016**.
- [12] M. Zebarjadi, K. Esfarjani, M. S. Dresselhaus, Z. F. Ren, G. Chen, *Energy Environ. Sci.* **2012**, *5*, 5147.
- [13] J. Yang, T. Caillat, *MRS Bull.* **2006**, *31*, 224.
- [14] M. Kishi, H. Nemoto, T. Hamao, M. Yamamoto, S. Sudou, M. Mandai, S. Yamamoto, *Eighteenth International Conference on Thermoelectrics. Proceedings* **1999**, 301.
- [15] D. M. Rowe, *CRC Handbook of Thermoelectrics*, CRC Press, Boca Raton, FL **1995**.
- [16] K. Yazawa, A. Shakouri, *J. Electron. Mater.* **2013**, *42*, 1946.
- [17] Department for Business Energy & Industrial Strategy, *Electricity Generation Costs*, **2016**, <https://www.gov.uk/government/publications/beis-electricity-generation-costs-november-2016>, (accessed: September 2021).
- [18] J. Weber, K. Potje-Kamloth, F. Haase, P. Detemple, F. Völklein, T. Doll, *Sens. Actuators, A* **2006**, *132*, 325.
- [19] A. E. Ostfeld, I. Deckman, A. M. Gaikwad, C. M. Lochner, A. C. Arias, *Sci. Rep.* **2015**, *5*, 15959.

- [20] P. Mariani, L. Vesce, A. Di Carlo, *Semicond. Sci. Technol.* **2015**, *30*, 104003.
- [21] F. De Rossi, J. A. Baker, D. Beynon, K. E. A. Hooper, S. M. P. Meroni, D. Williams, Z. Wei, A. Yasin, C. Charbonneau, E. H. Jewell, T. M. Watson, *Adv. Mater. Technol.* **2018**, *3*, 1800156.
- [22] D. Raptis, V. Stoichkov, S. M. P. Meroni, A. Pockett, C. A. Worsley, M. Carnie, D. A. Worsley, T. Watson, *Curr. Appl. Phys.* **2020**, *20*, 619.
- [23] J. Baker, K. Hooper, S. Meroni, A. Pockett, J. McGettrick, Z. Wei, R. Escalante, G. Oskam, M. Carnie, T. Watson, *J. Mater. Chem. A* **2017**, *5*, 18643.
- [24] T. Öhlund, *PhD Thesis*, Mid Sweden University **2014**.
- [25] H. Kipphan, *Handbook of Print Media: Technologies and Production Methods*, Springer Science and Business Media, Berlin **2001**.
- [26] Z. Cao, E. Koukharenko, M. J. Tudor, R. N. Torah, S. P. Beeby, *J. Phys.: Conf. Ser.* **2013**, *476*, 012031.
- [27] H. P. Le, *J. Imaging Sci. Technol.* **1998**, *42*, 49.
- [28] M. S. Hossain, T. Li, Y. Yu, J. Yong, J.-H. Bahk, E. Skafidas, *RSC Adv.* **2020**, *10*, 8421.
- [29] B. Chen, S. R. Das, W. Zheng, B. Zhu, B. Xu, S. Hong, C. Sun, X. Wang, Y. Wu, J. C. Claussen, *Adv. Electron. Mater.* **2017**, *3*, 1600524.
- [30] A. M. Gaikwad, A. C. Arias, D. A. Steingart, *Energy Technol.* **2015**, *3*, 305.
- [31] P. K. Wright, D. Dornfeld, A. Chen, C. C. Ho, J. W. Evans, *Trans. NAMRI/SME* **2010**, *38*, 555.
- [32] E. Desimone, K. Schacht, T. Jungst, J. Groll, T. Scheibel, *Pure Appl. Chem.* **2015**, *87*, 737.
- [33] Z. Cao, J. J. Shi, R. N. Torah, M. J. Tudor, S. P. Beeby, *J. Phys.: Conf. Ser.* **2015**, *660*, 012096.
- [34] F. Kim, B. Kwon, Y. Eom, J. E. Lee, S. Park, S. Jo, S. H. Park, B.-S. Kim, H. J. Im, M. H. Lee, T. S. Min, K. T. Kim, H. G. Chae, W. P. King, J. S. Son, *Nat. Energy* **2018**, *3*, 301.
- [35] M. M. Kruse, *Dissertation or Thesis*, Iowa State University, **2018**.
- [36] M. R. Burton, S. Mehraban, D. Beynon, J. McGettrick, T. Watson, N. P. Lavery, M. J. Carnie, *Adv. Energy Mater.* **2019**, *9*, 1900201.
- [37] M. R. Burton, S. Mehraban, J. McGettrick, T. Watson, N. P. Lavery, M. J. Carnie, *J. Mater. Chem. A* **2019**, *7*, 25586.
- [38] I. Petsagkourakis, K. Tybrandt, X. Crispin, I. Ohkubo, N. Satoh, T. Mori, *Sci. Technol. Adv. Mater.* **2018**, *19*, 836.
- [39] D. Beretta, N. Neophytou, J. M. Hodges, M. G. Kanatzidis, D. Narducci, M. Martin-Gonzalez, M. Beekman, B. Balke, G. Cerretti, W. Tremel, A. Zevalkink, A. I. Hofmann, C. Müller, B. Dörfling, M. Campoy-Quiles, M. Caironi, *Mater. Sci. Eng., R* **2019**, *138*, 100501.
- [40] X. Shi, J. Zou, Z. Chen, *Chem. Rev.* **2020**, *120*, 7399.
- [41] M. Massetti, F. Jiao, A. J. Ferguson, D. Zhao, K. Wijeratne, A. Würger, J. L. Blackburn, X. Crispin, S. Fabiano, *Chem. Rev.* **2021**, *121*, 12465.
- [42] Y. Jia, Q. Jiang, H. Sun, P. Liu, D. Hu, Y. Pei, W. Liu, X. Crispin, S. Fabiano, Y. Ma, Y. Cao, *Adv. Mater.* **2021**, *33*, 2102990.
- [43] Q. Yan, M. G. Kanatzidis, *Nat. Mater.* **2021**, <http://doi.org/10.1038/s41563-021-01109-w>.
- [44] Y. Shi, C. Sturm, H. Kleinke, *J. Solid State Chem.* **2019**, *270*, 273.
- [45] O. Yamashita, S. Tomiyoshi, K. Makita, *J. Appl. Phys.* **2003**, *93*, 368.
- [46] T. Fu, X. Yue, H. Wu, C. Fu, T. Zhu, X. Liu, L. Hu, P. Ying, J. He, X. Zhao, *J. Mater.* **2016**, *2*, 141.
- [47] C. Navone, M. Soulier, M. Plissonnier, A. L. Seiler, *J. Electron. Mater.* **2010**, *39*, 1755.
- [48] S. J. Kim, J. H. We, B. J. Cho, *Energy Environ. Sci.* **2014**, *7*, 1959.
- [49] Z. Cao, E. Koukharenko, M. J. Tudor, R. N. Torah, S. P. Beeby, *Sens. Actuators, A* **2016**, *238*, 196.
- [50] T. Varghese, C. Hollar, J. Richardson, N. Kempf, C. Han, P. Gamarachchi, D. Estrada, R. J. Mehta, Y. Zhang, *Sci. Rep.* **2016**, *6*, 33135.
- [51] S. J. Kim, H. E. Lee, H. Choi, Y. Kim, J. H. We, J. S. Shin, K. J. Lee, B. J. Cho, *ACS Nano* **2016**, *10*, 10851.
- [52] J. H. We, S. J. Kim, G. S. Kim, B. J. Cho, *J. Alloys Compd.* **2013**, *552*, 107.
- [53] S. Shin, R. Kumar, J. W. Roh, D.-S. Ko, H.-S. Kim, S. Il Kim, L. Yin, S. M. Schlossberg, S. Cui, J.-M. You, S. Kwon, J. Zheng, J. Wang, R. Chen, *Sci. Rep.* **2017**, *7*, 7317.
- [54] C. Han, G. Tan, T. Varghese, M. G. Kanatzidis, Y. Zhang, *ACS Energy Lett.* **2018**, *3*, 818.
- [55] A. L. Pires, I. F. Cruz, J. Silva, G. N. P. Oliveira, S. Ferreira-Teixeira, A. M. L. Lopes, J. P. Araújo, J. Fonseca, C. Pereira, A. M. Pereira, *ACS Appl. Mater. Interfaces* **2019**, *11*, 8969.
- [56] A. Chen, D. Madan, M. Koplou, P. K. Wright, J. W. Evans, *Technical Digest Power-MEMS* **2009**, pp. 277–280.
- [57] A. Chen, D. Madan, B. T. Mahlstedt, P. K. Wright, J. W. Evans, *Proceedings of the PowerMEMS*, Leuven, Belgium **2010**, 223.
- [58] A. Chen, D. Madan, P. K. Wright, J. W. Evans, *J. Micromech. Microeng.* **2011**, *21*, 104006.
- [59] D. Madan, A. Chen, P. K. Wright, J. W. Evans, *J. Appl. Phys.* **2011**, *109*, 034904.
- [60] D. Madan, A. Chen, P. K. Wright, J. W. Evans, *J. Electron. Mater.* **2012**, *41*, 1481.
- [61] D. Madan, Z. Wang, A. Chen, R. C. Juang, J. Keist, P. K. Wright, J. W. Evans, *ACS Appl. Mater. Interfaces* **2012**, *4*, 6117.
- [62] D. Madan, Z. Wang, A. Chen, R. Winslow, P. K. Wright, J. W. Evans, *Appl. Phys. Lett.* **2014**, *104*, 013902.
- [63] Z. Lu, M. Layani, X. Zhao, L. P. Tan, T. Sun, S. Fan, Q. Yan, S. Magdassi, H. H. Hng, *Small* **2014**, *10*, 3551.
- [64] B. Chen, M. Kruse, B. Xu, R. Tutika, W. Zheng, M. D. Bartlett, Y. Wu, J. C. Claussen, *Nanoscale* **2019**, *11*, 5222.
- [65] S. H. Park, S. Jo, B. Kwon, F. Kim, H. W. Ban, J. E. Lee, D. H. Gu, S. H. Lee, Y. Hwang, J.-S. Kim, D.-B. Hyun, S. Lee, K. J. Choi, W. Jo, J. S. Son, *Nat. Commun.* **2016**, *7*, 13403.
- [66] F. Kim, S. E. Yang, H. Ju, S. Choo, J. Lee, G. Kim, S. Jung, S. Kim, C. Cha, K. T. Kim, S. Ahn, H. G. Chae, J. S. Son, *Nat. Electron.* **2021**, *4*, 579.
- [67] J. Lee, S. Choo, H. Ju, J. Hong, S. E. Yang, F. Kim, D. H. Gu, J. Jang, G. Kim, S. Ahn, J. E. Lee, S. Y. Kim, H. G. Chae, J. S. Son, *Adv. Energy Mater.* **2021**, *11*, 2100190.
- [68] J. Wang, S. Liu, L. Li, *Energy Procedia* **2019**, *158*, 1052.
- [69] M. Feinaeugle, C. L. Sones, E. Koukharenko, R. W. Eason, *Smart Mater. Struct.* **2013**, *22*, 115023.
- [70] J. Shi, H. Chen, S. Jia, W. Wang, *J. Manuf. Process.* **2019**, *37*, 370.
- [71] J. Qiu, Y. Yan, T. Luo, K. Tang, L. Yao, J. Zhang, M. Zhang, X. Su, G. Tan, H. Xie, M. G. Kanatzidis, C. Uher, X. Tang, *Energy Environ. Sci.* **2019**, *12*, 3106.
- [72] R. Welch, D. Hobbs, A. J. Birnbaum, G. Nolas, S. LeBlanc, *Adv. Mater. Interfaces* **2021**, *8*, 2100185.
- [73] W. M. Haynes, *CRC Handbook of Chemistry and Physics*, 95th ed, CRC Press, Boca Raton, FL **2014**.
- [74] Trading Economics Tellurium, <https://tradingeconomics.com/commodity/tellurium>, (accessed: October 2021).
- [75] Trading Economics Aluminium, <https://tradingeconomics.com/commodity/aluminum>, (accessed: October 2021).
- [76] T.-R. Wei, C.-F. Wu, F. Li, J.-F. Li, *J. Mater.* **2018**, *4*, 304.
- [77] L.-D. Zhao, S. Hao, S.-H. Lo, C.-I. Wu, X. Zhou, Y. Lee, H. Li, K. Biswas, T. P. Hogan, C. Uher, C. Wolverton, V. P. Dravid, M. G. Kanatzidis, *J. Am. Chem. Soc.* **2013**, *135*, 7364.
- [78] H. Liu, X. Shi, F. Xu, L. Zhang, W. Zhang, L. Chen, Q. Li, C. Uher, T. Day, G. J. Snyder, *Nat. Mater.* **2012**, *11*, 422.
- [79] L.-D. Zhao, C. Chang, G. Tan, M. G. Kanatzidis, *Energy Environ. Sci.* **2016**, *9*, 3044.
- [80] S. Sassi, C. Candolfi, J.-B. Vaney, V. Ohorodniichuk, P. Masschelein, A. Dauscher, B. Lenoir, *Appl. Phys. Lett.* **2014**, *104*, 212105.
- [81] X. Shi, K. Zheng, M. Hong, W. Liu, R. Moshwan, Y. Wang, X. Qu, Z.-G. Chen, J. Zou, *Chem. Sci.* **2018**, *9*, 7376.
- [82] M. R. Burton, T. Liu, J. McGettrick, S. Mehraban, J. Baker, A. Pockett, T. Watson, O. Fenwick, M. J. Carnie, *Adv. Mater.* **2018**, *30*, 1801357.

- [83] Z. Lin, C. Hollar, J. S. Kang, A. Yin, Y. Wang, H.-Y. Shiu, Y. Huang, Y. Hu, Y. Zhang, X. Duan, *Adv. Mater.* **2017**, *29*, 1606662.
- [84] M. M. Mallick, A. G. Rösch, L. Franke, S. Ahmed, A. Gall, H. Geßwein, J. Aghassi, U. Lemmer, *ACS Appl. Mater. Interfaces* **2020**, *12*, 19655.
- [85] M. M. Mallick, A. G. Rösch, L. Franke, A. Gall, S. Ahmad, H. Geßwein, A. Mazilkin, C. Kübel, U. Lemmer, *J. Mater. Chem. A* **2020**, *8*, 16366.
- [86] M. M. Mallick, L. Franke, A. G. Rösch, U. Lemmer, *ACS Energy Lett.* **2021**, *6*, 85.
- [87] A. V. Powell, *J. Appl. Phys.* **2019**, *126*, 100901.
- [88] B. Chen, C. Uher, L. Iordanidis, M. G. Kanatzidis, *Chem. Mater.* **1997**, *9*, 1655.
- [89] Y. He, T. Day, T. Zhang, H. Liu, X. Shi, L. Chen, G. J. Snyder, *Adv. Mater.* **2014**, *26*, 3974.
- [90] C. Goupil, *Continuum Theory and Modeling of Thermoelectric Elements*, Wiley-VCH, New York **2015**.
- [91] P. M. Markowski, A. Dziedzic, *Microelectron. Reliab.* **2008**, *48*, 890.
- [92] K. Ankireddy, A. K. Menon, B. Iezzi, S. K. Yee, M. D. Losego, J. S. Jur, *J. Electron. Mater.* **2016**, *45*, 5561.
- [93] S. Duby, B. Ramsey, D. Harrison, G. Hay, *Sensors IEEE* **2004**, *3*, 1098.
- [94] S. Duby, B. J. Ramsey, D. J. Harrison, *Electron. Lett.* **2005**, *41*, 312.
- [95] P. M. Markowski, A. Dziedzic, *J. Microelectron. Electron. Packag.* **2006**, *3*, 95.
- [96] P. M. Markowski, W. Pinczakowski, L. Straszewski, A. Dziedzic *30th International Spring Seminar on Electronics Technology (ISSE)*, **2007**, pp. 223–228.
- [97] P. M. Markowski, A. Dziedzic, *33rd International Spring Seminar on Electronics Technology*, ISSE 2010, **2010**, pp. 77–81.
- [98] P. Markowski, A. Dziedzic, E. Prociow, *2008 2nd Electronics System-Integration Technology Conference*, **2008**, pp. 601–606.
- [99] P. Markowski, E. Prociów, A. D.-O. Applicata, *Opt. Appl.* **2009**, *39*, 681.
- [100] R. Lechner, H. Wiggers, A. Ebberts, J. Steiger, M. S. Brandt, M. Stutzmann, *Phys. Status Solidi RRL* **2007**, *1*, 262.
- [101] S. M. Sze, K. K. Ng, *Physics of Semiconductor Devices*, Wiley-VCH, New York **1981**.
- [102] T. H. Geballe, G. W. Hull, *Phys. Rev.* **1955**, *98*, 940.
- [103] E. Drahi, A. Gupta, S. Blayac, L. Lombez, M. Jubault, P. Benaben in *Technical Proceedings of the 2013 NSTI Nanotechnology Conference and Expo, NSTI-Nanotech 2013*, **2013**, p. 247.
- [104] E. Drahi, A. Gupta, S. Blayac, S. Saunier, L. Lombez, M. Jubault, G. Renou, P. Benaben, *MRS Online Proc. Libr.* **2013**, *1536*, 201.
- [105] E. Drahi, A. Gupta, S. Blayac, S. Saunier, P. Benaben, *Phys. Status Solidi* **2014**, *211*, 1301.
- [106] S. Khan, R. S. Dahiya, L. Lorenzelli, *2014 44th European Solid State Device Research Conference (ESSDERC)*, **2014**, p. 86.
- [107] S. Khan, L. Lorenzelli, R. Dahiya, *IEEE J. Electron Devices Soc.* **2016**, *4*, 189.
- [108] T. Kajitani, T. Ueno, Y. Miyazaki, K. Hayashi, T. Fujiwara, R. Ihara, T. Nakamura, M. Takakura, *J. Electron. Mater.* **2014**, *43*, 1993.
- [109] H. B. Lee, J. H. We, H. J. Yang, K. Kim, K. C. Choi, B. J. Cho, *Thin Solid Films* **2011**, *519*, 5441.
- [110] H. B. Lee, H. J. Yang, J. H. We, K. Kim, K. C. Choi, B. J. Cho, *J. Electron. Mater.* **2011**, *40*, 615.
- [111] L. J. Hoong, Y. C. Keat, A. Chik, T. P. Leng, *Ceram. Int.* **2016**, *42*, 12064.
- [112] Y. H. Kang, K.-S. Jang, C. Lee, S. Y. Cho, *ACS Appl. Mater. Interfaces* **2016**, *8*, 5216.
- [113] R. Rudež, P. M. Markowski, M. Presečnik, M. Košir, A. Dziedzic, S. Bernik, *Ceram. Int.* **2015**, *41*, 13201.
- [114] N. Van Nong, A. J. Samson, N. Pryds, S. Linderoth, *J. Electron. Mater.* **2012**, *41*, 1280.
- [115] D. Liu, P. Shi, W. Ren, Y. Liu, M. Liu, Y. Zhang, Q. Lin, B. Tian, Z. Jiang, Z.-G. Ye, *J. Eur. Ceram. Soc.* **2018**, *38*, 5030.
- [116] K.-W. Lee, W. E. Pickett, *Phys. Rev. B* **2009**, *80*, 125133.
- [117] T. Hashimoto, K. Shibata, K. Tsuchida, A. Kato, *J. Mater. Sci. Lett.* **1992**, *11*, 745.
- [118] T. T. Huang, W. Wu, *Adv. Mater. Interfaces* **2020**, *7*, 2000015.
- [119] H. Andersson, P. Šuly, G. Thungström, M. Engholm, R. Zhang, J. Mašlík, H. Olin, *J. Low Power Electron. Appl.* **2019**, *9*, 14.
- [120] A. R. M. Siddique, S. Mahmud, B. Van Heyst, *Renewable Sustainable Energy Rev.* **2017**, *73*, 730.
- [121] F. Jiao, in *Flexible and Wearable Electronics for Smart Clothing*, (Eds: G. Wang, C. Hou, H. Wang), Wiley, New York **2020**, pp. 49–66.
- [122] Q. Wu, J. Hu, *Composites, Part B* **2016**, *107*, 59.
- [123] H. M. Elmoughni, A. K. Menon, R. M. W. Wolfe, S. K. Yee, *Adv. Mater. Technol.* **2019**, *4*, 1800708.
- [124] A. Nozariasbmarz, H. Collins, K. Dsouza, M. H. Polash, M. Hosseini, M. Hyland, J. Liu, A. Malhotra, F. M. Ortiz, F. Mohaddes, V. P. Ramesh, Y. Sargolzaeiaval, N. Snouwaert, M. C. Öztürk, D. Vashae, *Appl. Energy* **2020**, *258*, 114069.
- [125] J. He, T. M. Tritt, *Science* **2017**, *357*, 1369.
- [126] L. M. Cowen, J. Atoyo, M. J. Carnie, D. Baran, B. C. Schroeder, *ECS J. Solid State Sci. Technol.* **2017**, *6*, N3080.
- [127] Z. Zhang, J. Qiu, S. Wang, *Manuf. Lett.* **2016**, *8*, 6.
- [128] M. Mukaida, K. Kirihara, S. Horike, Q. Wei, *J. Mater. Chem. A* **2020**, *8*, 22544.
- [129] N. Nandihalli, C. J. Liu, T. Mori, *Nano Energy* **2020**, *78*, 105186.
- [130] W. Zeng, X. M. Tao, S. Lin, C. Lee, D. Shi, K. ho Lam, B. Huang, Q. Wang, Y. Zhao, *Nano Energy* **2018**, *54*, 163.
- [131] K. Kordás, T. Mustonen, G. Tóth, H. Jantunen, M. Lajunen, C. Soldano, S. Talapatra, S. Kar, R. Vajtai, P. M. Ajayan, *Small* **2006**, *2*, 1021.
- [132] J. Kim, R. Kumar, A. J. Bandodkar, J. Wang, *Adv. Electron. Mater.* **2017**, *3*, 1600260.
- [133] Q. Jiang, J. Yang, P. Hing, H. Ye, *Mater. Adv.* **2020**, *1*, 1038.
- [134] W. A. D. M. Jayathilaka, K. Qi, Y. Qin, A. Chinnappan, W. Serrano-García, C. Baskar, H. Wang, J. He, S. Cui, S. W. Thomas, S. Ramakrishna, *Adv. Mater.* **2019**, *31*, 1805921.
- [135] M. Dargusch, W. Di Liu, Z. G. Chen, *Adv. Sci.* **2020**, *7*, 2001362.
- [136] Y. Wang, Y. Shi, D. Mei, Z. Chen, *Appl. Energy* **2017**, *205*, 710.
- [137] G. Lee, C. S. Kim, S. Kim, Y. J. Kim, H. Choi, B. J. Cho, *Energy* **2019**, *179*, 12.
- [138] S. Krainer, C. Smit, U. Hirn, *RSC Adv.* **2019**, *9*, 31708.
- [139] S. Jo, S. Choo, F. Kim, S. H. Heo, J. S. Son, *Adv. Mater.* **2019**, *31*, 1.
- [140] S. J. Potts, C. Phillips, T. Claypole, E. Jewell, *Coatings* **2020**, *10*, 1008.
- [141] H. Menon, R. Aiswarya, K. P. Surendran, *RSC Adv.* **2017**, *7*, 44076.
- [142] G. Huebner, in *Handbook of Industrial Inkjet Printing: A Full System Approach*, (Ed: W. Zapka), Wiley-VCH, Weinheim, Germany **2017**, pp. 7–22.
- [143] R. Kroon, D. A. Mengistie, D. Kiefer, J. Hynynen, J. D. Ryan, L. Yu, C. Müller, *Chem. Soc. Rev.* **2016**, *45*, 6147.
- [144] T. Juntunen, H. Jussila, M. Ruoho, S. Liu, G. Hu, T. Albrow-Owen, L. W. T. Ng, R. C. T. Howe, T. Hasan, Z. Sun, I. Tittonen, *Adv. Funct. Mater.* **2018**, *28*, 1800480.
- [145] T. Wei, J. Ruan, Z. Fan, G. Luo, F. Wei, *Carbon* **2007**, *45*, 2712.
- [146] R. Tortorich, J.-W. Choi, *Nanomaterials* **2013**, *3*, 453.
- [147] J. W. Song, J. Kim, Y. H. Yoon, B. S. Choi, J. H. Kim, C. S. Han, *Nanotechnology* **2008**, *19*, 095702.
- [148] C. K. Najeeb, J.-H. Lee, J. Chang, J.-H. Kim, *Nanotechnology* **2010**, *21*, 385302.
- [149] C. A. Hewitt, A. B. Kaiser, S. Roth, M. Craps, R. Czerw, D. L. Carroll, *Nano Lett.* **2012**, *12*, 1307.
- [150] K. Suemori, S. Hoshino, T. Kamata, *Appl. Phys. Lett.* **2013**, *103*, 153902.
- [151] R. Tortorich, H. Shamkhalichenar, J.-W. Choi, *Appl. Sci.* **2018**, *8*, 288.

- [152] H. Okimoto, T. Takenobu, K. Yanagi, Y. Miyata, H. Shimotani, H. Kataura, Y. Iwasa, *Adv. Mater.* **2010**, *22*, 3981.
- [153] T. Wang, M. A. Roberts, I. A. Kinloch, B. Derby, *J. Phys. D: Appl. Phys.* **2012**, *45*, 315304.
- [154] R. P. Tortorich, E. Song, J.-W. Choi, *J. Electrochem. Soc.* **2014**, *161*, B3044.
- [155] S. Azoubel, S. Shemesh, S. Magdassi, *Nanotechnology* **2012**, *23*, 344003.
- [156] S. Horike, T. Fukushima, T. Saito, T. Kuchimura, Y. Koshiba, M. Morimoto, K. Ishida, *Mol. Syst. Des. Eng.* **2017**, *2*, 616.
- [157] S. Horike, T. Fukushima, T. Saito, Y. Koshiba, K. Ishida, *Chem. Phys. Lett.* **2018**, *691*, 219.
- [158] H. Shirakawa, E. J. Louis, A. G. MacDiarmid, C. K. Chiang, A. J. Heeger, *J. Chem. Soc., Chem. Commun.* **1977**, <https://pubs.rsc.org/en/content/articlelanding/1977/c3/c39770000578>.
- [159] S. Lee, S. Kim, A. Pathak, A. Tripathi, T. Qiao, Y. Lee, H. Lee, H. Y. Woo, *Macromol. Res.* **2020**, *28*, 531.
- [160] C.-J. Yao, H.-L. Zhang, Q. Zhang, *Polymers* **2019**, *11*, 107.
- [161] N. Dubey, M. Leclerc, *J. Polym. Sci., Part B: Polym. Phys.* **2011**, *49*, 467.
- [162] M. N. Gueye, A. Carella, J. Faure-Vincent, R. Demadrille, J. P. Simonato, *Prog. Mater. Sci.* **2020**, *108*, 100616.
- [163] J. Atoyo, M. R. Burton, J. McGettrick, M. J. Carnie, *Polymers* **2020**, *12*, 559.
- [164] J. Kim, J. G. Jang, J.-I. Hong, S. H. Kim, J. Kwak, *J. Mater. Sci.: Mater. Electron.* **2016**, *27*, 6122.
- [165] X. Wang, F. Meng, H. Tang, Z. Gao, S. Li, F. Jiang, J. Xu, *J. Mater. Sci.* **2017**, *52*, 9806.
- [166] B. J. Worfolk, S. C. Andrews, S. Park, J. Reinspach, N. Liu, M. F. Toney, S. C. B. Mannsfeld, Z. Bao, *Proc. Natl. Acad. Sci. USA* **2015**, *112*, 14138.
- [167] T. A. Yemata, Y. Zheng, A. K. K. Kyaw, X. Wang, J. Song, W. S. Chin, J. Xu, *RSC Adv.* **2020**, *10*, 1786.
- [168] H. Li, Y. Liang, S. Liu, F. Qiao, P. Li, C. He, *Org. Electron.* **2019**, *69*, 62.
- [169] N.-G. Park, K. Zhu, *Nat. Rev. Mater.* **2020**, *5*, 333.
- [170] Z. Zhu, J. Lowes, J. Berron, B. Smith, D. Sullivan, *ECS Trans.* **2014**, *60*, 293.
- [171] B. W. Boudouris, S. Yee, *J. Appl. Polym. Sci.* **2017**, *134*, 44456.
- [172] H. Fang, B. C. Popere, E. M. Thomas, C.-K. Mai, W. B. Chang, G. C. Bazan, M. L. Chabiny, R. A. Segalman, *J. Appl. Polym. Sci.* **2017**, *134*, 44208.
- [173] J. F. Serrano-Claumarchirant, M. Culebras, R. Muñoz-Espí, A. Cantarero, C. M. Gómez, M. N. Collins, *ACS Appl. Energy Mater.* **2020**, *3*, 861.
- [174] Y. Sun, C. A. Di, W. Xu, D. Zhu, *Adv. Electron. Mater.* **2019**, *5*, 1800825.
- [175] B. Kim, J. U. Hwang, E. Kim, *Energy Environ. Sci.* **2020**, *13*, 859.
- [176] O. Bubnova, Z. U. Khan, A. Malti, S. Braun, M. Fahlman, M. Berggren, X. Crispin, *Nat. Mater.* **2011**, *10*, 429.
- [177] B. Winther-Jensen, K. West, *Macromolecules* **2004**, *37*, 4538.
- [178] Y. Li, Y. Du, Y. Dou, K. Cai, J. Xu, *Synth. Met.* **2017**, *226*, 119.
- [179] Q. Wei, M. Mukaida, K. Kiriwara, Y. Naitoh, T. Ishida, *Materials* **2015**, *8*, 732.
- [180] O. Bubnova, M. Berggren, X. Crispin, *J. Am. Chem. Soc.* **2012**, *134*, 16456.
- [181] J. Feng-Xing, X. Jing-Kun, L. Bao-Yang, X. Yu, H. Rong-Jin, L. Lai-Feng, *Chin. Phys. Lett.* **2008**, *25*, 2202.
- [182] Q. Jiang, C. Liu, J. Xu, B. Lu, H. Song, H. Shi, Y. Yao, L. Zhang, *J. Polym. Sci., Part B: Polym. Phys.* **2014**, *52*, 737.
- [183] Q. Wei, M. Mukaida, K. Kiriwara, Y. Naitoh, T. Ishida, *RSC Adv.* **2014**, *4*, 28802.
- [184] Q. Wei, M. Mukaida, K. Kiriwara, Y. Naitoh, T. Ishida, *Appl. Phys. Express* **2014**, *7*, 031601.
- [185] T. Park, H. Lim, J. U. Hwang, J. Na, H. Lee, E. Kim, *APL Mater.* **2017**, *5*, 074106.
- [186] C. Wang, K. Sun, J. Fu, R. Chen, M. Li, Z. Zang, X. Liu, B. Li, H. Gong, J. Ouyang, *Adv. Sustainable Syst.* **2018**, *2*, 1800085.
- [187] Z. Li, H. Sun, C. L. Hsiao, Y. Yao, Y. Xiao, M. Shahi, Y. Jin, A. Cruce, X. Liu, Y. Jiang, W. Meng, F. Qin, T. Ederth, S. Fabiano, W. M. Chen, X. Lu, J. Birch, J. W. Brill, Y. Zhou, X. Crispin, F. Zhang, *Adv. Electron. Mater.* **2018**, *4*, 1700496.
- [188] Z. Li, G. Ma, R. Ge, F. Qin, X. Dong, W. Meng, T. Liu, J. Tong, F. Jiang, Y. Zhou, K. Li, X. Min, K. Huo, Y. Zhou, *Angew. Chem., Int. Ed.* **2016**, *55*, 979.
- [189] N. A. Khoso, A. Ahmed, H. Deb, S. Tian, X. Jiao, X. Y. Gong, J. Wang, *Org. Electron.* **2019**, *75*, 105368.
- [190] A. Mazaheripour, S. Majumdar, D. Hanemann-Rawlings, E. M. Thomas, C. McGuinness, L. D'Alencon, M. L. Chabiny, R. A. Segalman, *Chem. Mater.* **2018**, *30*, 4816.
- [191] S. Kee, N. Kim, B. S. Kim, S. Park, Y. H. Jang, S. H. Lee, J. Kim, J. Kim, S. Kwon, K. Lee, *Adv. Mater.* **2016**, *28*, 8625.
- [192] D. Ju, D. Kim, H. Yook, J. W. Han, K. Cho, *Adv. Funct. Mater.* **2019**, *29*, 1905590.
- [193] S. Kee, H. Kim, S. H. K. Paleti, A. El Labban, M. Neophytou, A.-H. Emwas, H. N. Alshareef, D. Baran, *Chem. Mater.* **2019**, *31*, 3519.
- [194] M. Y. Teo, N. Kim, S. Kee, B. S. Kim, G. Kim, S. Hong, S. Jung, K. Lee, *ACS Appl. Mater. Interfaces* **2017**, *9*, 819.
- [195] S. Xu, M. Hong, X.-L. Shi, Y. Wang, L. Ge, Y. Bai, L. Wang, M. Dargusch, J. Zou, Z. Chen, *Chem. Mater.* **2019**, *31*, 5238.
- [196] E. Yvenou, M. Sandroni, A. Carella, M. N. Gueye, J. Faure-Vincent, S. Pouget, R. Demadrille, J.-P. Simonato, *Mater. Chem. Front.* **2020**, *4*, 2054.
- [197] M. N. Gueye, A. Carella, N. Massonnet, E. Yvenou, S. Brenet, J. Faure-Vincent, S. Pouget, F. Rieutord, H. Okuno, A. Benayad, R. Demadrille, J.-P. Simonato, *Chem. Mater.* **2016**, *28*, 3462.
- [198] A. G. Rösch, A. Gall, S. Aslan, M. Hecht, L. Franke, M. M. Mallick, L. Penth, D. Bahro, D. Friderich, U. Lemmer, *npj Flexible Electron.* **2021**, *5*, 1.
- [199] M. Massetti, S. Bonfadini, D. Nava, M. Butti, L. Criante, G. Lanzani, L. Qiu, J. C. Hummelen, J. Liu, L. J. A. Kostler, M. Caironi, *Nano Energy* **2020**, *75*, 104983.
- [200] M. Shakeel, K. Rehman, S. Ahmad, M. Amin, N. Iqbal, A. Khan, *Renewable Energy* **2021**, *167*, 853.
- [201] F. Jiao, C. Di, Y. Sun, P. Sheng, W. Xu, D. Zhu, *Philos. Trans. R. Soc., A* **2014**, *372*, 20130008.
- [202] A. K. Menon, O. Meek, A. J. Eng, S. K. Yee, *J. Appl. Polym. Sci.* **2017**, *134*, 44060.
- [203] C. Y. Yang, M. A. Stoeckel, T. P. Ruoko, H. Y. Wu, X. Liu, N. B. Kolhe, Z. Wu, Y. Puttisong, C. Musumeci, M. Massetti, H. Sun, K. Xu, D. Tu, W. M. Chen, H. Y. Woo, M. Fahlman, S. A. Jenekhe, M. Berggren, S. Fabiano, *Nat. Commun.* **2021**, *12*, 2354.
- [204] E. J. Bae, Y. H. Kang, K.-S. Jang, C. Lee, S. Y. Cho, *Nanoscale* **2016**, *8*, 10885.
- [205] C. Ou, L. Zhang, Q. Jing, V. Narayan, S. Kar-Narayan, *Adv. Electron. Mater.* **2020**, *6*, 1900720.
- [206] S. Ferhat, C. Domain, J. Vidal, D. Noël, B. Ratier, B. Lucas, *Sustainable Energy Fuels* **2018**, *2*, 199.
- [207] C. J. An, Y. C. Lee, Y. H. Kang, S. Y. Cho, *Carbon* **2017**, *124*, 662.
- [208] E. Jang, A. Poosapati, D. Madan, *ACS Appl. Energy Mater.* **2018**, *1*, 1455.
- [209] S. K. Yee, S. LeBlanc, K. E. Goodson, C. Dames, *Energy Environ. Sci.* **2013**, *6*, 2561.
- [210] S. LeBlanc, S. K. Yee, M. L. Scullin, C. Dames, K. E. Goodson, *Renewable Sustainable Energy Rev.* **2014**, *32*, 313.



Matthew Burton is a postdoctoral researcher for SPECIFIC-IKC at the Faculty of Science and Engineering at Swansea University. He obtained his Masters of Chemistry (MChem) from the University of Southampton (2013). He subsequently obtained his Ph.D. on thermoelectrics at the University of Southampton in 2017. He has been a postdoctoral researcher at Swansea University since 2017 focusing on printed thermoelectric materials. His research interests are focused on printed thermoelectric materials for use in generators to harness waste heat from buildings.



Geraint Howells received his B.Eng. in Materials Engineering and Science from Swansea University in 2019. Currently, he is doing an Engineering doctorate (EngD) at Swansea University in conjunction with Tata steel studying thermoelectrics, and how they can be used to recover industrial waste heat.



Jonathan Atoyo is a materials scientist specializing in characterization techniques using scanning electron microscopy and energy dispersive spectroscopy to identify and quantify different elements in metals, polymers, and other materials. He obtained a B.Sc. in Chemistry from the University of Greenwich (2016) and his Ph.D. from Swansea University (2021). His Ph.D. looked at improving the thermoelectric properties of organic and hybrid thermoelectrics.



Matt Carnie is associate professor at Swansea University, where he also gained a B.Sc. in Chemistry (2003) and an MRes (2007) and EngD (2011) in Materials Science. His work encompasses both photovoltaic and thermoelectric materials and devices.